

THE EFFECT OF THE A-SITE CATION ON THE PHASE TRANSITION TEMPERATURE OF METAL HALIDE PEROVSKITES

PREPRINT, COMPILED FEBRUARY 24, 2026

Tom Braeckevelt^{1,2}, Sander Vandenhoute¹, Sven M. J. Rogge¹, Johan Hofkens², and Veronique Van Speybroeck^{†,1}

¹Center for Molecular Modeling, Ghent University, Technologiepark 46, Zwijnaarde 9052, Belgium

²Department of Chemistry, KU Leuven, Celestijnenlaan 200F, Leuven 3001, Belgium

† Email: Veronique.VanSpeybroeck@UGent.be

ABSTRACT

A key challenge for the practical application of metal halide perovskites (MHPs) is the instability of the desired perovskite phase relative to the optically non-active δ phase. To determine the phase stability, we previously developed a procedure to compute the harmonic free energy as a function of temperature, which was suited for CsPbI₃ but fails when Cs is replaced by organic cations due to their rotational freedom. Herein we propose a multistep thermodynamic integration (TI) approach that corrects the harmonic free energy to obtain the Gibbs free energy. Given the abundance of local minima in these materials, we employ replica exchange to prevent simulations from getting trapped, while introducing an intermediate potential energy surface to improve convergence and reduce computational cost. Benchmarking energy and forces from different exchange-correlation functionals and dispersion methods against high-level RPA+HF calculations identifies PBE+D3(BJ) as the best trade-off between accuracy, computational efficiency, and precision. To perform molecular dynamics simulations within the TI framework, it was necessary to train a machine learning potential using the MACE architecture on *ab initio* data calculated with density functional theory. Our results show that, for all three materials, the free energy difference between the γ and δ phases exhibits a very similar temperature dependence. This suggests that phase stability is primarily governed by differences in ground-state energy, rather than by material-specific thermal effects. Beyond these three materials, our methodology provides a robust framework for investigating the phase behavior of other MHPs, paving the way for the discovery of more stable perovskites.

Keywords metal halide perovskites, free energy, machine learning interatomic potentials, thermodynamic integration

1 INTRODUCTION

Over the past decade, metal halide perovskites (MHPs) with the general composition ABX₃ have garnered significant interest for a variety of optoelectronic applications.[1, 2, 3] However, many MHPs suffer from low stability and readily degrade under certain external conditions.[4] In particular, widely studied MHPs such as CsPbI₃ and FAPbI₃ (FA = formamidinium) exhibit a perovskite phase (also referred to as the black phase or, depending on its symmetry, as the α , β , or γ phase) that is metastable at room temperature. Over time, this perovskite phase transitions into a non-perovskite phase, often called the yellow phase or δ phase, which significantly deteriorates the optoelectronic properties. Interestingly, substituting the A-site cation from Cs⁺ to FA⁺ for APbI₃ MHPs leads to another δ phase that is stable at room temperature, while using methylammonium cations (MA⁺) leads to a stable perovskite phase at room temperature.[5] Fig. 1 illustrates the different PbI frameworks of the two δ phases and the γ phase, introducing a nomenclature to distinguish the two δ phases: δ_{Cs} and δ_{FA} .

In recent years, significant effort has been dedicated to stabilizing the perovskite phase across various MHPs. Experimental studies have shown that this can be achieved through compositional and strain engineering, surface functionalization, and crystal size control.[6, 7, 8, 9, 10, 11, 12, 13] However, the underlying driving forces behind these stabilizing effects remain poorly understood. To address this gap, we computationally predict the stability of the perovskite phase, allowing us to gain molecular-level insights and identify the key stabilizing factors.[14, 15] In previous work, we successfully predicted the

transition temperature of CsPbI₃. [16] To further elucidate the A-site cations influence on phase stability at room temperature, we extend our approach to FAPbI₃ and MAPbI₃. However, a key challenge arises: the organic cations possess rotational degrees of freedom, which significantly affect the free energy landscape. Our previous methodology relied on the harmonic approximation, which becomes inadequate when rotational motions are significant.[17]

To correct for the errors introduced by the harmonic approximation, we employ a combination of thermodynamic integration (TI) methods, following the approach outlined by Cheng and Ceriotti.[18] TI has been successfully applied to various systems, including the thermodynamics of water,[19] metal-organic frameworks,[20] nitrogen,[21] proton hopping and adsorption in zeolites,[22, 23] and multicomponent alloys.[24] TI states that the change in free energy along a given path is equal to the ensemble average of the derivative of the potential energy along that path. The primary challenge lies in achieving convergence of these ensemble averages, which typically demands significant computational resources. As a result, TI has traditionally been applied to relatively simple model systems[25, 26] or studies relying on classical force fields.[27, 20] Unfortunately, the accuracy of TI is highly dependent on the quality of the force field.[27]

Recently, machine learning potentials (MLPs) have been employed in TI calculations to achieve *ab initio* accuracy at a significantly lower computational cost.[19, 24, 28, 29] This is necessary because the computational cost of *ab initio* methods is

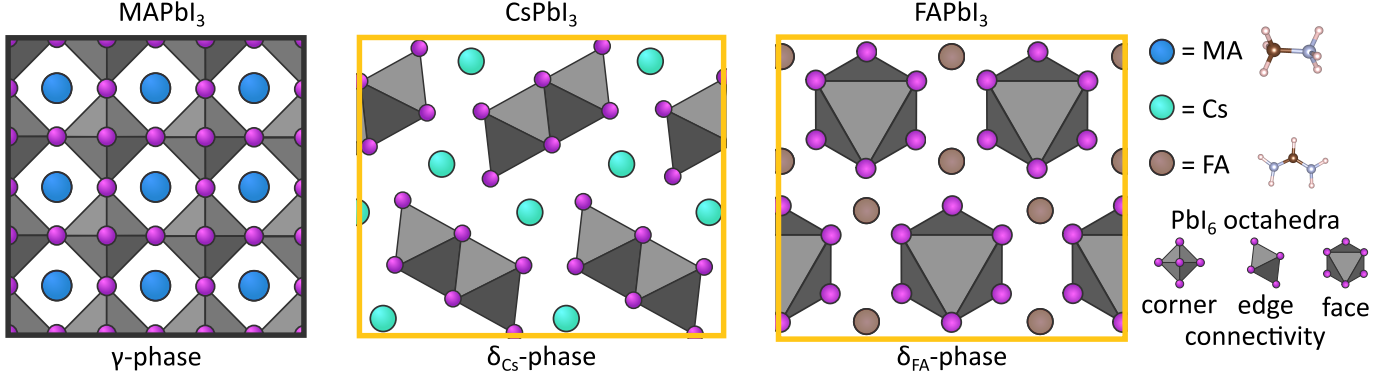


Figure 1: Schematic representation of the most stable phase for MAPbI₃, CsPbI₃, and FAPbI₃ at room temperature.

prohibitive for the extensive sampling required in TI. Message-passing equivariant MLPs such as NequIP[30] and MACE[31] combine high accuracy with a low data requirement. This enables training on more accurate *ab initio* data and broadens the range of materials and phases that can be studied. To this end, we will evaluate the accuracy of various *ab initio* methods, assessing both energy and force predictions by benchmarking them against RPA+HF.

An additional challenge arises when studying flexible materials such as MHPs.[32] The phase space associated with a stable phase may contain energy barriers that are unlikely to be overcome during molecular dynamics (MD) simulations at lower temperatures.[33, 34, 35, 36] To avoid the system getting trapped into a local minimum, we apply replica exchange (REX) [37] assuming that the MD at the highest temperature can frequently cross those barriers. REX facilitates Monte Carlo (MC) swaps between MD runs at different temperatures, pressures, or Hamiltonians,[38] allowing structural information sampled at high temperatures to be transferred to lower temperatures. REX has been shown to efficiently explore phase space at lower temperatures, where conventional MD simulations would otherwise remain stuck in local minima.[38] Due to its effectiveness, REX has been applied to various systems, including protein folding,[37] phase transitions in metal-organic frameworks,[39] and cation distributions in zeolites.[40]

This paper is structured as follows: First, we outline the theory and computational details of our revised methodology. Next, we evaluate the accuracy of different *ab initio* methods. Finally, we apply our revised approach to CsPbI₃, FAPbI₃, and MAPbI₃, obtaining free energy differences between phases as a function of temperature, from which we determine the transition temperatures.

2 METHODOLOGY

Thermodynamic integration (TI) is computationally expensive. To accelerate calculations, machine learning potentials (MLPs) are trained using MACE.[31] MACE is a message-passing neural network with equivariant features that significantly enhances both the accuracy and data efficiency of the model.[30] By extending two-body message passing to many-body interactions, MACE reduces the required number of interaction layers while

maintaining similar accuracy, thereby lowering computational costs.[31]

We train MACE on *ab initio* data generated using VASP[41, 42] with the PBE+D3(BJ) exchange-correlation (XC) functional.[43, 44] The PBE+D3(BJ) XC functional was chosen as it closely approximates RPA+HF energies and forces while requiring significantly fewer computational resources.[45, 46] Further details on *ab initio* data generation and MLP training are provided in Sec. 3.

TI accounts for anharmonicities in free energy calculations without assuming a specific form of the potential energy surface (PES).[47] In general, TI computes the Helmholtz free energy, F , difference between two states within a given simulation cell, \mathbf{h} , and temperature, T , by integrating the change in free energy along a path connecting states a and b :

$$\Delta_{a \rightarrow b}^{\text{TI}} F(\mathbf{h}, T) = \int_a^b \frac{\partial F(\lambda, \mathbf{h}, T)}{\partial \lambda} d\lambda = \int_a^b \left\langle \frac{\partial U(\lambda)}{\partial \lambda} \right\rangle_{\lambda, \mathbf{h}, T} d\lambda. \quad (1)$$

For a system with N atoms, the Helmholtz free energy is equal to $-k_B T \ln \left(\int e^{-\frac{U(\lambda, \vec{q})}{k_B T}} d\vec{q} \right)$, where k_B is the Boltzmann constant and \vec{q} a $6N$ -dimensional vector in phase space. If λ is independent of temperature, then the free energy derivative simplifies to the ensemble average of the potential energy derivative, as shown in Eq. 1. When λ represents the temperature, the free energy difference between two temperatures can be computed as:

$$\begin{aligned} \Delta_{T_1 \rightarrow T_2}^{\text{TI}} F(\mathbf{h}, T_2) &= F(\mathbf{h}, T_2) - F(\mathbf{h}, T_1) = \\ &= \left(\frac{T_2 - T_1}{T_1} \right) F(\mathbf{h}, T_1) - T_2 \int_{T_1}^{T_2} \frac{\langle U \rangle_{\mathbf{h}, T'} + \frac{3N-3}{2} k_B T'}{T'^2} dT'. \end{aligned} \quad (2)$$

A similar expression holds for the Gibbs free energy, G , by replacing the potential energy, U , with the enthalpy, H . [18]

The parameter λ can represent a physical coordinate-dependent path between two states,[48, 49] or it can serve as a hypothetical interpolation variable that gradually transforms one potential energy surface (PES) into another.[50, 19, 24, 28] For instance, starting from a harmonic PES, U_{harm} , we can linearly interpolate toward the MLP PES, U_{MLP} , by defining the path:

$$U(\lambda) = U_{\text{harm}} + \lambda(U_{\text{MLP}} - U_{\text{harm}}) \quad (3)$$

for $0 \leq \lambda \leq 1$. The Helmholtz free energy of the MLP PES can then be computed via thermodynamic integration (TI) as:

$$\begin{aligned} \Delta_{\text{harm} \rightarrow \text{MLP}}^{\text{TI}} F_{\text{MLP}}(\mathbf{h}, T) &= F_{\text{MLP}}(\mathbf{h}, T) - F_{\text{harm}}(\mathbf{h}, T) \\ &= \int_0^1 \langle U_{\text{MLP}} - U_{\text{harm}} \rangle_{\lambda, \mathbf{h}, T_0} d\lambda. \end{aligned} \quad (4)$$

The Helmholtz free energy of the harmonic PES, $F_{\text{harm}}(\mathbf{h}, T)$, can be determined analytically:[51]

$$F_{\text{harm}}(\mathbf{h}, T) = E_{\text{GS}}(\mathbf{h}) + k_{\text{B}} T \sum_{i=1}^{3N-3} \ln \left(\frac{h\nu_i(\mathbf{h})}{k_{\text{B}} T} \right), \quad (5)$$

where $E_{\text{GS}}(\mathbf{h})$ is the ground-state energy and $\nu_i(\mathbf{h})$ are the frequencies. Here, h is Planck's constant and N is the number of atoms in the system.

Finally, since the previous simulations are performed at fixed simulation cell \mathbf{h} , we convert the resulting Helmholtz free energy to the Gibbs free energy at pressure P by applying the correction

$$\begin{aligned} \Delta_{\mathbf{h} \rightarrow P} G(P, T) &= G(P, T) - F(\mathbf{h}, T) \\ &= P \text{det}(\mathbf{h}) + k_{\text{B}} T \ln \rho(\mathbf{h}|P, T), \end{aligned} \quad (6)$$

where $\rho(\mathbf{h}|P, T)$ is the probability of observing the simulation cell \mathbf{h} in an MD simulation performed at constant pressure and temperature.[18] As discussed in Sec. 3.3, the probability distribution $\rho(\mathbf{h}|P, T)$ is approximated by $\rho(V|P, T)$, since converging the full six-dimensional distribution proved computationally unfeasible.

As shown in Fig. 2, we only need these (TI) contributions to calculate the Gibbs free energy as a function of temperature. Moreover, MLPs allow TI corrections to converge with *ab initio* accuracy.[50, 52] However, this straightforward approach led to convergence issues for MHPs. Therefore, more advanced sampling techniques than standard MD are required, and an intermediate PES, U_{int} , is introduced, as discussed in more detail below.

We first explain the core issue. Namely, these difficulties arise in systems where local minima are separated by high energy barriers, limiting phase-space exploration. In such cases, standard MD simulations can become trapped in a local region of phase space, preventing reliable estimation of ensemble averages. This problem is particularly pronounced at lower temperatures, where activated processes such as octahedral tilting and organic-cation rotation occur infrequently.

To overcome these sampling limitations and ensure convergence of the ensemble averages required for TI, we employ replica exchange (REX) simulations.[37] REX involves running multiple parallel MD simulations at different temperatures, with Monte Carlo (MC) swap attempts between replicas. We restrict ourselves to temperature-based exchanges, although generalizations to varying pressures or Hamiltonians exist. Swaps are attempted at intervals comparable to the MD correlation time to ensure sufficient decorrelation between configurations.[38]

Specifically, at each swap attempt, the simulation evaluates the acceptance probability P_{accept} for exchanging the temperatures of two NVT MD trajectories, based on their instantaneous energies E_n and E_m , and temperatures T_n and T_m :

$$P_{\text{accept}} = \min \left(1, \exp \left[\left(\frac{1}{k_{\text{B}} T_n} - \frac{1}{k_{\text{B}} T_m} \right) (E_n - E_m) \right] \right). \quad (7)$$

For NPT MD simulations conducted at the same pressure, the acceptance probability retains the same form as in Eq. 7, with the energy replaced by the enthalpy.[53]

An important advantage of the MC swaps is that they connect the phase space sampled by MD trajectories at different temperatures. The enhanced exploration of phase space at higher temperatures can thus assist lower-temperature simulations in escaping local minima. Through these swaps, energy barriers that are rarely crossed at low temperatures can be effectively overcome if they are frequently traversed at higher temperatures. As a result, REX simulations are employed to improve sampling for the TI contribution along the temperature integration path. Additional details regarding the REX implementation are provided in Sec. 3.3.

This sampling challenge also affects the TI correction between the harmonic and MLP PES, as it is evaluated at low temperature. Performing REX simulations for all λ values between 0 and 1 would substantially increase the computational cost. Fortunately, this is not required: for small λ values, sampling only needs to cover the vicinity of the harmonic minimum. For large λ values, the potential is dominated by the MLP PES, and sampling at elevated temperatures becomes more appropriate, as the system can more readily overcome energy barriers. In contrast, at small λ , low-temperature sampling remains essential to avoid exploring unphysical regions of the PES that arise from the breakdown of the harmonic approximation.

To construct a continuous path between these two regimes, low λ at low temperature and high λ at high temperature, we introduce the intermediate PES, U_{int} . This PES provides a better approximation to the MLP PES than the harmonic PES, avoiding its breakdown at higher temperatures while retaining the harmonic minima as the dominant contribution at low temperature. A practical choice is $U_{\text{int}} = U(0.7) = 0.3 U_{\text{harm}} + 0.7 U_{\text{MLP}}$, alternative intermediate PESs are discussed in Sec. 3.3.

Fig. 2 schematically summarizes the required free energy contributions. We start from the ground state energy, E_{GS} (contribution 1), and compute the static harmonic free energy, $F_{\text{harm,stat}}$ (contribution 2). Rather than directly applying a TI correction from the harmonic to the MLP PES, we first evaluate a TI correction from the harmonic to the intermediate PES at low temperature, T_{low} , where the harmonic approximation is more accurate (contribution 3). Next, a TI along a temperature path is performed for the intermediate PES using REX simulations to ensure convergence of the ensemble averages (contribution 4). Finally, a TI correction from the intermediate to the MLP PES is applied at high temperature, T_{high} , where sampling is more efficient (contribution 5).

The full temperature dependence of the Helmholtz free energy is then obtained by (see contributions 2 to 6 in Fig. 2):

$$\begin{aligned} F_{\text{MLP}}(\mathbf{h}, T) &= F_{\text{harm}}(\mathbf{h}, T_{\text{low}}) \\ &+ \Delta_{\text{harm} \rightarrow \text{int}}^{\text{TI}} F_{\text{int}}(\mathbf{h}, T_{\text{low}}) \\ &+ \Delta_{T_{\text{low}} \rightarrow T_{\text{high}}}^{\text{TI}} F_{\text{int}}(\mathbf{h}, T_{\text{high}}) \\ &+ \Delta_{\text{int} \rightarrow \text{MLP}}^{\text{TI}} F_{\text{MLP}}(\mathbf{h}, T_{\text{high}}) \\ &+ \Delta_{T_{\text{high}} \rightarrow T}^{\text{TI}} F_{\text{MLP}}(\mathbf{h}, T) \end{aligned} \quad (8)$$

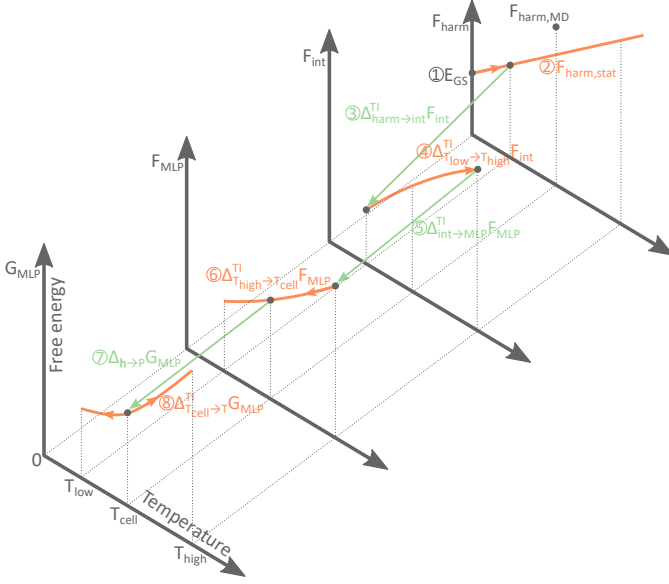


Figure 2: Visualization of the free-energy contributions required to obtain the Gibbs free energy as a function of temperature. Starting from the ground-state energy, E_{GS} , we calculate the static harmonic free energy, $F_{harm,stat}$. The Helmholtz free energy is evaluated at the average cell \mathbf{h} obtained from an NPT MD simulation at temperature T_{cell} and pressure P , i.e., the pressure at which the Gibbs free energy is desired. A TI contribution at T_{low} corrects for anharmonic effects, yielding $F_{int}(\mathbf{h}, T_{low})$, followed by a TI contribution along a temperature path to T_{high} and a TI correction from the intermediate to the MLP PES, giving $F_{MLP}(\mathbf{h}, T_{high})$. To obtain G_{MLP} , a TI contribution is first performed from T_{high} to T_{cell} , followed by the correction $\Delta_{\mathbf{h} \rightarrow P}$, and finally a TI contribution from T_{cell} to any temperature T . The previously reported $F_{H,MD}$ is shown for comparison.[16]

In principle, the Gibbs free energy can be computed using Eq. 6, provided that the Helmholtz free energy is known for an arbitrary simulation cell (contribution 7). However, obtaining accurate probabilities for simulation cells that deviate significantly from the average cell in an NPT MD simulation at the target pressure and temperature is computationally unfeasible. Therefore, the Helmholtz free energy is evaluated at the temperature T_{cell} (contribution 6) at which the average simulation cell (used for the Helmholtz free energy calculation) was determined.

To avoid repeating Helmholtz free energy calculations for the average cell at each temperature, we perform NPT REX simulations, from which the Gibbs free energy as a function of temperature can be obtained via TI along a temperature path (contribution 8). The full temperature dependence of the Gibbs free energy is then given by (see contributions 6 to 8 in Fig. 2):

$$G_{MLP}(P, T) = F_{MLP}(\mathbf{h}, T_{cell}) + \Delta_{\mathbf{h} \rightarrow P} G_{MLP}(P, T_{cell}) + \Delta_{T_{cell} \rightarrow T}^{TI} G_{MLP}(P, T), \quad (9)$$

with \mathbf{h} the average simulation cell in a NPT MD simulation at pressure P and temperature T_{cell} .

Additionally, we perform NVE MD simulations to extract vibrational frequencies and compute the Helmholtz free energy

(see $F_{harm,MD}$ in Fig. 2), as described in our previous work.[16] The free energies obtained from this method and our present approach are compared in Sec. 4.2.

This methodology assumes classical motion of the atomic nuclei. Quantum nuclear effects (QNE) can be incorporated through an alternative TI scheme,[54] but this lies beyond the scope of the present work. In Sec. 1 of the Supporting Information (SI), we investigate the difference between the harmonic free energy calculated using the classical partition function (see Eq. 5) and the quantum mechanical partition function. As expected, the differences are small, since the high-frequency vibrational modes, which are most sensitive to quantum effects, are associated with the organic molecules, and these modes are similar across the three phases considered.

3 COMPUTATIONAL DETAILS

3.1 Density functional theory benchmark

Because the ground state energy strongly influences the phase transition temperature, we assessed the accuracy of the energy and forces predicted by various XC functionals and dispersion corrections by benchmarking them against RPA+HF results. We used the same XC functionals, dispersion methods, and computational settings as in our previous study,[16] and extended the benchmark to include the organic MHPs: FAPbI₃ and MAPbI₃. In addition to energies, forces were also benchmarked, as they are directly used in training the MLP. To ensure meaningful force comparisons, we evaluated randomly selected structures from NPT MD simulations rather than optimized structures, which have near-zero forces by definition. RPA+HF forces were calculated in VASP using Green’s function theory,[46] and their convergence was verified, as discussed in Sec. 2 of the SI.

3.2 Training of the machine learning potentials

3.2.1 Ab initio data generation

To generate the dataset, we first performed NVT *ab initio* MD simulations at 800 K using CP2K.[55, 56] The simulations employed the PBE XC functional with D3(BJ) dispersion corrections.[43, 44] CP2K utilizes a mixed Gaussian and plane-wave basis, and we used GTH pseudopotentials in combination with TZVP-MOLOPT-SR-GTH basis sets. The plane-wave cutoff and relative cutoff were set to 400 Ry and 40 Ry, respectively. Each simulation box contained 64 formula units (fu), and only the Γ -point was used for Brillouin zone sampling.

For each material and each phase, MD simulations were performed at 22 different volumes to generate training structures for the MLP, and at 5 additional volumes to generate validation and test structures. A volume range of approximately $\pm 10\%$ around the average volume at 300 K was uniformly sampled. Initial configurations were extracted from an NPT MD simulation at 800 K and 0.1 MPa; one structure was selected every 100 ps and isotropically scaled to the desired volume. For FAPbI₃ and MAPbI₃, the organic molecules were additionally subjected to random rotations to reduce correlations between the NVT MD simulations and to ensure a more uniform sampling of the phase space. During the NVT and NPT simulations with CP2K, a Nosé-Hoover thermostat with a time constant of 100 fs and three thermostat beads was used to control the temperature.[57, 58, 59] For the NPT simulations, the pressure was maintained using a Martyna-Tuckerman-Klein (MTK) barostat with a time constant of 500 fs.[60]

We performed 1000 steps for each NVT MD simulation, using a time step of 2 fs for CsPbI₃ and 0.5 fs for FAPbI₃ and MAPbI₃. From each MD simulation in the training dataset, 6 structures were uniformly selected. For the validation and test datasets, 2 structures were selected from each of the five MD simulations at the additional volumes for validation, and 2 different structures were selected for testing. Three separate MLPs were trained, one for each material. By combining the structures from all phases of a given material, we constructed datasets consisting of 396 training structures, 30 validation structures, and 30 test structures.

The initial dataset was sufficient to train MLPs that accurately reproduced the *ab initio* PES sampled at temperatures up to 600 K. However, our TI approach also requires sampling the harmonic (Hessian) PES at lower temperatures, specifically 150 K. While the MLPs were generally accurate for most structures generated during MD on the Hessian PES, a few outlier structures exhibited large prediction errors, which strongly affected the ensemble averages required for the free energy calculation (see Eq. 4). To address this, we developed new MLPs for each material by augmenting the original training dataset with 48 additional structures sampled from NVT MD simulations on the Hessian PES at 150, 245, 383, and 600 K for all three phases. For each phase and temperature, seven structures were added to the training set and one to the validation set. These updated MLPs were then used to compute the true and Hessian PES across the relevant temperature range.

Before training the MLPs, all structures in the dataset were recalculated using VASP[41, 42], which yields low net forces,[61] with the PBE+D3(BJ) XC functional.[43, 44] The following PAW potentials[62] were employed: H (1s¹), C (2s²2p²), N (2s²2p³), Cs_{sv} (5s²5p⁶6s¹), Pb_d (5d¹⁰6s²6p²), and I (5s²5p⁵). A Γ -centered $2 \times 2 \times 2$ k-point grid and a plane-wave cutoff energy of 500 eV were used. This recalculation step was necessary because the CP2K-predicted energy differences between phases differed from the VASP values by several kJ/mol. Moreover, the phase energy differences obtained with PBE+D3(BJ) in VASP show good agreement with the RPA+HF reference values, as discussed in Sec. 4.1.

The CP2K MD input files and the VASP single-point calculation input files are available at <https://doi.org/10.5281/zenodo.18108633>.

3.2.2 Architecture of the machine learning potentials

The MACE architecture with a cut-off radius of 6 Å was used to train the MLP. We employed the psiflow software package (version 1.0.0),[63] and adapted several settings of the MACE architecture as implemented in psiflow; these are listed in Tab. 1. The input files used for MLP training are available at <https://doi.org/10.5281/zenodo.18108633>. This relatively small network could be evaluated on 1 cpu core. The evaluation time per structure for 8 and 64 fu simulation cells of CsPbI₃ was 32 and 183 ms, respectively. For the organic MHPs, the corresponding evaluation times were 86 and 685 ms. These fast evaluation times are essential, as more than 200 million MD steps are required to compute the Gibbs free energy of a single system (see next subsection).

Table 1: Non-default settings of the applied MACE architecture used for MLP training

Setting	Value
r_max	6.0
max_e11	2
num_channels	8
lr	0.02
max_num_epochs	300
ema	True

For the MLPs trained on the CsPbI₃, FAPbI₃, and MAPbI₃ datasets (including the Hessian structures), the test set energy errors were 0.4, 0.3, and 0.2 meV/atom, respectively, while the corresponding force errors were 25.6, 28.7, and 24.3 meV/Å. These root mean square errors (RMSEs) are significantly smaller than the standard deviations of the respective test sets, which were 18.4, 6.8, and 5.8 meV/atom for the energies and 358.5, 1175.8, and 1068.3 meV/Å for the forces.

3.3 Workflow

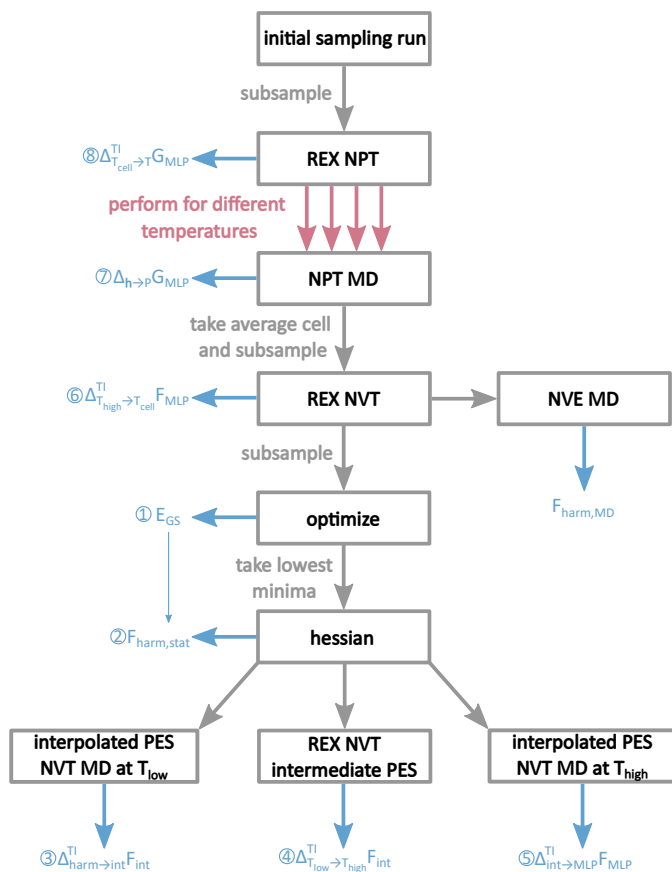


Figure 3: Flowchart to derive the Gibbs free energy of a phase. The numbers next to the contributions indicate the order in which they are theoretically added, as depicted in Fig. 2. As explained in our previous work,[16] the harmonic free energy at a specific temperature can also be determined via an additional NVE MD simulation.

The PES of MHPs contains numerous local minima, which hampers the convergence of the ensemble averages required

for free energy calculations. To obtain converged values, we perform multiple MD simulations in parallel and employ replica exchange (REX) simulations. To accelerate convergence, it is important that parallel simulations are initialized from distinct random structures that are still thermodynamically relevant at the conditions of interest. Each contribution depicted in Fig. 2 requires a separate calculation, and the sampling from one step is used to generate the initial structures for the next. The general workflow is illustrated in Fig. 3. All calculations in this workflow are performed using the trained MLPs, as discussed in Sec. 3.2.

First, we define the temperature range of interest. The MD simulation at the highest temperature should be able to easily escape local minima and efficiently explore the entire PES of the phases of interest. The lowest temperature is ideally chosen to be as low as possible, but is constrained by the number of replicas and the acceptance probability of the Monte Carlo exchanges in the REX simulations. For all MHPs investigated, we use 32 temperatures ranging from 150 K to 600 K. The temperatures follow a geometric progression ($\frac{T_{i+1}}{T_i} = \text{constant}$) to ensure that all replica swaps have a similar acceptance ratio.[38]

We begin with a short NPT MD simulation at the highest temperature (600 K) and 0.1 MPa to generate 32 distinct initial structures for the REX NPT simulations. The REX NPT simulation couples 32 MD simulations at different temperatures under constant pressure (0.1 MPa). From this simulation, the temperature-dependent free energy contribution, $\Delta_{T_{\text{cell}} \rightarrow T}^{\text{TI}} G_{\text{MLP}}(P, T)$, can be computed.

In principle, the $\Delta_{\mathbf{h} \rightarrow P} G_{\text{MLP}}(P, T_{\text{cell}})$ correction could be determined by selecting one temperature, calculating the average simulation cell, and evaluating the corresponding $\Delta_{\mathbf{h} \rightarrow P} G_{\text{MLP}}(P, T_{\text{cell}})$ correction. However, accurately sampling $\rho(\mathbf{h}|P, T)$ is challenging because the cell shape matrix \mathbf{h} is six-dimensional. To reduce complexity, we instead approximate it using the volume probability distribution $\rho(V|P, T)$. Moreover, at low temperatures, \mathbf{h} may exhibit multiple minima due to different octahedral tilt patterns. To obtain a meaningful average structure, a separate NPT MD simulation is performed at each temperature, as the cell parameters tend to remain in a local minimum at low temperature. The average cell from this simulation is used, and the probability of the corresponding volume, $\rho(V|P, T)$, is used to compute $\Delta_{\mathbf{h} \rightarrow P} G_{\text{MLP}}(P, T_{\text{cell}})$. To assess the impact of the approximations made, this correction (and the associated Helmholtz free energy $F_{\text{MLP}}(\mathbf{h}, T_{\text{cell}})$) is evaluated at eight different temperatures: 150, 187, 234, 293, 350, 419, 501, and 600 K.

Due to the rough PES with numerous local minima, we first explore the PES and subsequently perform multiple geometry optimizations. To generate a relevant set of structures for optimization, MD simulations are preferably performed at the lowest temperature. However, to escape local minima and ensure broad sampling of the PES, MD simulations at the highest temperature are necessary. To achieve both objectives, we perform REX NVT simulations and extract 4000 structures from the replica at the lowest temperature for geometry optimization. Moreover, the REX NVT simulations enable the calculation of the free energy contribution $\Delta_{T_{\text{high}} \rightarrow T_{\text{cell}}}^{\text{TI}} F_{\text{MLP}}(\mathbf{h}, T_{\text{cell}})$. From the set of optimized structures, the one with the lowest energy is selected, and its

Hessian is computed. This Hessian is then used to determine the harmonic free energy as a function of temperature.

For CsPbI₃, we use an intermediate PES defined as $0.3U_{\text{harm}} + 0.7U_{\text{MLP}}$. For FAPbI₃ and MAPbI₃, the intermediate PES corresponds to the MLP PES augmented with a bias potential. This bias potential constrains the orientation of the organic molecules, effectively fixing them during simulations on the intermediate PES. As a result, only the minima of the harmonic PES are sampled, which circumvents convergence issues that typically arise at low temperatures. Details about the construction and implementation of the bias potential are provided in Sec. 3 of the SI.

REX NVT simulations at various temperatures are performed on the intermediate PES to compute the thermodynamic integration (TI) correction $\Delta_{T_{\text{low}} \rightarrow T_{\text{high}}}^{\text{TI}} F_{\text{int}}(\mathbf{h}, T_{\text{high}})$. In addition, interpolated PESs between the Hessian PES and the intermediate PES are constructed to perform MD simulations at the lowest temperature, yielding the TI correction $\Delta_{\text{harm} \rightarrow \text{int}}^{\text{TI}} F_{\text{int}}(\mathbf{h}, T_{\text{low}})$. Similarly, MD simulations between the intermediate and MLP PES are used to compute the correction $\Delta_{\text{int} \rightarrow \text{MLP}}^{\text{TI}} F_{\text{MLP}}(\mathbf{h}, T_{\text{high}})$. For both TI corrections, 14 intermediate PESs were constructed using Eq. 3, with the following λ values: 0.0, 0.01, 0.02, 0.05, 0.1, 0.2, 0.4, 0.6, 0.8, 0.9, 0.95, 0.98, 0.99, and 1.0.

To investigate the effect of supercell size, shorter MD simulations were performed using simulation cells containing 64 fu instead of 8. Because the phase space is considerably larger for the bigger cell, the final structure from the 8 fu MD simulations was used as the initial structure for the $2 \times 2 \times 2$ supercell to reduce equilibration time. To reduce the overall computational cost, the Helmholtz free energy, $F_{\text{MLP}}(\mathbf{h}, T_{\text{cell}})$, for 64 fu was calculated using the average cell at only three temperatures: 234 K, 350 K, and 501 K.

All structural optimizations were carried out with ASE[64] using the PreconLBFGS optimizer[65]. MD simulations and Hessian calculations were performed with Yaff.[66] Temperature and pressure were controlled with a Langevin thermostat and barostat,[67, 68] using a timestep of 2 fs for CsPbI₃ and 0.5 fs for FAPbI₃ and MAPbI₃. Multiple parallel MD simulations were performed for each contribution, resulting in nearly 220 million MD steps required to compute the Gibbs free energy of a single material at a given system size. The exact number of simulation steps for each contribution is provided in the simulation scripts available at <https://doi.org/10.5281/zenodo.18108633>.

4 RESULTS

4.1 Benchmarking XC functionals with RPA+HF

We benchmarked the energies and forces predicted by various XC functionals and dispersion corrections for CsPbI₃, FAPbI₃, and MAPbI₃. For each material and each of the three phases, five representative structures were randomly selected from NPT MD simulations at 600 K and 0.1 MPa using a simulation cell containing four fu, resulting in a total of 45 structures for the energy evaluation. Given the high computational cost of RPA+HF force calculations, a subset of two structures per phase and material (*i.e.*, 18 in total) was selected for force benchmarking.

The mean absolute errors (MAEs) of the DFT energies with respect to the RPA+HF reference are shown in Fig. 4. With the exception of vdW-DF2 and a few outliers for CsPbI₃, most XC

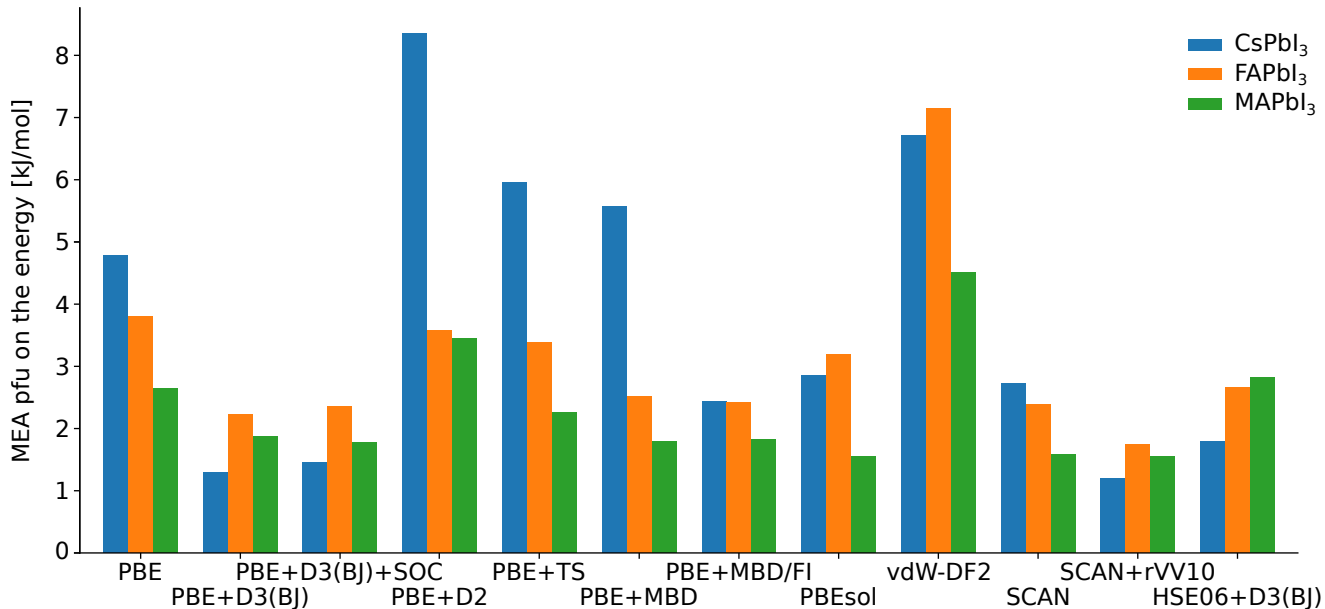


Figure 4: Mean absolute error of the DFT energies using different XC functionals and dispersion corrections with respect to RPA+HF.

functionals and dispersion schemes yield comparable accuracy. Among these, SCAN+rVV10 achieves the lowest MAE of 1.5 kJ/mol per formula unit (pfu), demonstrating the best agreement with RPA+HF.[69] PBE+D3(BJ) also performs well, with an average MAE of 1.8 kJ/mol pfu.

A similar benchmark performed on optimized structures is presented in Sec. 4 of the SI and yields consistent trends. Furthermore, for several optimized structures used in the thermodynamic integration procedure, we compared the MLP-predicted energies with PBE+D3(BJ) values, finding deviations smaller than 1 kJ/mol pfu.

The RMSEs of the forces between the different levels of theory are shown in Fig. 5. Variations in the dispersion correction have only a minor effect on the computed forces. For the PBE XC functional, the largest deviations occur when using the D2 dispersion correction, primarily due to inaccuracies in the forces on Cs atoms. In contrast, adding D3(BJ), SOC, or MBD/FI dispersion corrections to PBE does not significantly alter the force predictions compared to PBE without dispersion.

Similarly, SCAN, SCAN+rVV10, and HSE06+D3(BJ) show good mutual agreement, indicating internal consistency among these functionals. In contrast, vdW-DF2 stands out as a clear outlier, yielding large RMSEs in the forces when compared to all other methods. While PBEsol exhibits better agreement than vdW-DF2, it still shows RMSEs exceeding 170 meV/Å with respect to the other functionals, indicating notable discrepancies.

No XC functional or dispersion method shows significantly better agreement with RPA+HF for the atomic forces. Among the tested methods, PBE+D3(BJ) yields the lowest overall RMSE of 260 meV/Å, while PBEsol results in the highest RMSE of 381 meV/Å. However, a breakdown of the RMSE by atomic species reveals considerable variation. Specifically, the errors on the C

and N atoms are substantially larger than those on Cs, Pb, and I atoms. This discrepancy may be attributed to the delocalized electronic charge distribution on the C and N atoms in the FA and MA molecules, which standard DFT functionals often fail to accurately describe.[70, 71] Furthermore, the RMSE is slightly higher for the C and N atoms of FA compared to those of MA, possibly because the electronic charge in FA is more delocalized than in MA.

While the total RMSE of the atomic forces with respect to RPA+HF is comparable across GGA, mGGA, and hybrid XC functionals, significant differences arise when partitioning the error between organic and inorganic atoms. The mGGA and hybrid functionals yield RMSE values below 85 meV/Å for the inorganic atoms, whereas the RMSE on the organic atoms can exceed 850 meV/Å. In contrast, the PBE+D3(BJ) functional results in higher RMSE values for the inorganic atoms, up to 140 meV/Å. However, it provides a more accurate description of the forces on the organic species.

In general, we expect that the atomic dynamics predicted by most DFT methods, when compared to RPA+HF, primarily differ in the internal vibrational modes of the FA and MA molecules. These modes are present in all three phases. Consequently, the large force errors observed on the organic atoms are not expected to significantly impact the free energy differences between phases, due to a cancellation of errors.

We opted to train the MLPs on PBE+D3(BJ) energies and forces computed with VASP[41, 42], as this functional yields one of the best agreements with RPA+HF while being computationally less demanding than alternatives such as SCAN+rVV10. Furthermore, the PBE functional is known to produce less noisy forces compared to many other XC functionals.[72]

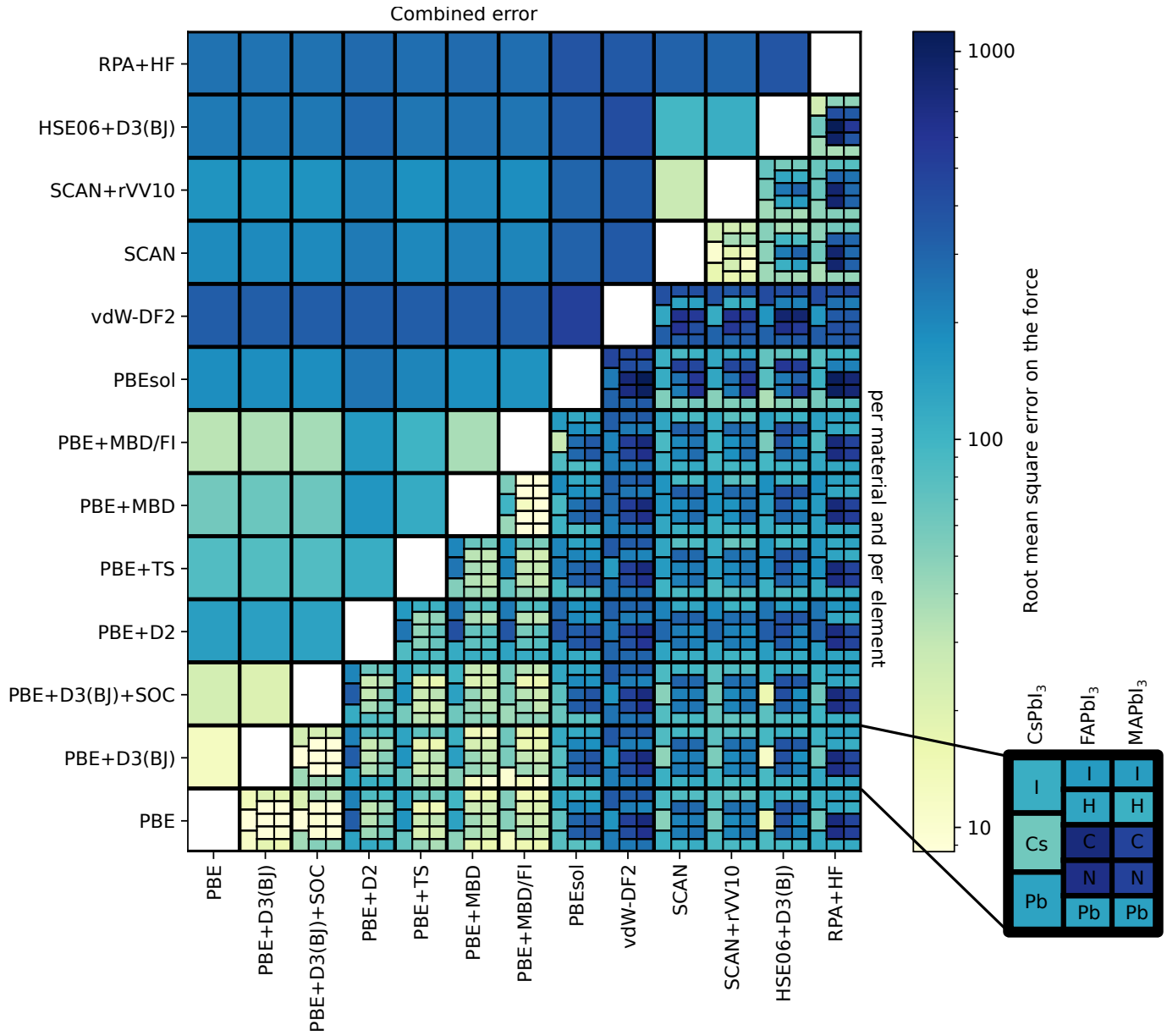


Figure 5: Root mean square error of the atomic forces between different XC functionals, dispersion methods, and RPA+HF calculations. The top left shows the total RMSE across all atoms from two benchmark structures per phase and material. The bottom right breaks down the RMSE by material and atomic species.

4.2 Free energy as a function of temperature

By performing the simulations outlined in Fig. 3 with the trained MLP, the four temperature-dependent free energies shown in Fig. 2 can be computed. As detailed in Sec. 5 of the SI, each simulation step contributes to the total free energy and can be analyzed independently. Fig. 6 presents the four free energy curves as a function of temperature for CsPbI₃, FAPbI₃, and MAPbI₃. For all MHPs, the δ phases are stabilized by enthalpy, whereas the γ phase is stabilized by entropy.[73]

The bottom panel for each material shows the harmonic free energy. This quantity can be computed using two different methods: from the vibrational frequencies obtained from the Hessian of the ground state structure (solid lines), and from the velocities in NVE MD simulations (dotted lines).[16] For CsPbI₃, both approaches yield consistent results, indicating good agreement. However, for FAPbI₃ and MAPbI₃, the harmonic free energy derived from the velocities of the NVE MD simulations is less accurate and fails to converge. As discussed in Sec. 7 of the SI, this discrepancy arises due to the presence of numerous inequivalent local minima introduced by the organic molecules. These contribute to poor convergence of the frequencies and, consequently, the harmonic free energy when derived from MD trajectories.

The intermediate PES is designed to incorporate anharmonic effects while remaining constrained to the region near the global energy minimum. Comparison of the bottom panel with the panel above shows that this correction is small and tends to stabilize the δ phases relative to the γ phase at elevated temperatures.

The correction from the intermediate to the MLP PES includes the contribution from configurational entropy. Comparison of the second and third panels shows that this correction slightly destabilizes the δ_{FA} phase and significantly destabilizes the δ_{CS} phase. These results suggest that the γ phase has access to a larger number of local minima than the δ_{FA} phase, which in turn has more than the δ_{CS} phase. Interestingly, for MAPbI₃, the correction destabilizes the γ phase at low temperatures, indicating that some local minima become accessible only at elevated temperatures (see also Sec. 4.3).

To calculate the Helmholtz free energy, we used eight different simulation cells, resulting in a spread indicated by the shaded area in Fig. 6. This best estimate, shown as solid lines, corresponds to the average NPT MD simulation cell at the temperature closest (on a logarithmic scale) to the one considered. Using Eq. 6, we applied a correction to convert the Helmholtz free energies into Gibbs free energies for all eight cells (top panel). Ideally, this correction should collapse the spread, since all Gibbs free energies at a given (P, T) should be equal. However, the spread remains comparable, likely because the correction is based on the volume distribution $\rho(V|P, T)$ rather than the full six-dimensional cell distribution $\rho(\mathbf{h}|P, T)$.

The experimental transition temperature of CsPbI₃ from the δ_{CS} to the γ phase ranges from 548 K to 599 K, in good agreement with the prediction from the TI approach. For FAPbI₃, the experimental transition from the δ_{FA} to the γ phase occurs between 433 K and 458 K, with the TI method slightly overestimating this value.[74, 75, 76, 77, 78] In the case of MAPbI₃, the γ phase is experimentally stable at room temperature, which is not

reproduced by the TI predictions. Nevertheless, the free energy differences between the three phases at room temperature are very small, suggesting that only a modest correction would be required to align the predictions with experimental observations.

Based on the limited experimental data for the temperatures at which the free energy of two phases are the same, we conclude that the TI approach predicts small free energy differences at the experimental transition temperatures. However, there is some degree of error cancellation, as the free energy difference relative to the γ phase decreases when using a supercell containing 64 fu (see Sec. 8 of the SI). This results in free energy differences at the experimental transition temperatures that are approximately 2 kJ/mol pfu too low, which may stem from inaccuracies in the PBE+D3(BJ) XC functional. Additional sources of error could include insufficient sampling of the phase space, convergence issues, or the neglect of quantum nuclear effects. Moreover, experimental factors such as the presence of defects may also influence the observed transition temperatures.

4.3 A-site effect on the free energy

To investigate the effect of the A-site cation on the free energy, we analyze six contributions to the Helmholtz free energy. Fig. 7 presents the ground-state energy of the global minima, the two λ -TI corrections, and the difference in Helmholtz free energy between 600 K and 150 K for the three different PES.

The top-left panel shows the ground-state energy and is strongly influenced by the A-site cation, with a pronounced difference between CsPbI₃ and the organic MHPs. The δ_{CS} phase is significantly more stable in CsPbI₃, whereas the δ_{FA} phase is favored in the organic MHPs, with FAPbI₃ exhibiting slightly greater stability in this phase compared to MAPbI₃. The cell has a notable impact, particularly for the organic MHPs, where the average cells at elevated temperatures tend to destabilize the γ phase.

As shown in the top-right panel of Fig. 7, the harmonic free energy differences show the opposite trend, stabilizing the γ phase at elevated temperatures. For the δ_{CS} phase, this stabilization is more pronounced in CsPbI₃, while for the δ_{FA} phase, it is stronger in the organic MHPs. TI corrections to the intermediate PES and their temperature dependence shown by the middle panels in Fig. 7, introduce only minor changes to the harmonic free energy across all materials, slightly reducing cell size dependence and destabilizing the γ phase.

The correction to the MLP PES is reported in the bottom-left panel of Fig. 7 and includes configurational entropy, which has a significant influence on the total free energy. All three materials share the same PbI framework, whose flexibility is most easily analyzed in CsPbI₃. For instance, when considering the γ phase of CsPbI₃ using a simulation cell with eight fu at 600 K, all but one of the 4000 sampled structures optimize to the same energy, as shown in Sec. 7 of the SI. However, this does not imply that they converge to the same point in phase space. Due to the various possible octahedral tilting directions and axes, multiple distinct local minima can exist with nearly identical energies.[79] A comparison of the distance matrices of the atomic positions across all optimized structures revealed 25 unique configurations, indicating that the γ phase contains 24 equivalent minima. In contrast, only one unique configuration

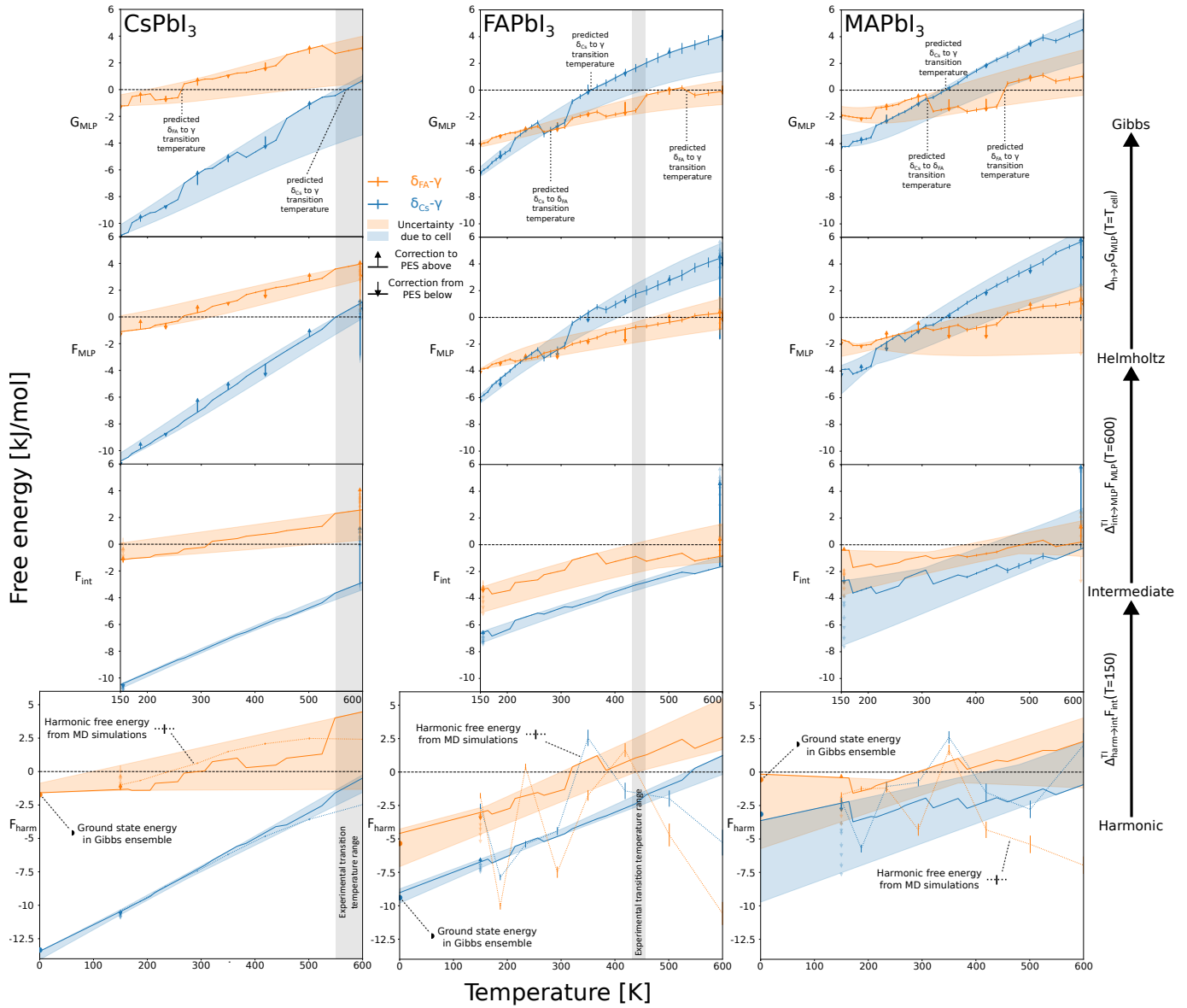


Figure 6: Free energy difference of the δ_{Cs} (blue) and δ_{FA} (orange) phases relative to the γ phase as a function of temperature, computed using different PES: harmonic (via NVE MD simulations, dashed lines, and via Hessian calculations, solid lines with shaded areas), intermediate, and MLP. The Helmholtz and Gibbs free energies for the MLP PES are obtained from MD simulations in the NVT and NPT ensembles, respectively. All results correspond to simulation cells containing eight fu of CsPbI₃, FAPbI₃, and MAPbI₃. For the NVT simulations, eight independent simulation cells were used; the shaded areas represent the range between the minimum and maximum values. The solid lines depict the free energy computed for the average NPT MD simulation cell at the temperature closest to the corresponding x-axis value on a logarithmic scale. The arrows originating from the solid lines represent corrections to the free energy plotted above, while the arrows pointing toward the solid lines represent corrections arising from the free energy plotted below.

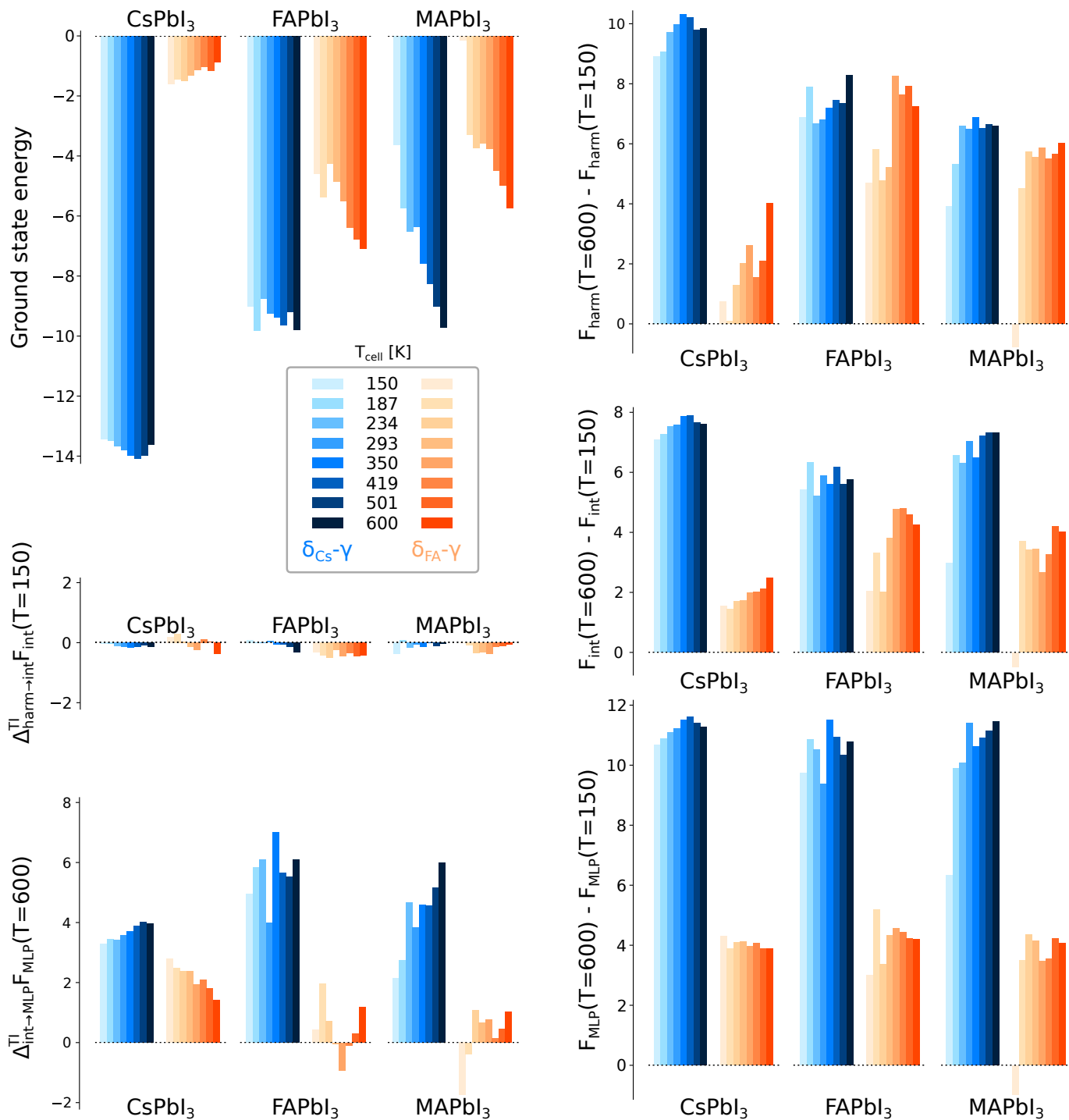


Figure 7: Contributions to the total Helmholtz free energies (in kJ/mol pfu) calculated for average simulation cells at eight different temperatures T_{cell} , as described in Eq 8. The energy differences of the δ phases relative to the γ phase are shown; positive values indicate stabilization of the γ phase. The left panel presents the ground-state energies and the λ -TI corrections for the intermediate and MLP PES. The right panel illustrates the temperature-dependent free energy changes for the harmonic, intermediate, and MLP PES.

was identified for the δ_{Cs} phase, and six configurations with approximately the same energy were found for the δ_{FA} phase.

The contribution of configurational entropy to the free energy can be estimated by taking the natural logarithm of the number of distinct minima and multiplying by $k_{\text{B}}T$. At 600 K, this results in a destabilization of the δ_{Cs} phase by approximately 1.2 kJ/mol pfu relative to the δ_{FA} phase, and 2 kJ/mol pfu relative to the γ phase. These values are slightly lower than $\Delta_{\text{int} \rightarrow \text{MLP}}^{\text{TI}} F_{\text{MLP}}(\mathbf{h}_{600}, T = 600)$ shown in Fig. 7, as the latter also accounts for contributions from higher-energy minima and anharmonic effects.

The configurational entropy is influenced by the size of the supercell. For the configurational entropy to scale linearly with system size, the number of accessible minima must scale exponentially. This condition is not met for the γ phase of CsPbI_3 , as octahedral tilts in one part of the structure constrain the tilts in neighboring regions. While larger supercells can accommodate more local minima through irregular tilting patterns, these configurations generally have higher energies. As a result, normalizing the configurational entropy contribution pfu leads to a relative destabilization of the γ phase when increasing the system size, see Sec. 8 of the SI. In contrast, this destabilizing effect is not observed for the δ_{FA} phase compared to the δ_{Cs} phase, indicating that the number of energetically relevant minima in the δ_{FA} phase scales exponentially with system size.

The rotational freedom of the organic molecules generates a significantly larger number of local minima, as shown in Sec. 7 of the SI. By comparing the $\Delta_{\text{int} \rightarrow \text{MLP}}^{\text{TI}} F_{\text{MLP}}(\mathbf{h}_{600}, T = 600)$ contributions for FAPbI_3 and CsPbI_3 (*i.e.*, the dark blue bars of both materials and the dark red bars in the bottom-left panel of Fig. 7), we infer that the FA molecule exhibits reduced rotational freedom in the δ_{Cs} phase and enhanced rotational freedom in the δ_{FA} phase relative to the γ phase. A similar trend is observed for the MA molecule, although the cell dependence is significantly more pronounced for MAPbI_3 .

To understand the effect of the cell, we investigate the orientational freedom of the organic molecules by tracking the vector defined by the carbon and nitrogen atoms of a MA molecule. Fig. 8 presents the orientation distributions for three MA molecules in the γ phase of MAPbI_3 during NVT MD simulations at various temperatures and for different simulation cell sizes.

Instead of the spread of the orientation distributions, we investigate correlations between the orientations of different molecules, as these can strongly affect the number of energetically relevant minima and, consequently, the configurational entropy. If the orientations are perfectly correlated, the number of minima is determined by a single molecule, and the configurational entropy does not increase with system size. Conversely, if molecular orientations are independent, adding a molecule with two possible orientations doubles the number of minima, and the configurational entropy grows accordingly.

To visualize correlations between different molecules, the RGB color of each dot in Fig. 8 is determined by the x , y , and z components of the orientation vector of a reference MA molecule. As defined, the dots on the reference molecule’s sphere are colored by position: red for the left and right sides, blue for the top and bottom, and green for the front. The orientations of two other investigated MA molecules in the simulation cell (one nearby and

one distant from the reference) are also plotted using the color defined by the reference molecule. If dots of the same color cluster on the spheres of the other molecules, their orientations are correlated with that of the reference molecule. Conversely, if a color is scattered across the sphere, the orientations are uncorrelated.

As shown in the top-left panel of Fig. 8, in the average cell of the lowest temperature, the orientation of the reference molecule is correlated with that of both nearby and distant MA molecules, indicating strong orientational coupling. This is consistent with observations by Escorihuela-Sayalero *et al.*[80, 81] This coupling restricts the number of energetically relevant minima. At higher temperatures and in larger simulation cells, each color is more uniformly distributed for the neighboring molecules, suggesting reduced influence from the reference molecule’s orientation. In the absence of such coupling, the number of accessible minima is expected to scale exponentially with system size, contributing significantly to the configurational entropy. As discussed in Sec. 9 of the SI, for other phases and for FAPbI_3 , the orientation of one molecule can give rise to multiple orientations of surrounding molecules, even at low temperatures and in small simulation cells. This strong temperature and cell-size dependence of the orientational entropy in the γ phase of MAPbI_3 explains the pronounced curvature in the free energy differences shown in Fig. 7, which is even more pronounced in the supercell simulations (see Sec. 8 of the SI).

Remarkably, the temperature dependence of the Helmholtz free energy differences between the phases (shown in the bottom-right panel of Fig. 7) is similar for all three materials, with the exception of the smallest simulation cell of the γ phase of MAPbI_3 , where the configurational free energy is reduced due to hindered orientational freedom of the MA molecules. The free energy difference between the δ_{Cs} and γ phases increases by approximately 2.4 kJ/mol per 100 K, while for the δ_{FA} and γ phases this increase is about 0.9 kJ/mol per 100 K. For larger supercells, these values are slightly lower due to additional destabilization of the γ phase, as discussed in Sec. 8 of the SI. These trends can be used to estimate the transition temperature based on the ground state energy differences. However, due to the strong cell dependence, the ground state energy should be evaluated using the average simulation cell at the estimated transition temperature. It is also important to note that this apparent similarity in temperature dependence arises from the combined effect of harmonic, anharmonic, and configurational contributions to the free energy. These individual components vary significantly between CsPbI_3 and the organic MHPs, so caution should be exercised when generalizing this trend.

5 CONCLUSIONS

MHPs are complex materials that require computationally demanding *ab initio* methods to accurately capture their energies and forces. In addition, their structural flexibility gives rise to strong anharmonic effects and a rich landscape of local minima. By employing MLPs, we can efficiently reproduce *ab initio*-level energies and forces, enabling MD simulations to compute Gibbs free energies using a TI based methodology.

In this work, we benchmark a range of XC functionals and dispersion corrections for their ability to reproduce the RPA+HF energies and forces of CsPbI_3 , FAPbI_3 , and MAPbI_3 . Several

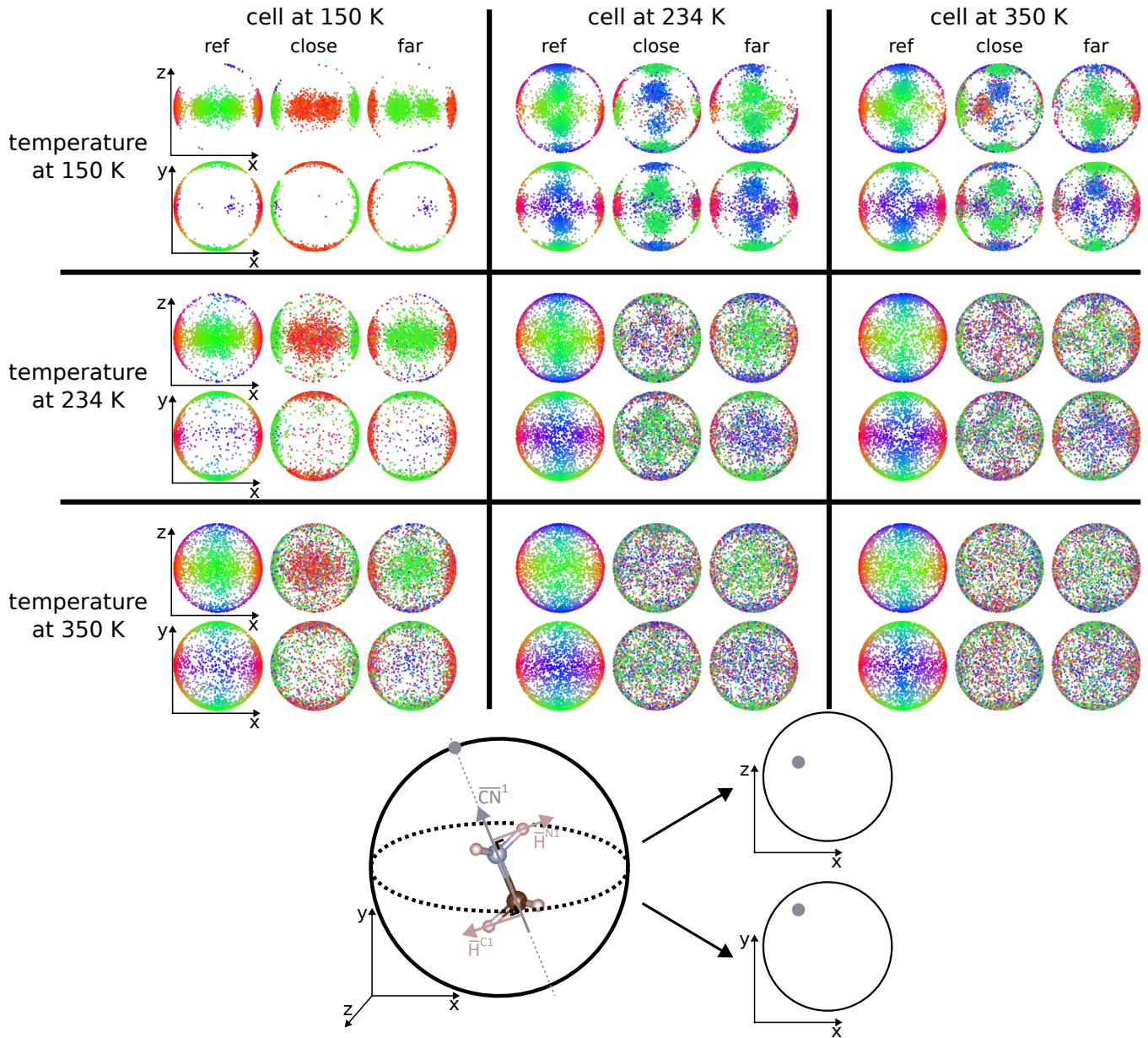


Figure 8: Orientation distributions of three MA molecules in the γ phase of MAPbI_3 during NVT simulations on the MLP PES at the specified temperature and simulation cell. The orientation of each molecule is represented by the unit vector $\vec{\text{CN}}^1$, defined from the carbon to the nitrogen atom. The endpoints of these vectors are projected onto the xz and xy planes, as illustrated at the bottom of the figure. For each simulation, three MA molecules are selected: one is randomly chosen as the reference, and the other two are the nearest and furthest molecules from the reference. The RGB color of each dot is determined by the x , y , and z components of the $\vec{\text{CN}}^1$ vector of the reference MA molecule in the simulation cell.

XC functionals achieve a reasonable root mean square error (RMSE) in the energies, around 2 kJ/mol pfu. However, accurately reproducing the forces proves more challenging. The overall RMSE in the forces is approximately 300 meV/Å, but this error is highly element-dependent: the inorganic atoms typically show much smaller force errors (around 100 meV/Å), while the organic atoms can exhibit errors of up to 1 eV/Å. We attribute these large deviations primarily to internal modes of the organic cations, which are present in all three phases and are thus expected to cancel out when computing free energy differences. Based on its balance between accuracy, computational cost, and precision, the MLP was trained on a dataset computed using DFT with the PBE+D3(BJ) functional.

To calculate the Gibbs free energy, we outline a multistep procedure using TI to correct the harmonic free energies. The harmonic free energy, previously obtained via molecular dynamics simulations as described in our earlier work,^[16] becomes unreliable for materials containing organic molecules due to their rotational degrees of freedom. We introduce an intermediate PES and apply REX to mitigate sampling issues at low temperatures, which arise from the presence of multiple local minima. The dependence of the Helmholtz free energy on the cell parameters is challenging to correct with high accuracy. To reduce this cell dependence, we employ eight different simulation cells for each phase, corresponding to the average cell geometries obtained from NPT simulations at eight different temperatures.

With this TI approach, we find that the δ phases are enthalpically favored, while the γ phase is stabilized by entropy. This explains why it is difficult to stabilize the optically active γ phase at low temperatures.

The ground state energy favors the δ_{Cs} phase over the δ_{FA} phase, which in turn is more stable than the γ phase. In contrast, both the harmonic and configurational free energy contributions reverse this stability order, favoring the γ phase. The predicted transition temperatures for CsPbI₃ and FAPbI₃ are in good agreement with experimental values, while the transition temperature of MAPbI₃ is overestimated. Since the free energy differences vary slowly with temperature, even small enthalpic errors can lead to significant deviations in the predicted transition temperatures. The free energy difference between the δ_{Cs} and γ phases increases by approximately 2.4 kJ/mol per 100 K, whereas the difference between the δ_{FA} and γ phases increases by about 0.9 kJ/mol per 100 K. For smaller supercells, the harmonic and configurational contributions tend to overestimate the stability of the γ phase. As a result, simulations with larger supercells exhibit a slightly lower temperature dependence of the free energy difference, shifting the predicted transition temperatures further away from experimental values.

By comparing the different contributions to the free energy for the three materials, we observe that the ground state energy has the largest influence. The harmonic free energy also varies between the three materials. However, once the configurational free energy is included, the temperature dependence of the total free energy becomes similar across all phases and materials. This observation does not hold for the smallest simulation cell of the γ phase of MAPbI₃. In this case, the orientation of a single organic molecule strongly influences the orientation of neighboring molecules. In contrast, for larger cells and at higher

temperatures, the organic molecules can rotate more freely, resulting in a higher configurational entropy. Furthermore, the ground state energy itself is significantly affected by the size and shape of the simulation cell. Therefore, in order to reliably estimate the transition temperature based on ground state energy calculations, the energy should be computed using the average simulation cell at the estimated transition temperature. Additionally, the organic molecules should exhibit sufficient orientational freedom such that the orientation of one molecule does not strongly constrain the orientations of others.

To the best of our knowledge, this is the first study to compute the Gibbs free energy of both inorganic and organic MHPs with *ab initio* accuracy and minimal approximations. Our findings, including the similar temperature dependence of free energy in CsPbI₃, FAPbI₃, and MAPbI₃, the critical role of ground-state energy, and the influence of molecular orientation freedom, provide valuable insights into phase stability across MHP materials. Furthermore, the presented methodology enables computational screening for MHPs with enhanced phase stability, offering a valuable tool for guiding materials design and potential industrial applications.

CONFLICTS OF INTEREST

There are no conflicts to declare.

DATA AVAILABILITY

The data that support the findings of this study are openly available in Zenodo at <https://doi.org/10.5281/zenodo.18108633>.

ACKNOWLEDGEMENTS

The authors acknowledge financial support from iBOF-21-085 PER-SIST. V.V.S. acknowledges funding from the Research Board of Ghent University (BOF). The computational resources and services used in this work were provided by the VSC (Flemish Supercomputer Center), funded by the Research Foundation-Flanders (FWO) and the Flemish Government-department EWI.

SUPPORTING INFORMATION

The Supporting Information is provided after the references.

REFERENCES

- [1] Jin Young Kim, Jin-Wook Lee, Hyun Suk Jung, Hyunjung Shin, and Nam-Gyu Park. High-efficiency perovskite solar cells. *Chem. Rev.*, 120(15):7867–7918, Aug 2020. ISSN 0009-2665. doi: 10.1021/acs.chemrev.0c00107. URL <https://doi.org/10.1021/acs.chemrev.0c00107>.
- [2] Kai Zhang, Ningning Zhu, Mingming Zhang, Lei Wang, and Jun Xing. Opportunities and challenges in perovskite led commercialization. *J. Mater. Chem. C*, 9:3795–3799, 2021. doi: 10.1039/D1TC00232E. URL <http://dx.doi.org/10.1039/D1TC00232E>.
- [3] He Dong, Chenxin Ran, Weiyin Gao, Mingjie Li, Yingdong Xia, and Wei Huang. Metal halide perovskite for next-generation optoelectronics: progresses and prospects. *eLight*, 3(1):3, Jan 2023. ISSN 2662-8643. doi: 10.1186/s43593-022-00033-z. URL <https://doi.org/10.1186/s43593-022-00033-z>.
- [4] Wanchun Xiang, Shengzhong (Frank) Liu, and Wolfgang Tress. A review on the stability of inorganic metal halide perovskites: challenges and opportunities for stable solar cells. *Energy Environ. Sci.*, 14:2090–2113, 2021. doi: 10.1039/D1EE00157D. URL <http://dx.doi.org/10.1039/D1EE00157D>.

- [5] Constantinos C. Stoumpos, Christos D. Malliakas, and Mercouri G. Kanatzidis. Semiconducting tin and lead iodide perovskites with organic cations: Phase transitions, high mobilities, and near-infrared photoluminescent properties. *Inorg.*, 52(15): 9019–9038, Aug 2013. ISSN 0020-1669. doi: 10.1021/ic401215x. URL <https://doi.org/10.1021/ic401215x>.
- [6] Julian A. Steele, Handong Jin, Iurii Dovgaliuk, Robert F. Berger, Tom Braeckvelt, Haifeng Yuan, Cristina Martin, Eduardo Solano, Kurt Lejaeghere, Sven M. J. Rogge, Charlotte Notebaert, Wouter Vandezande, Kris P. F. Janssen, Bart Goderis, Elke Debroye, Ya-Kun Wang, Yitong Dong, Dongxin Ma, Makhud Saidaminov, Hairen Tan, Zhenghong Lu, Vadim Dyadkin, Dmitry Chernyshov, Veronique Van Speybroeck, Edward H. Sargent, Johan Hofkens, and Maarten B. J. Roeffaers. Thermal nonequilibrium of strained black CsPbI_3 thin films. *Science*, 365(6454):679–684, 2019. doi: 10.1126/science.aax3878. URL <https://www.science.org/doi/abs/10.1126/science.aax3878>.
- [7] Julian A. Steele, Eduardo Solano, Handong Jin, Vittal Prakasam, Tom Braeckvelt, Haifeng Yuan, Zhenni Lin, René de Kloe, Qiong Wang, Sven M. J. Rogge, Veronique Van Speybroeck, Dmitry Chernyshov, Johan Hofkens, and Maarten B. J. Roeffaers. Texture formation in polycrystalline thin films of all-inorganic lead halide perovskite. *Adv. Mater.*, 33(13):2007224, 2021. doi: <https://doi.org/10.1002/adma.202007224>. URL <https://onlinelibrary.wiley.com/doi/abs/10.1002/adma.202007224>.
- [8] Keqiang Chen, Qiaohui Zhong, Wen Chen, Binghua Sang, Yingwei Wang, Tingqiang Yang, Yueli Liu, Yupeng Zhang, and Han Zhang. Short-chain ligand-passivated stable α - CsPbI_3 quantum dot for all-inorganic perovskite solar cells. *Adv. Funct. Mater.*, 29(24):1900991, 2019. doi: <https://doi.org/10.1002/adfm.201900991>. URL <https://onlinelibrary.wiley.com/doi/abs/10.1002/adfm.201900991>.
- [9] Bo Li, Yanan Zhang, Lin Fu, Tong Yu, Shujie Zhou, Luyuan Zhang, and Longwei Yin. Surface passivation engineering strategy to fully-inorganic cubic CsPbI_3 perovskites for high-performance solar cells. *Nat. Commun.*, 9(1):1076, Mar 2018. ISSN 2041-1723. doi: 10.1038/s41467-018-03169-0. URL <https://doi.org/10.1038/s41467-018-03169-0>.
- [10] Faming Li, Yunhe Pei, Fei Xiao, Tixian Zeng, Zhou Yang, Jinjiang Xu, Jie Sun, Bo Peng, and Mingzhen Liu. Tailored dimensionality to regulate the phase stability of inorganic cesium lead iodide perovskites. *Nanoscale*, 10:6318–6322, 2018. doi: 10.1039/C8NR00758F. URL <http://dx.doi.org/10.1039/C8NR00758F>.
- [11] Tianhao Wu, Yanbo Wang, Zhensheng Dai, Danyu Cui, Tao Wang, Xiangyue Meng, Enbing Bi, Xudong Yang, and Liyuan Han. Efficient and stable CsPbI_3 solar cells via regulating lattice distortion with surface organic terminal groups. *Adv. Mater.*, 31(24):1900605, 2019. doi: <https://doi.org/10.1002/adma.201900605>. URL <https://onlinelibrary.wiley.com/doi/abs/10.1002/adma.201900605>.
- [12] Dmitry N. Dirin, Loredana Protesescu, David Trummer, Ilia V. Kochetygov, Sergii Yakunin, Frank Krumeich, Nicholas P. Stadie, and Maksym V. Kovalenko. Harnessing defect-tolerance at the nanoscale: Highly luminescent lead halide perovskite nanocrystals in mesoporous silica matrixes. *Nano Lett.*, 16(9):5866–5874, Sep 2016. ISSN 1530-6984. doi: 10.1021/acs.nanolett.6b02688. URL <https://doi.org/10.1021/acs.nanolett.6b02688>.
- [13] Min Lu, Xiaoyu Zhang, Xue Bai, Hua Wu, Xinyu Shen, Yu Zhang, Wei Zhang, Weitao Zheng, Hongwei Song, William W. Yu, and Andrey L. Rogach. Spontaneous silver doping and surface passivation of CsPbI_3 perovskite active layer enable light-emitting devices with an external quantum efficiency of 11.2%. *ACS Energy Lett.*, 3(7):1571–1577, Jul 2018. doi: 10.1021/acsenerylett.8b00835. URL <https://doi.org/10.1021/acsenerylett.8b00835>.
- [14] Yue-Yu Zhang, Shiyu Chen, Peng Xu, Hongjun Xiang, Xin-Gao Gong, Aron Walsh, and Su-Huai Wei. Intrinsic instability of the hybrid halide perovskite semiconductor $\text{CH}_3\text{NH}_3\text{PbI}_3$. *Chinese Physics Letters*, 35(3):036104, mar 2018. doi: 10.1088/0256-307X/35/3/036104. URL <https://doi.org/10.1088/0256-307X/35/3/036104>.
- [15] Neha Arora, Alessandro Greco, Simone Meloni, Alexander Hinderhofer, Alessandro Mattoni, Ursula Rothlisberger, Jan Hagenlocher, Claudia Caddeo, Shaik M. Zakeeruddin, Frank Schreiber, Michael Graetzel, Richard H. Friend, and M. Ibrahim Dar. Kinetics and energetics of metal halide perovskite conversion reactions at the nanoscale. *Communications Materials*, 3(1):22, Apr 2022. ISSN 2662-4443. doi: 10.1038/s43246-022-00239-1. URL <https://doi.org/10.1038/s43246-022-00239-1>.
- [16] Tom Braeckvelt, Ruben Goeminne, Sander Vandenhaute, Sander Borgmans, Toon Verstraelen, Julian A. Steele, Maarten B. J. Roeffaers, Johan Hofkens, Sven M. J. Rogge, and Veronique Van Speybroeck. Accurately determining the phase transition temperature of CsPbI_3 via random-phase approximation calculations and phase-transferable machine learning potentials. *Chemistry of Materials*, 34(19):8561–8576, Oct 2022. ISSN 0897-4756. doi: 10.1021/acs.chemmater.2c01508. URL <https://doi.org/10.1021/acs.chemmater.2c01508>.
- [17] Venkat Kapil, Edgar Engel, Mariana Rossi, and Michele Ceriotti. Assessment of approximate methods for anharmonic free energies. *Journal of Chemical Theory and Computation*, 15(11):5845–5857, Nov 2019. ISSN 1549-9618. doi: 10.1021/acs.jctc.9b00596. URL <https://doi.org/10.1021/acs.jctc.9b00596>.
- [18] Bingqing Cheng and Michele Ceriotti. Computing the absolute gibbs free energy in atomistic simulations: Applications to defects in solids. *Phys. Rev. B*, 97:054102, Feb 2018. doi: 10.1103/PhysRevB.97.054102. URL <https://link.aps.org/doi/10.1103/PhysRevB.97.054102>.
- [19] Bingqing Cheng, Edgar A. Engel, Jörg Behler, Christoph Dellago, and Michele Ceriotti. Ab initio thermodynamics of liquid and solid water. *Proceedings of the National Academy of Sciences*, 116(4):1110–1115, 2019. doi: 10.1073/pnas.1815117116. URL <https://www.pnas.org/doi/abs/10.1073/pnas.1815117116>.
- [20] S. M. J. Rogge, L. Vanduyfhuys, A. Ghysels, M. Waroquier, T. Verstraelen, G. Maurin, and V. Van Speybroeck. A comparison of barostats for the mechanical characterization of metal-organic frameworks. *Journal of Chemical Theory and Computation*, 11(12):5583–5597, Dec 2015. ISSN 1549-9618. doi: 10.1021/acs.jctc.5b00748. URL <https://doi.org/10.1021/acs.jctc.5b00748>.
- [21] Evert Jan Meijer, Daan Frenkel, Richard A. LeSar, and Anthony J. C. Ladd. Location of melting point at 300 k of nitrogen by monte carlo simulation. *The Journal of Chemical Physics*, 92(12):7570–7575, 1990. doi: 10.1063/1.458193. URL <https://doi.org/10.1063/1.458193>.
- [22] Tomáš Bučko, Monika Gešvandtnerová, and Dario Rocca. Ab initio calculations of free energy of activation at multiple electronic structure levels made affordable: An effective combination of perturbation theory and machine learning. *Journal of Chemical Theory and Computation*, 16(10):6049–6060, Oct 2020. ISSN 1549-9618. doi: 10.1021/acs.jctc.0c00486. URL <https://doi.org/10.1021/acs.jctc.0c00486>.
- [23] Jonas Amsler, Philipp N. Plessow, Felix Studt, and Tomáš Bučko. Anharmonic correction to adsorption free energy from dft-based md using thermodynamic integration. *Journal of Chemical Theory*

- and Computation*, 17(2):1155–1169, 2021. doi: 10.1021/acs.jctc.0c01022. URL <https://doi.org/10.1021/acs.jctc.0c01022>. PMID: 33482059.
- [24] Blazej Grabowski, Yuji Ikeda, Prashanth Srinivasan, Fritz Körmann, Christoph Freysoldt, Andrew Ian Duff, Alexander Shapeev, and Jörg Neugebauer. Ab initio vibrational free energies including anharmonicity for multicomponent alloys. *npj Computational Materials*, 5(1):80, Jul 2019. ISSN 2057-3960. doi: 10.1038/s41524-019-0218-8. URL <https://doi.org/10.1038/s41524-019-0218-8>.
- [25] Daan Frenkel and Anthony J. C. Ladd. New monte carlo method to compute the free energy of arbitrary solids. application to the fcc and hcp phases of hard spheres. *The Journal of Chemical Physics*, 81(7):3188–3193, 1984. doi: 10.1063/1.448024. URL <https://doi.org/10.1063/1.448024>.
- [26] Jeremy Q. Broughton and George H. Gilmer. Molecular dynamics investigation of the crystal–fluid interface. i. bulk properties. *The Journal of Chemical Physics*, 79(10):5095–5104, 1983. doi: 10.1063/1.445633. URL <https://doi.org/10.1063/1.445633>.
- [27] Lunna Li, Tim Totton, and Daan Frenkel. Computational methodology for solubility prediction: Application to the sparingly soluble solutes. *The Journal of Chemical Physics*, 146(21):214110, 2017. doi: 10.1063/1.4983754. URL <https://doi.org/10.1063/1.4983754>.
- [28] Shogo Fukushima, Eisaku Ushijima, Hiroyuki Kumazoe, Akihide Koura, Fuyuki Shimojo, Kohei Shimamura, Masaaki Misawa, Rajiv K. Kalia, Aiichiro Nakano, and Priya Vashishta. Thermodynamic integration by neural network potentials based on first-principles dynamic calculations. *Phys. Rev. B*, 100:214108, Dec 2019. doi: 10.1103/PhysRevB.100.214108. URL <https://link.aps.org/doi/10.1103/PhysRevB.100.214108>.
- [29] Erik Fransson, Julia Wiktor, and Paul Erhart. Phase transitions in inorganic halide perovskites from machine-learned potentials. *The Journal of Physical Chemistry C*, 127(28):13773–13781, Jul 2023. ISSN 1932-7447. doi: 10.1021/acs.jpcc.3c01542. URL <https://doi.org/10.1021/acs.jpcc.3c01542>.
- [30] Simon Batzner, Albert Muehler, Lixin Sun, Mario Geiger, Jonathan P. Mailoa, Mordechai Kornbluth, Nicola Molinari, Tess E. Smidt, and Boris Kozinsky. E(3)-equivariant graph neural networks for data-efficient and accurate interatomic potentials. *Nature Communications*, 13(1):2453, May 2022. ISSN 2041-1723. doi: 10.1038/s41467-022-29939-5. URL <https://doi.org/10.1038/s41467-022-29939-5>.
- [31] Ilyes Batatia, Dávid Péter Kovács, Gregor N. C. Simm, Christoph Ortner, and Gábor Csányi. Mace: Higher order equivariant message passing neural networks for fast and accurate force fields, 2022. URL <https://arxiv.org/abs/2206.07697>.
- [32] Jonathon S. Bechtel, John C. Thomas, and Anton Van der Ven. Finite-temperature simulation of anharmonicity and octahedral tilting transitions in halide perovskites. *Phys. Rev. Mater.*, 3:113605, Nov 2019. doi: 10.1103/PhysRevMaterials.3.113605. URL <https://link.aps.org/doi/10.1103/PhysRevMaterials.3.113605>.
- [33] Aurelien M. A. Leguy, Jarvist Moore Frost, Andrew P. McMahon, Victoria Garcia Sakai, W. Kockelmann, ChunHung Law, Xiaoe Li, Fabrizia Foglia, Aron Walsh, Brian C. O’Regan, Jenny Nelson, João T. Cabral, and Piers R. F. Barnes. The dynamics of methylammonium ions in hybrid organic–inorganic perovskite solar cells. *Nature Communications*, 6(1):7124, May 2015. ISSN 2041-1723. doi: 10.1038/ncomms8124. URL <https://doi.org/10.1038/ncomms8124>.
- [34] Erik Fransson, J. Magnus Rahm, Julia Wiktor, and Paul Erhart. Revealing the free energy landscape of halide perovskites: Metastability and transition characters in cspbbr₃ and mapbi₃. *Chemistry of Materials*, 35(19):8229–8238, Oct 2023. ISSN 0897-4756. doi: 10.1021/acs.chemmater.3c01740. URL <https://doi.org/10.1021/acs.chemmater.3c01740>.
- [35] Sangita Dutta, Erik Fransson, Tobias Hainer, Benjamin M. Galant, Dominik J. Kubicki, Paul Erhart, and Julia Wiktor. Revealing the low-temperature phase of fapbi₃ using a machine-learned potential. *Journal of the American Chemical Society*, Aug 2025. ISSN 0002-7863. doi: 10.1021/jacs.5c05265. URL <https://doi.org/10.1021/jacs.5c05265>.
- [36] Virginia Carnevali, Lorenzo Agosta, Vladislav Slama, Nikolaos Lempesis, Andrea Vezzosi, and Ursula Rothlisberger. Nanoscale size effects in α -fapbi₃ evinced by large-scale ab initio simulations. *Nature Communications*, 16(1):6825, Jul 2025. ISSN 2041-1723. doi: 10.1038/s41467-025-61351-7. URL <https://doi.org/10.1038/s41467-025-61351-7>.
- [37] Yuji Sugita and Yuko Okamoto. Replica-exchange molecular dynamics method for protein folding. *Chemical Physics Letters*, 314(1):141–151, 1999. ISSN 0009-2614. doi: [https://doi.org/10.1016/S0009-2614\(99\)01123-9](https://doi.org/10.1016/S0009-2614(99)01123-9). URL <https://www.sciencedirect.com/science/article/pii/S0009261499011239>.
- [38] David J. Earl and Michael W. Deem. Parallel tempering: Theory, applications, and new perspectives. *Phys. Chem. Chem. Phys.*, 7:3910–3916, 2005. doi: 10.1039/B509983H. URL <http://dx.doi.org/10.1039/B509983H>.
- [39] Ruben Demuyneck, Jelle Wieme, Sven M. J. Rogge, Karen D. Dedecker, Louis Vanduyfhuys, Michel Waroquier, and Veronique Van Speybroeck. Protocol for identifying accurate collective variables in enhanced molecular dynamics simulations for the description of structural transformations in flexible metal–organic frameworks. *Journal of Chemical Theory and Computation*, 14(11):5511–5526, Nov 2018. ISSN 1549-9618. doi: 10.1021/acs.jctc.8b00725. URL <https://doi.org/10.1021/acs.jctc.8b00725>.
- [40] Christèle Beauvais, Xavier Guerrault, François-Xavier Coudert, Anne Boutin, and Alain H. Fuchs. Distribution of sodium cations in faujasite-type zeolite: a canonical parallel tempering simulation study. *The Journal of Physical Chemistry B*, 108(1):399–404, Jan 2004. ISSN 1520-6106. doi: 10.1021/jp036085i. URL <https://doi.org/10.1021/jp036085i>.
- [41] G. Kresse and J. Furthmüller. Efficiency of ab-initio total energy calculations for metals and semiconductors using a plane-wave basis set. *Comput. Mater. Sci.*, 6(1):15–50, 1996.
- [42] G. Kresse and J. Furthmüller. Efficient iterative schemes for ab initio total-energy calculations using a plane-wave basis set. *Phys. Rev. B*, 54:11169–11186, Oct 1996.
- [43] John P. Perdew, Kieron Burke, and Matthias Ernzerhof. Generalized gradient approximation made simple. *Phys. Rev. Lett.*, 77:3865–3868, Oct 1996. doi: 10.1103/PhysRevLett.77.3865. URL <https://link.aps.org/doi/10.1103/PhysRevLett.77.3865>.
- [44] Stefan Grimme, Stephan Ehrlich, and Lars Goerigk. Effect of the damping function in dispersion corrected density functional theory. *J. Comput. Chem.*, 32(7):1456–1465, 2011. doi: <https://doi.org/10.1002/jcc.21759>. URL <https://onlinelibrary.wiley.com/doi/abs/10.1002/jcc.21759>.
- [45] Guo P. Chen, Vamsee K. Voora, Matthew M. Agee, Sree Ganesh Balasubramani, and Filipp Furche. Random-phase approximation methods. *Annu. Rev. Phys. Chem.*, 68(1):421–445, 2017. doi: 10.1146/annurev-physchem-040215-112308. URL <https://doi.org/10.1146/annurev-physchem-040215-112308>.

- [46] Benjamin Ramberger, Tobias Schäfer, and Georg Kresse. Analytic interatomic forces in the random phase approximation. *Phys. Rev. Lett.*, 118:106403, Mar 2017. doi: 10.1103/PhysRevLett.118.106403. URL <https://link.aps.org/doi/10.1103/PhysRevLett.118.106403>.
- [47] Daan Frenkel, Berend Smit, and Mark A. Ratner. Understanding molecular simulation: From algorithms to applications. *Physics Today*, 50(7):66–66, 07 1997. ISSN 0031-9228. doi: 10.1063/1.881812. URL <https://doi.org/10.1063/1.881812>.
- [48] Giovanni Ciccotti, Raymond Kapral, and Eric Vanden-Eijnden. Blue moon sampling, vectorial reaction coordinates, and unbiased constrained dynamics. *ChemPhysChem*, 6(9):1809–1814, 2005. doi: <https://doi.org/10.1002/cphc.200400669>. URL <https://chemistry-europe.onlinelibrary.wiley.com/doi/abs/10.1002/cphc.200400669>.
- [49] Jonas Amsler, Philipp N. Plessow, Felix Studt, and Tomáš Bučko. Anharmonic correction to free energy barriers from dft-based molecular dynamics using constrained thermodynamic integration. *Journal of Chemical Theory and Computation*, 19(9):2455–2468, 2023. doi: 10.1021/acs.jctc.3c00169. URL <https://doi.org/10.1021/acs.jctc.3c00169>. PMID: 37043693.
- [50] Namrata Jaykhedkar, Roman Bystrický, Milan Sýkora, and Tomáš Bučko. Investigating the role of dispersion corrections and anharmonic effects on the phase transition in srzr3: A systematic analysis from aimd free energy calculations. *The Journal of Chemical Physics*, 160(1):014710, 01 2024. ISSN 0021-9606. doi: 10.1063/5.0185319. URL <https://doi.org/10.1063/5.0185319>.
- [51] Laurens D. M. Peters, Johannes C. B. Dietschreit, Jörg Kusmann, and Christian Ochsenfeld. Calculating free energies from the vibrational density of states function: Validation and critical assessment. *J. Chem. Phys.*, 150(19):194111, 2019. doi: 10.1063/1.5079643. URL <https://doi.org/10.1063/1.5079643>.
- [52] Aleks Reinhardt and Bingqing Cheng. Quantum-mechanical exploration of the phase diagram of water. *Nature Communications*, 12(1):588, Jan 2021. ISSN 2041-1723. doi: 10.1038/s41467-020-20821-w. URL <https://doi.org/10.1038/s41467-020-20821-w>.
- [53] Tsuneyasu Okabe, Masaaki Kawata, Yuko Okamoto, and Masuhiro Mikami. Replica-exchange monte carlo method for the isobaric–isothermal ensemble. *Chemical Physics Letters*, 335(5):435–439, 2001. ISSN 0009-2614. doi: [https://doi.org/10.1016/S0009-2614\(01\)00055-0](https://doi.org/10.1016/S0009-2614(01)00055-0). URL <https://www.sciencedirect.com/science/article/pii/S0009261401000550>.
- [54] Venkat Kapil, Edgar Engel, Mariana Rossi, and Michele Ceriotti. Assessment of approximate methods for anharmonic free energies. *Journal of Chemical Theory and Computation*, 15(11):5845–5857, Nov 2019. ISSN 1549-9618. doi: 10.1021/acs.jctc.9b00596. URL <https://doi.org/10.1021/acs.jctc.9b00596>.
- [55] Jürg Hutter, Marcella Iannuzzi, Florian Schiffmann, and Joost VandeVondele. Cp2k: atomistic simulations of condensed matter systems. *Wiley Interdiscip. Rev. Comput. Mol. Sci.*, 4(1):15–25, 2014. doi: <https://doi.org/10.1002/wcms.1159>. URL <https://wires.onlinelibrary.wiley.com/doi/abs/10.1002/wcms.1159>.
- [56] Joost VandeVondele, Matthias Krack, Fawzi Mohamed, Michele Parrinello, Thomas Chassaing, and Jürg Hutter. Quickstep: Fast and accurate density functional calculations using a mixed gaussian and plane waves approach. *Comput. Phys. Commun.*, 167(2):103–128, 2005. ISSN 0010-4655. doi: <https://doi.org/10.1016/j.cpc.2004.12.014>. URL <https://www.sciencedirect.com/science/article/pii/S0010465505000615>.
- [57] Shuichi Nosé. A unified formulation of the constant temperature molecular dynamics methods. *J. Chem. Phys.*, 81(1):511–519, 1984. doi: 10.1063/1.447334. URL <https://doi.org/10.1063/1.447334>.
- [58] Shuichi Nosé. A molecular dynamics method for simulations in the canonical ensemble. *Mol. Phys.*, 52(2):255–268, 1984. doi: 10.1080/00268978400101201. URL <https://doi.org/10.1080/00268978400101201>.
- [59] William G. Hoover. Canonical dynamics: Equilibrium phase-space distributions. *Phys. Rev. A*, 31:1695–1697, Mar 1985. doi: 10.1103/PhysRevA.31.1695. URL <https://link.aps.org/doi/10.1103/PhysRevA.31.1695>.
- [60] Glenn J. Martyna, Douglas J. Tobias, and Michael L. Klein. Constant pressure molecular dynamics algorithms. *J. Chem. Phys.*, 101(5):4177–4189, 1994. doi: 10.1063/1.467468. URL <https://doi.org/10.1063/1.467468>.
- [61] Domantas Kuryla, Fabian Berger, Gábor Csányi, and Angelos Michaelides. How accurate are dft forces? unexpectedly large uncertainties in molecular datasets. *The Journal of Chemical Physics*, 163(22):224313, 12 2025. ISSN 0021-9606. doi: 10.1063/5.0296997. URL <https://doi.org/10.1063/5.0296997>.
- [62] G. Kresse and D. Joubert. From ultrasoft pseudopotentials to the projector augmented-wave method. *Phys. Rev. B*, 59:1758–1775, Jan 1999. doi: 10.1103/PhysRevB.59.1758. URL <https://link.aps.org/doi/10.1103/PhysRevB.59.1758>.
- [63] Sander Vandenhaute, Maarten Cools-Ceuppens, Simon DeKeyser, Toon Verstraelen, and Veronique Van Speybroeck. Machine learning potentials for metal-organic frameworks using an incremental learning approach. *npj Computational Materials*, 9(1):19, Feb 2023. ISSN 2057-3960. doi: 10.1038/s41524-023-00969-x. URL <https://doi.org/10.1038/s41524-023-00969-x>.
- [64] Ask Hjorth Larsen, Jens Jørgen Mortensen, Jakob Blomqvist, Ivano E. Castelli, Rune Christensen, Marcin Dułak, Jesper Friis, Michael N. Groves, Bjørk Hammer, Cory Hargus, Eric D. Hermes, Paul C. Jennings, Peter Bjerre Jensen, James Kermode, John R. Kitchin, Esben Leonhard Kolsbjerg, Joseph Kubal, Kristen Kaasbjerg, Steen Lysgaard, Jón Bergmann Maronsson, Tristan Maxson, Thomas Olsen, Lars Pastewka, Andrew Peterson, Carsten Rostgaard, Jakob Schiøtz, Ole Schütt, Mikkel Strange, Kristian S. Thygesen, Tejs Vegge, Lasse Vilhelmsen, Michael Walter, Zhenhua Zeng, and Karsten W. Jacobsen. The atomic simulation environment—a python library for working with atoms. *Journal of Physics: Condensed Matter*, 29(27):273002, Jun 2017. ISSN 0953-8984. doi: 10.1088/1361-648X/aa680e. URL <https://dx.doi.org/10.1088/1361-648X/aa680e>.
- [65] David Packwood, James Kermode, Letif Mones, Noam Bernstein, John Woolley, Nicholas Gould, Christoph Ortner, and Gábor Csányi. A universal preconditioner for simulating condensed phase materials. *The Journal of Chemical Physics*, 144(16):164109, 04 2016. ISSN 0021-9606. doi: 10.1063/1.4947024. URL <https://doi.org/10.1063/1.4947024>.
- [66] Toon Verstraelen, Louis Vanduyfhuys, Steven Vandenbrande, and Sven Rogge. Yaff, yet another force field. <https://github.com/molmod/yaff>. Accessed: 2024-10-03.
- [67] William G. Hoover, Anthony J. C. Ladd, and Bill Moran. High-strain-rate plastic flow studied via nonequilibrium molecular dynamics. *Phys. Rev. Lett.*, 48:1818–1820, Jun 1982. doi: 10.1103/PhysRevLett.48.1818. URL <https://link.aps.org/doi/10.1103/PhysRevLett.48.1818>.
- [68] D. J. Evans. Computer “experiment” for nonlinear thermodynamics of couette flow. *J. Chem. Phys.*, 78(6):3297–3302, 1983.

- doi: 10.1063/1.445195. URL <https://doi.org/10.1063/1.445195>.
- [69] Haibo Xue, Geert Brocks, and Shuxia Tao. First-principles calculations of defects in metal halide perovskites: A performance comparison of density functionals. *Phys. Rev. Mater.*, 5:125408, Dec 2021. doi: 10.1103/PhysRevMaterials.5.125408. URL <https://link.aps.org/doi/10.1103/PhysRevMaterials.5.125408>.
- [70] Aron J. Cohen, Paula Mori-Sánchez, and Weitao Yang. Challenges for density functional theory. *Chemical Reviews*, 112(1): 289–320, Jan 2012. ISSN 0009-2665. doi: 10.1021/cr200107z. URL <https://doi.org/10.1021/cr200107z>.
- [71] Danny Broberg, Kyle Bystrom, Shivani Srivastava, Diana Dahliah, Benjamin A. D. Williamson, Leigh Weston, David O. Scanlon, Gian-Marco Rignanese, Shyam Dwaraknath, Joel Varley, Kristin A. Persson, Mark Asta, and Geoffroy Hautier. High-throughput calculations of charged point defect properties with semi-local density functional theory—performance benchmarks for materials screening applications. *npj Computational Materials*, 9(1):72, May 2023. ISSN 2057-3960. doi: 10.1038/s41524-023-01015-6. URL <https://doi.org/10.1038/s41524-023-01015-6>.
- [72] Sebastian P. Sitkiewicz, Robert Zaleśny, Eloy Ramos-Cordoba, Josep M. Luis, and Eduard Matito. How reliable are modern density functional approximations to simulate vibrational spectroscopies? *The Journal of Physical Chemistry Letters*, 13(25):5963–5968, 2022. doi: 10.1021/acs.jpcclett.2c01278. URL <https://doi.org/10.1021/acs.jpcclett.2c01278>. PMID: 35735354.
- [73] Huifen Liu, Nengxu Li, Zehua Chen, Shuxia Tao, Chunlei Li, Lang Jiang, Xiuxiu Niu, Qi Chen, Feng Wang, Yu Zhang, Zijian Huang, Tinglu Song, and Huanping Zhou. Reversible phase transition for durable formamidinium-dominated perovskite photovoltaics. *Advanced Materials*, 34(39): 2204458, 2022. doi: <https://doi.org/10.1002/adma.202204458>. URL <https://advanced.onlinelibrary.wiley.com/doi/abs/10.1002/adma.202204458>.
- [74] Subham Dastidar, Christopher J. Hawley, Andrew D. Dillon, Alejandro D. Gutierrez-Perez, Jonathan E. Spanier, and Aaron T. Fafarman. Quantitative phase-change thermodynamics and metastability of perovskite-phase cesium lead iodide. *J. Phys. Chem. Lett.*, 8(6):1278–1282, Mar 2017. doi: 10.1021/acs.jpcclett.7b00134. URL <https://doi.org/10.1021/acs.jpcclett.7b00134>.
- [75] Bin Wang, Novendra Novendra, and Alexandra Navrotsky. Energetics, structures, and phase transitions of cubic and orthorhombic cesium lead iodide (cs₂pb₂i₃) polymorphs. *Journal of the American Chemical Society*, 141(37):14501–14504, 2019. doi: 10.1021/jacs.9b05924. URL <https://doi.org/10.1021/jacs.9b05924>. 31487167.
- [76] Yu An, Juanita Hidalgo, Carlo Andrea Ricardo Perini, Andrés-Felipe Castro-Méndez, Jacob N. Vagott, Kathryn Bairley, Shirong Wang, Xianggao Li, and Juan-Pablo Correa-Baena. Structural stability of formamidinium- and cesium-based halide perovskites. *ACS Energy Lett.*, 6(5):1942–1969, 2021. doi: 10.1021/acsenerylett.1c00354. URL <https://doi.org/10.1021/acsenerylett.1c00354>.
- [77] Qifeng Han, Sang-Hoon Bae, Pengyu Sun, Yao-Tsung Hsieh, Yang (Michael) Yang, You Seung Rim, Hongxiang Zhao, Qi Chen, Wangzhou Shi, Gang Li, and Yang Yang. Single crystal formamidinium lead iodide (fapbi₃): Insight into the structural, optical, and electrical properties. *Adv. Mater.*, 28(11):2253–2258, 2016. doi: <https://doi.org/10.1002/adma.201505002>. URL <https://onlinelibrary.wiley.com/doi/abs/10.1002/adma.201505002>.
- [78] Nam Joong Jeon, Jun Hong Noh, Woon Seok Yang, Young Chan Kim, Seungchan Ryu, Jangwon Seo, and Sang Il Seok. Compositional engineering of perovskite materials for high-performance solar cells. *Nature*, 517(7535):476–480, Jan 2015. ISSN 1476-4687. doi: 10.1038/nature14133. URL <https://doi.org/10.1038/nature14133>.
- [79] Jonathon S. Bechtel and Anton Van der Ven. Octahedral tilting instabilities in inorganic halide perovskites. *Phys. Rev. Mater.*, 2:025401, Feb 2018. doi: 10.1103/PhysRevMaterials.2.025401. URL <https://link.aps.org/doi/10.1103/PhysRevMaterials.2.025401>.
- [80] Carlos Escorihuela-Sayalero, Luis Carlos Pardo, Michela Romanini, Nicolas Obrecht, Sophie Loehlé, Pol Lloveras, Josep-Lluís Tamarit, and Claudio Cazorla. Prediction and understanding of barocaloric effects in orientationally disordered materials from molecular dynamics simulations. *npj Computational Materials*, 10(1):13, Jan 2024. ISSN 2057-3960. doi: 10.1038/s41524-024-01199-5. URL <https://doi.org/10.1038/s41524-024-01199-5>.
- [81] Carlos Escorihuela-Sayalero, Ares Sanuy, Luis Carlos Pardo, and Claudio Cazorla. Orientational disorder and molecular correlations in hybrid organic–inorganic perovskites: From fundamental insights to technological applications. *ACS Applied Materials & Interfaces*, 17(1):1428–1440, Jan 2025. ISSN 1944-8244. doi: 10.1021/acsam.4c12762. URL <https://doi.org/10.1021/acsam.4c12762>.

The effect of the A-site cation on the phase transition temperature of metal halide perovskites

Tom Braeckvelt,[†] ‡Sander Vandenhaute,[†] Sven M. J. Rogge,[†] Johan Hofkens,[‡] and
Veronique Van Speybroeck^{*,†}

[†]*Center for Molecular Modeling (CMM), Ghent University, Technologiepark-Zwijnaarde 46, 9052
Zwijnaarde, Belgium, and*

[‡]*Department of Chemistry, KU Leuven, Celestijnenlaan 200F, Leuven 3001, Belgium*

E-mail: Veronique.VanSpeybroeck@UGent.be

[†]Ghent University
[‡]KU Leuven Chemistry

Table of contents

1	Quantum versus classical description of the nuclei	S-3
2	VASP settings for the benchmark of the exchange correlation functionals	S-5
2.1	Convergence PBE+D3(BJ) forces	S-5
2.2	Convergence RPA+HF forces	S-7
3	Bias potential for organic molecules	S-9
3.1	Formamidinium	S-10
3.2	Methylammonium	S-10
4	Level of theory effect on the ground state energies	S-12
5	Analysis of the free energy contributions	S-15
5.1	Finding the ground state structure and frequencies	S-15
5.2	Going from the harmonic to the intermediate PES	S-17
5.3	Temperature correction to the Helmholtz free energy for the intermediate PES	S-18
5.4	Going from the intermediate to the MLP PES	S-20
5.5	Temperature correction to the Helmholtz free energy for the MLP PES	S-21
5.6	Going from Helmholtz to Gibbs free energy	S-22
5.7	Temperature correction to the Gibbs free energy for the MLP PES	S-23
5.8	Spectra from NVE MD simulations	S-24
6	Parameters of the average cell used to calculate the Helmholtz free energy	S-26
7	Histogram of optimized energies	S-31
8	Supercell effect on the free energy contributions	S-36
9	Orientation of the organic molecules	S-41

1 Quantum versus classical description of the nuclei

Within the harmonic approximation, we can calculate the correction to the classical free energy, $F_{H, \text{clas}}$, for each mode to obtain the quantum mechanical free energy, $F_{H, \text{qm}}$:¹

$$\Delta F_H(\nu, T) = F_{H, \text{qm}}(\nu, T) - F_{H, \text{clas}}(\nu, T) = k_B T \ln \left[\frac{1 - \exp\left(-\frac{h\nu}{k_B T}\right)}{\frac{h\nu}{k_B T} \exp\left(\frac{-h\nu}{2k_B T}\right)} \right], \quad (\text{S1.1})$$

h is the Planck constant, k_B is the Boltzmann constant, T is temperature, and ν is the frequency of a mode. For a harmonic potential energy surface (PES) the difference between the classical and quantum vibrational free energy becomes negligible at higher temperatures or lower frequencies, as shown on the left side of Fig. S1.

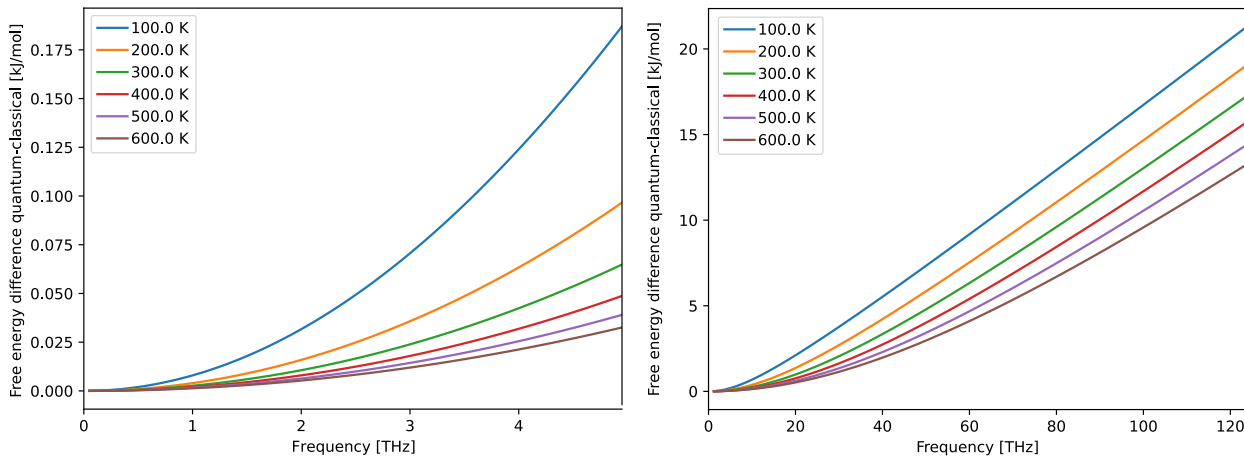


Figure S1: Vibrational free energy difference per mode between a classical and quantum description of the nuclei as a function of the frequency and temperature. The left figure provides a zoomed-in picture of the right figure, to indicate that the quantum free energy difference is approximately the same as the classical free energy for low frequencies and high temperatures.

Heavy nuclei lead to low frequencies and therefore a classical description is sufficient. For the organic molecules a quantum description is necessary. However, the terms in the thermodynamic integration (TI) procedure discussed in Sec. 2 of the main text, assume a classical description of the nuclei. As explained by Kapil and coworkers, it is possible to perform a thermodynamic integration correction to go from the classical to the quantum free energy by applying path integral MD calculations.² This is outside the scope of the current paper.

If we sum (or integrate) over all frequencies and subtract the free energy correction for the δ

phases with the correction of the γ phase, we find the temperature-dependent correction for the free energy differences, the results for CsPbI₃, FAPbI₃, and MAPbI₃ are reported in Tab. S1.

Table S1: Correction to Helmholtz free energy which is the difference between the quantum mechanical free energy and the classical free energy. The correction is obtained via the harmonic approximation, see Eq. S1.1. The differences between the δ phases and the γ phase are reported for the three investigated materials in kJ/mol per formula unit (pfu). For each material three different unit cells are investigated, namely the average unit cell during a NPT MD simulation at 0.1 MPa and at 234, 350, or 501 K.

$F_{H,qm} - F_{H,clas}$ pfu [kJ/mol]	$\delta_{Cs} - \gamma$			$\delta_{FA} - \gamma$		
	$h(T=234\text{ K})$	$h(T=350\text{ K})$	$h(T=501\text{ K})$	$h(T=234\text{ K})$	$h(T=350\text{ K})$	$h(T=501\text{ K})$
CsPbI ₃	0.02	0.02	0.02	0.01	0.02	0.02
FAPbI ₃	-0.54	-0.62	-0.64	0.20	-0.31	-0.27
MAPbI ₃	-0.29	-0.35	-0.40	0.22	0.18	0.06

Because CsPbI₃ only has heavy nuclei, the frequencies are low, and the correction is small. This correction is larger for FAPbI₃, and MAPbI₃ due to the organic molecules. However, the correction remains small because the high-frequency modes are similar for all three phases.

2 VASP settings for the benchmark of the exchange correlation functionals

To benchmark the energies, the same settings as explained in our previous work were used.³ Only for the RPA+HF calculations, the precision setting of the fast Fourier transform grids used to calculate the RPA correlation was increased to "Normal", and the kpoint grids were slightly reduced to $3 \times 3 \times 2$, $6 \times 3 \times 1$, and $3 \times 2 \times 3$ grids for the γ , δ_{Cs} , and δ_{FA} phases, respectively. Because forces are derivatives of the energy, the convergence could be more problematic. Therefore, convergence tests for the forces were performed, see the next subsections. The same settings as for the energy calculations were used for the force calculations. Only the RPA+HF settings were slightly changed. The cut-off energy for the RPA+HF calculations increased to 600 eV, the precision setting of the fast Fourier transform grids was increased to "Accurate", and the kpoint grids were decreased to $2 \times 2 \times 2$, $4 \times 2 \times 4$, and $2 \times 2 \times 2$ grids for the γ , δ_{Cs} , and δ_{FA} phases, respectively.

2.1 Convergence PBE+D3(BJ) forces

The convergence of the cut-off energy was determined for a random structure in the γ phase containing 4 formula units. The results are depicted in Fig. S2 and Tab. S2. The forces do not change significantly when increasing the cut-off energy beyond 400 eV for CsPbI₃. For FAPbI₃ the forces converge more slowly and a cut-off energy of 500 eV is necessary. Using a kpoint grid with only 4 kpoints leads to a huge error in the forces of lead and iodine. A kpoint grid of $3 \times 3 \times 2$ is sufficient to get accurate forces. Setting LREAL to Auto also introduces an error, while the other settings have an insignificant effect.

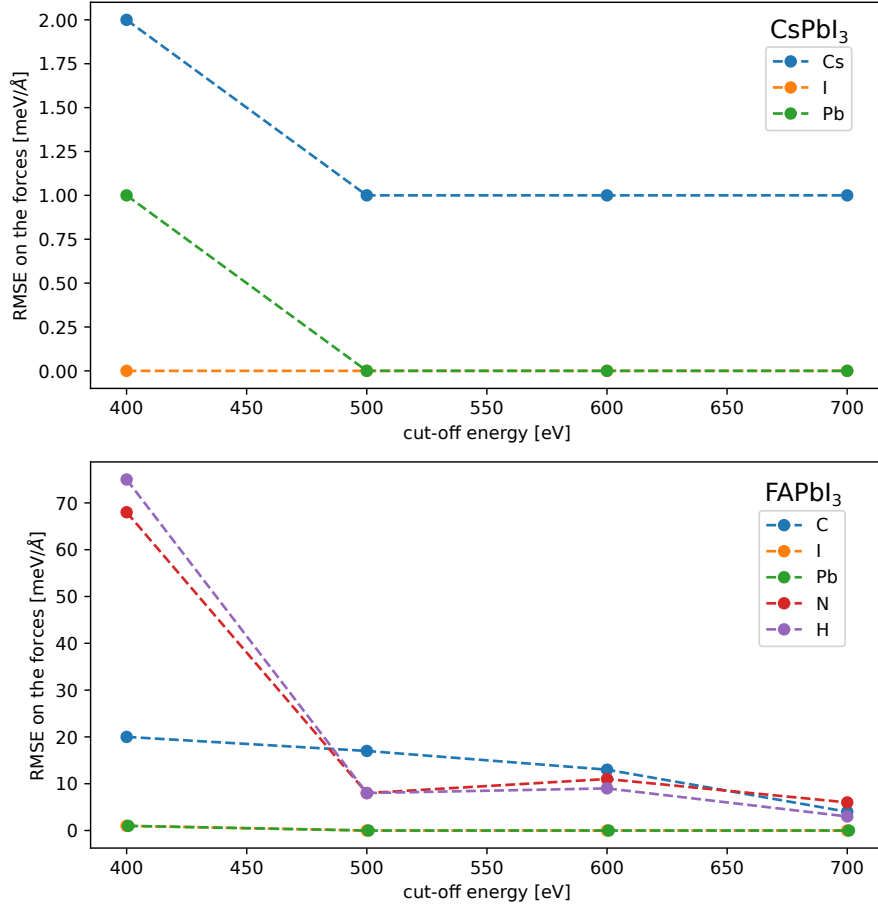


Figure S2: The root mean square error on the PBE+D3(BJ) forces for CsPb₃ and FAPbI₃ partitioned per element. A random structure of the γ phase was used containing 4 formula units. The error was determined with respect to the forces obtained with a cut-off energy of 800 eV.

Table S2: Overview of the effect of the VASP settings on the PBE+D3(BJ) forces for CsPb₃ and FAPbI₃ partitioned per element. The first column indicates which setting is changed with respect to the reference settings (*i.e.*, kpoints = $4 \times 4 \times 3$, PREC = Accurate, ADDGRID = False, LREAL = False, and EDIFF = 10^{-5}) while all other settings are kept at their reference value.

RMSE forces [meV/Å]	CsPbI ₃			FAPbI ₃				
	Cs	Pb	I	H	C	N	Pb	I
kpoints = $2 \times 2 \times 1$	12	150	175	8	12	11	138	135
kpoints = $3 \times 3 \times 2$	1	10	11	0	1	1	7	7
kpoints = $5 \times 5 \times 4$	0	1	1	0	0	0	1	1
PREC = Normal	2	1	0	0	0	1	1	0
ADDGRID = .TRUE.	0	0	0	0	0	0	0	0
LREAL = Auto	6	5	20	2	2	2	5	17
EDIFF = 10^{-8}	1	1	1	0	1	1	0	0

2.2 Convergence RPA+HF forces

The convergence of the cut-off energy was determined for a random structure in the γ phase containing 4 formula units. The results are depicted in Fig. S3 and Tab. S3. The root mean square error (RMSE) on the RPA+HF forces is significantly higher than for PBE+D3(BJ) at the same cut-off energy. The RMSE on the forces goes below $50 \text{ meV}/\text{\AA}$ for all elements only at 600 eV. The forces clearly decrease with increasing cut-off energy, only the error for Cs shows an oscillating behavior around a RMSE of $50 \text{ meV}/\text{\AA}$. The precision setting of the fast Fourier transform grids has a major effect, definitely the grid used to calculate the RPA correlation (PRECFOCK) has to be set to Normal. The kpoint grids can be reduced to $2 \times 2 \times 2$ without significantly changing the forces. Also, the number of frequency points (NOMEGA) has a minor effect.

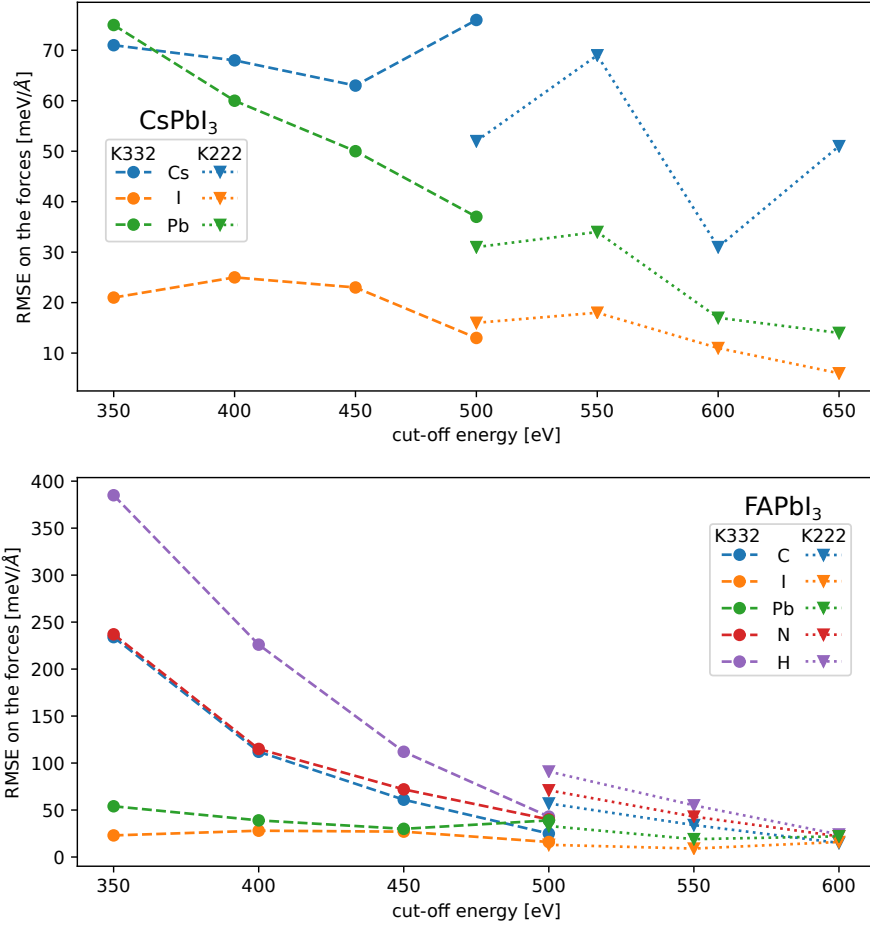


Figure S3: The root mean square error on the RPA+HF forces for CsPbI_3 and FAPbI_3 partitioned per element. A random structure of the γ phase was used containing 4 formula units. The error was determined with respect to the forces obtained with a cut-off energy of 550 eV for a $3 \times 3 \times 2$ kpoint grid. For the calculations with a $2 \times 2 \times 2$ kpoint grid, the reference forces were calculated with 700, and 650 eV as cut-off energy for CsPbI_3 , and FAPbI_3 , respectively.

Table S3: Overview of the effect of the VASP settings on the RPA+HF forces for CsPbI_3 and FAPbI_3 partitioned per element. The first column indicates which setting is changed with respect to the reference settings (*i.e.*, kpoints = $3 \times 3 \times 2$, PRECFOCK = Normal, PREC = Accurate, and NOMEGA = 8) while all other settings are kept at their reference value.

RMSE forces [meV/Å]	CsPbI ₃			FAPbI ₃				
	Cs	Pb	I	H	C	N	Pb	I
kpoints = $2 \times 2 \times 2$	1	5	5	2	1	2	7	7
PRECFOCK = Fast	115	104	132	590	251	854	242	97
PRECFOCK = Accurate	24	21	48	23	7	27	36	22
PREC = Normal	36	24	19	0	2	4	0	0
NOMEGA = 6	3	2	4	2	3	3	3	2
NOMEGA = 12	0	0	0	0	1	1	0	0

3 Bias potential for organic molecules

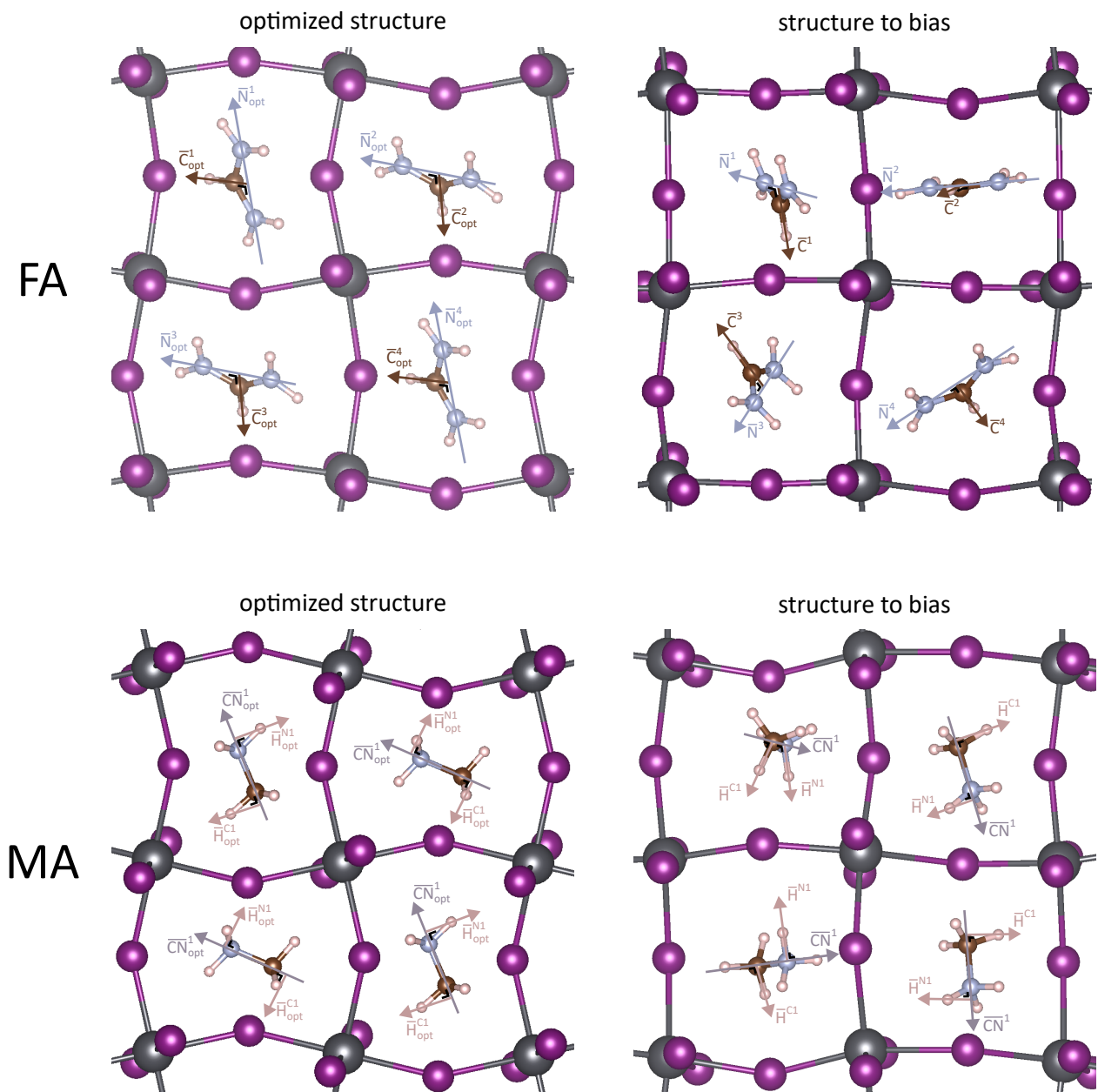


Figure S4: Visual representation of the vectors to define the orientation of the organic FA or MA molecules in the optimized structure and the structure for which the bias will be applied.

W

For the Hessian PES, the organic molecules have a specific orientation. To fix this orientation for the machine learning potential (MLP) PES, we add a bias based on the orientation of the organic molecules with respect to the orientation of the organic molecule in the optimized

structure. The bias is determined for each organic molecule separately. The total bias is the sum of all those biases. For each molecule we define two (for FA) or three (for MA) vectors based on the atomic positions, see Fig. S4. The dot product between the normalized vectors of the optimized structure and the structure for which the bias will be applied, is used as a metric to define the change in orientation. Afterward, a sigmoid function is applied to this dot product. Finally, a harmonic bias is applied when the value of the dot product is lower than 0.95. The exact mathematical values of the bias are provided in the next subsections.

3.1 Formamidinium

$$CV_{\text{N}}^i = \frac{1}{1 + \exp \left[5 \left(\frac{\vec{N}_{\text{opt}}^i \cdot \vec{N}^i}{|\vec{N}_{\text{opt}}^i| |\vec{N}^i|} - 0.95 \right) \right]} \quad (\text{S3.1})$$

$$CV_{\text{C}}^i = \frac{1}{1 + \exp \left[5 \left(\frac{\vec{C}_{\text{opt}}^i \cdot \vec{C}^i}{|\vec{C}_{\text{opt}}^i| |\vec{C}^i|} - 0.95 \right) \right]} \quad (\text{S3.2})$$

$$b_{\text{N}}^i = \begin{cases} 800 (CV_{\text{N}}^i)^2 \text{ [kJ/mol]} & \text{if } CV_{\text{N}}^i < 0.95, \\ 0 & \text{if } CV_{\text{N}}^i \geq 0.95. \end{cases} \quad (\text{S3.3})$$

$$b_{\text{C}}^i = \begin{cases} 200 (CV_{\text{C}}^i)^2 \text{ [kJ/mol]} & \text{if } CV_{\text{C}}^i < 0.95, \\ 0 & \text{if } CV_{\text{C}}^i \geq 0.95. \end{cases} \quad (\text{S3.4})$$

The total bias is equal to the sum of all biases, *i.e.* $\text{bias} = \sum_i^{\text{\#f.u.}} (b_{\text{N}}^i + b_{\text{C}}^i)$

3.2 Methylammonium

$$CV_{\text{CN}}^i = \frac{1}{1 + \exp \left[5 \left(\frac{\vec{CN}_{\text{opt}}^i \cdot \vec{CN}^i}{|\vec{CN}_{\text{opt}}^i| |\vec{CN}^i|} - 0.95 \right) \right]} \quad (\text{S3.5})$$

$$CV_{\text{H}}^i = \frac{1}{1 + \exp \left[5 \left(0.5 \frac{\vec{H}_{\text{opt}}^{\text{Ni}} \cdot \vec{H}^{\text{Ni}}}{|\vec{H}_{\text{opt}}^{\text{Ni}}| |\vec{H}^{\text{Ni}}|} + 0.5 \frac{\vec{H}_{\text{opt}}^{\text{Ci}} \cdot \vec{H}^{\text{Ci}}}{|\vec{H}_{\text{opt}}^{\text{Ci}}| |\vec{H}^{\text{Ci}}|} - 0.95 \right) \right]} \quad (\text{S3.6})$$

$$b_{\text{N}}^i = \begin{cases} 800 (CV_{\text{CN}}^i)^2 \text{ [kJ/mol]} & \text{if } CV_{\text{CN}}^i < 0.95, \\ 0 & \text{if } CV_{\text{CN}}^i \geq 0.95. \end{cases} \quad (\text{S3.7})$$

$$b_{\text{H}}^i = \begin{cases} 200 (CV_{\text{H}}^i)^2 \text{ [kJ/mol]} & \text{if } CV_{\text{H}}^i < 0.95, \\ 0 & \text{if } CV_{\text{H}}^i \geq 0.95. \end{cases} \quad (\text{S3.8})$$

The total bias is equal to the sum of all biases, *i.e.* $\text{bias} = \sum_i^{\text{\#f.u.}} (b_{\text{CN}}^i + b_{\text{H}}^i)$

4 Level of theory effect on the ground state energies

In our previous work,³ we benchmarked exchange-correlation (XC) functionals on optimized structures containing four formula units of CsPbI₃, also optimizing the cell degrees of freedom. Here, we extend this benchmark to FAPbI₃ and MAPbI₃, with results shown in Fig. S5. As discussed in Sec. 7, the rotational freedom of organic molecules introduces numerous local minima. For each phase and material, we optimized ten structures generated from NPT MD simulations at 600 K and 0.1 MPa, all of which relaxed into distinct configurations.

We find that energy differences between optimized structures of the same phase are largely consistent across most XC functionals and dispersion methods. However, the choice of XC functional and dispersion method significantly impacts energy differences between phases, with PBE+D2 and vdW-DF2 standing out as clear outliers. Using the lowest RPA+HF energy for each phase, we determine the ground-state energy (GSE) differences. For FAPbI₃, the GSE difference is 7.22 kJ/mol pfu between the δ_{Cs} and γ phases and 5.26 kJ/mol pfu between the δ_{FA} and γ phases. For MAPbI₃, the corresponding GSE differences are 4.82 kJ/mol pfu and 2.96 kJ/mol pfu, respectively.

It is important to note that this simple optimization procedure probably did not identify the lowest-energy structure for each phase. Fig. S6 presents the results of RPA+HF calculations on MLP-optimized structures. The optimized structures containing eight formula units, without optimizing the cell degrees of freedom, were required for the TI methodology, and the full cell optimized structures were obtained similarly. Specifically, 4000 structures were generated via NVT (NPT) MD simulations at 150 K (and 0.1 MPa). To escape local minima, these MD simulations were coupled via replica exchange (REX) with 31 simulations at higher temperatures, reaching a maximum of 600 K. The structure predicted by the MLP to have the lowest energy was selected as the ground-state structure.

Fig. S6 shows that the MLP reproduces PBE+D3(BJ) energies within a margin of 1 kJ/mol pfu. Furthermore, the PBE+D3(BJ) energies are in good agreement with the RPA+HF results, with GSE differences between phases deviating by at most 2 kJ/mol pfu. Finally, comparing the RPA+HF results for the fully optimized structures in Fig. S6 with the RPA+HF energy differences in Fig. S5, we find small discrepancies, up to 2 kJ/mol pfu. This may be due to supercell effects, though

it is more likely a result of the more comprehensive ground state structure search performed for the TI approach.

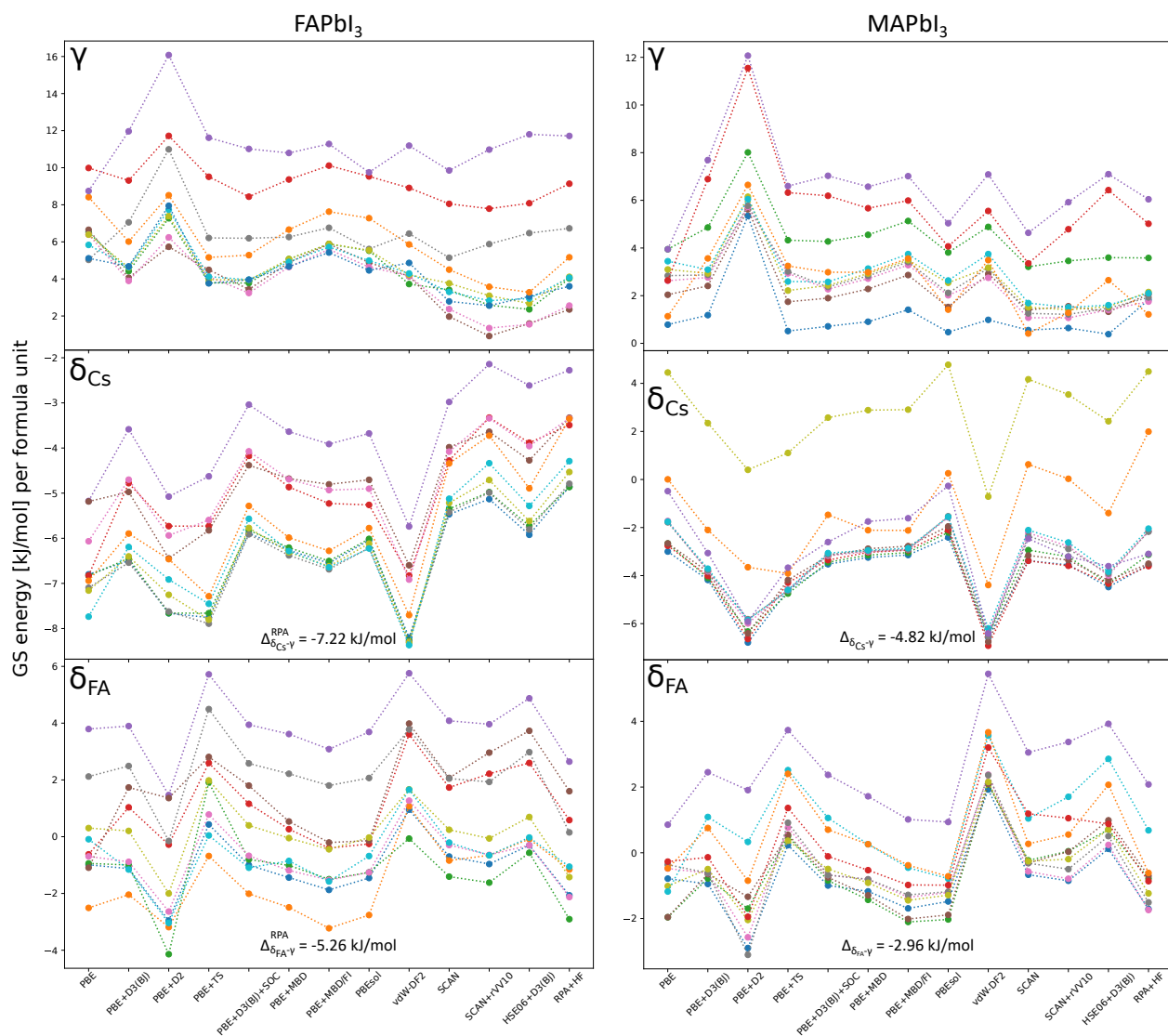


Figure S5: Energy differences between ten NPT optimized structures of the γ , δ_{Cs} , and δ_{FA} phases for FAPbI_3 and MAPbI_3 , calculated using various methods. The simulations were performed using cells containing four formula units, with structure optimization carried out via density functional theory (DFT) employing the PBE+D3(BJ) exchange-correlation functional.

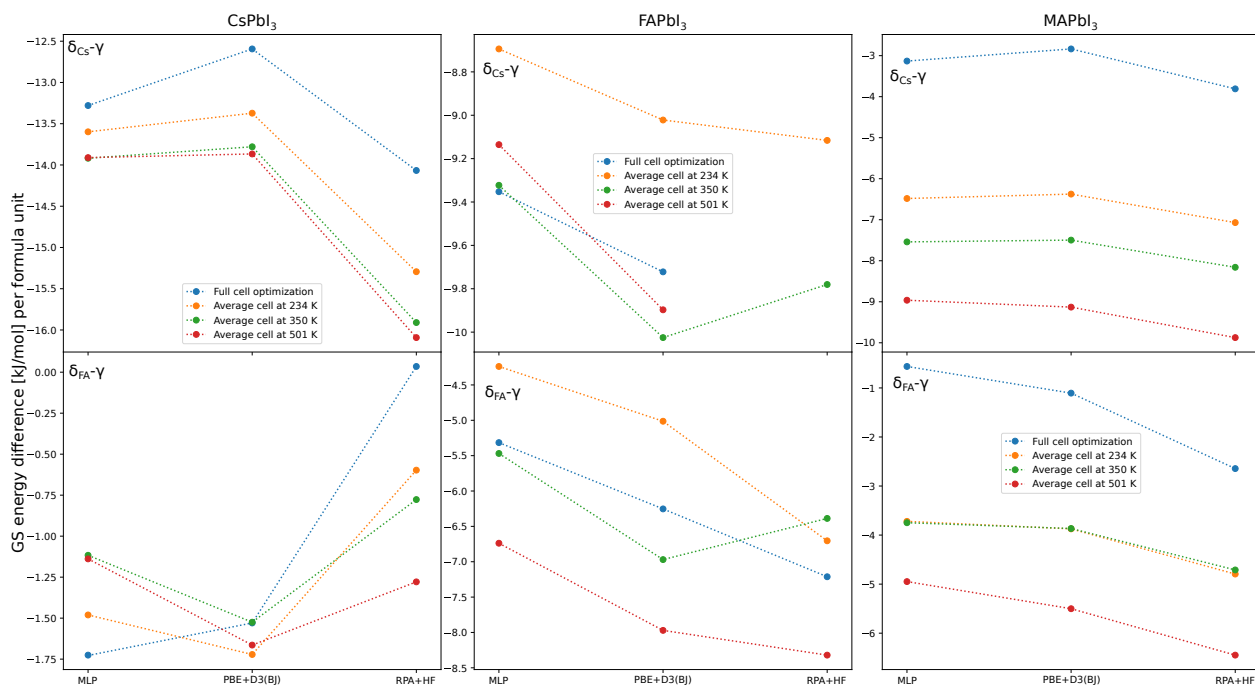


Figure S6: GSE of the δ phases relative to the γ phase for CsPbI₃, FAPbI₃, and MAPbI₃, calculated using MLP, DFT with the PBE+D3(BJ) functional, and RPA+HF. For each phase, structures were optimized using the MLP while keeping the simulation cell containing eight formula units fixed at the average cell dimensions from NPT simulations at 234 K, 350 K, or 501 K. Additionally, a full cell optimization was performed.

5 Analysis of the free energy contributions

The complete TI approach requires multiple MD simulations for each structure. The full TI approach can be split into seven contributions for which six contributions require a fixed simulation cell. Each contribution can be analyzed separately. In this section, we will analyze each contribution for the γ phase of FAPbI₃ using the average cell at 150 K and 0.1 MPa containing eight formula units. The data and plots for all other simulations can be found at <https://doi.org/10.5281/zenodo.18108633>.

5.1 Finding the ground state structure and frequencies

The first step is to find the ground state structure and calculate its frequencies to find the harmonic Helmholtz free energy. While it is impossible to prove that this is the lowest energy structure, the distribution of the 4000 optimized structures does provide some insights. If there are many bins (the bin size is set to 0.2 kJ/mol pfu) present in the plot, many nonequivalent local minima are present in the sampled phase space during the 150 K MD simulations. The more nonequivalent local minima, the less likely that the global minima can be found. The number of times the lowest observed minimum is found, indicates how likely it is to find it. If it is frequently found, then we could have performed fewer optimizations. If not, then the number of optimizations is definitely justified and more optimizations can be considered to affirm that this is the lowest energy structure.

Fig. S7 shows the histogram of the energies of all 4000 optimized structures for the γ phase of FAPbI₃, with a simulation cell set to the average cell at 150 K. There are a lot of different optimized energies, indicating that there are a lot of nonequivalent local minima. The lowest energy was found a few times, which indicates that 4000 optimizations is definitely justified and might be enough. Moreover, the TI approach is in principle correct for a harmonic PES around random local minima. With the downside that the TI corrections might be more difficult to converge. See also Sec. 7, which discusses the histograms for all materials, phases, and simulation cells.

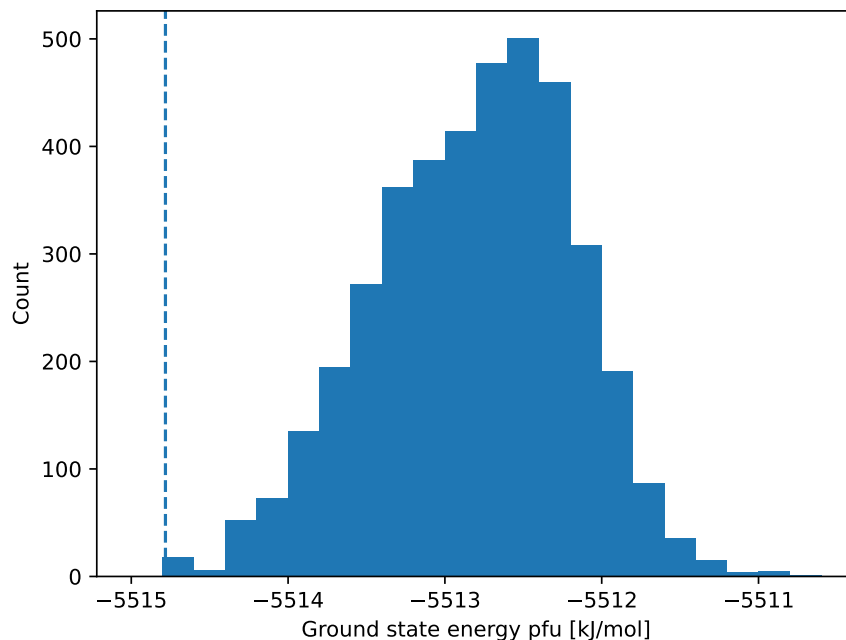


Figure S7: Histogram of the energies of all 4000 optimized structures for the γ phase of FAPbI₃, with a simulation cell set to the average cell at 150 K. The dotted line indicates the lowest optimized energy.

We construct a harmonic PES around the lowest energy minima and calculate the harmonic free energy via its frequencies. Therefore, the Hessian matrix of the lowest energy structure is determined via finite displacements of 53 fm. If the mass-weighted Hessian has negative eigenvalues (besides the 3 translation modes that have eigenvalues close to zero), then a short MD simulation of 500 steps at 100 K are performed, using the lowest energy structure as the initial structure. The last structure of this MD simulation is then reoptimized and its mass-weighted Hessian is determined. If this matrix still has significant negative eigenvalues, the same MD simulation is performed starting from the last structure of the previous MD simulation. This procedure is followed until the mass-weighted Hessian no longer contains significant negative eigenvalues. These eigenvalues are the frequencies from which the harmonic free energy can be determined. The phonon spectra of the γ phase of FAPbI₃, with a simulation cell set to the average cell at 150 K is visualized in Fig. S8.

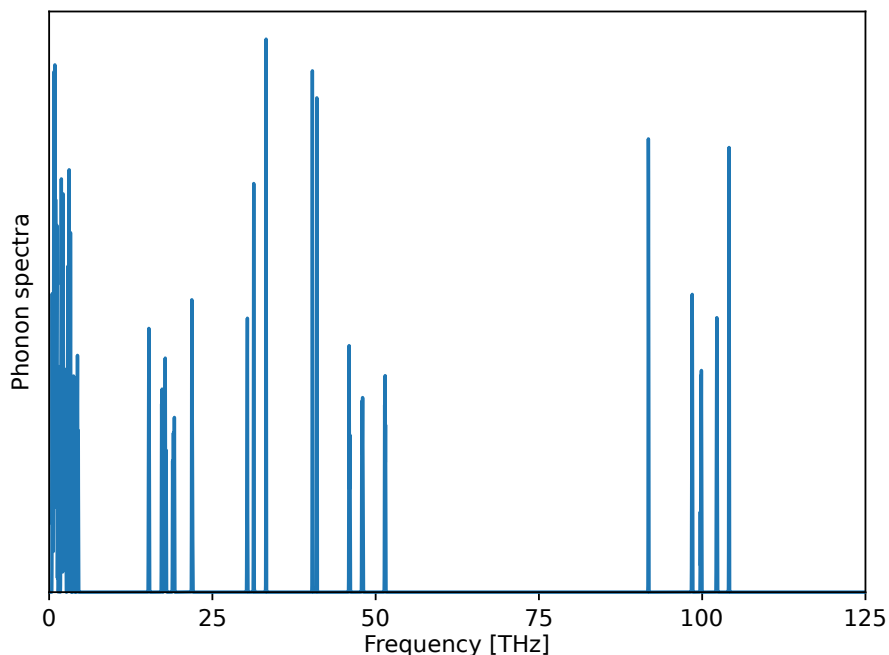


Figure S8: Phonon spectra for the γ phase of FAPbI₃, with a simulation cell set to the average cell at 150 K. Gaussian smearing of 0.02 THz is added to the eigenvalues of the mass-weighted Hessian of the lowest energy structure to construct this spectrum.

5.2 Going from the harmonic to the intermediate PES

To calculate the free energy difference between two PES, a λ -TI contribution is determined. This contribution is calculated via the ensemble average of the energy difference between the two PES, which has to be determined for multiple ensembles that lie along a λ -path that gradually changes one PES into the other, *i.e.*, ensemble average for $U(\lambda) = U_{\text{begin}} + \lambda (U_{\text{end}} - U_{\text{begin}})$. To investigate how the ensemble average changes along the λ -path, we plot the ensemble average and the standard error of the energy difference between the intermediate and harmonic PES as a function of λ for the γ phase of FAPbI₃, with a simulation cell set to the average cell at 150 K. The curve is smooth, monotonically decreasing, and the error bars are too small to be visible. These are signs that the free energy contribution has converged.

The curve shows non-linear behavior at the edges. Therefore, we took more λ points near $\lambda = 0$ and $\lambda = 1$, see Sec. 3.3 of the manuscript. This plot also indicates that along the λ -path different phase spaces are sampled justifying the use of thermodynamic integration over free energy perturbation.⁴

When sampling in the harmonic PES, the intermediate PES is higher in energy, indicating

that the harmonic PES samples unlikely phase spaces of the MLP PES. A possible explanation could be that the translation modes of the FA molecule are relatively free to move leading to short distances between the organic atoms and the iodine atoms. The harmonic PES definitely sampled unrealistic structures, because the initial MLP trained on *ab initio* MD structures generated at 800 K failed to accurately predict some Hessian MD structures generated at 150 K. Therefore, extra Hessian structures got added to the *ab initio* data set, see Sec. 3.2.

On the contrary, when sampling the intermediate PES, the harmonic PES is higher in energy. This is probably the results of nearby local minima that are (partially) sampled for which the harmonic PES predicts a high energy. As shown in Sec. 5.4, for the MLP PES this effect is even more pronounced, because a lot more minima become accessible leading to a significantly negative free energy contribution.

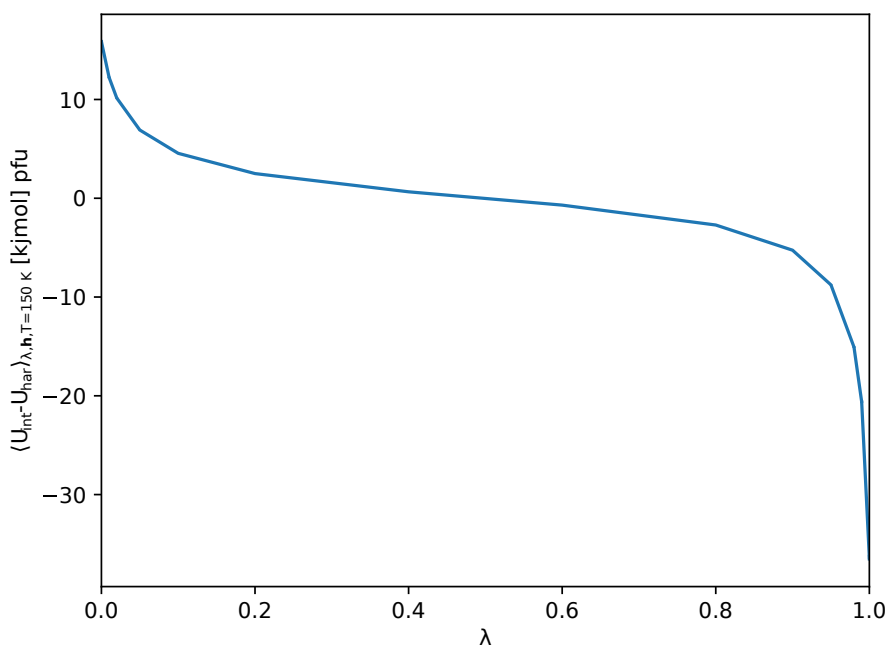


Figure S9: Ensemble average at 150 K of the energy difference between the intermediate PES and harmonic PES as a function of the interpolation parameter λ for the γ phase of FAPbI_3 , with a simulation cell set to the average cell at 150 K.

5.3 Temperature correction to the Helmholtz free energy for the intermediate PES

For the temperature correction to the Helmholtz free energy we need to calculate the ensemble average of the energy at different temperatures. If we plot this ensemble average as a function of temperature we would observe an approximately linear relationship, similar to the ensemble

average of the harmonic PES, namely $\langle U \rangle_{\text{harm},T} = E_{\text{GS}} + (3N - 3) \frac{k_{\text{B}}T}{2}$. Therefore, we investigate the anharmonic ensemble average of the energy:⁵

$$\langle U_{\text{anharm}} \rangle_{\text{int},T} = \langle U \rangle_{\text{int},T} - \langle U \rangle_{\text{harm},T}. \quad (\text{S5.1})$$

As shown by Cheng and Ceriotti,⁵ the Helmholtz free energy can then be determined as follows:

$$\frac{F_{\text{int}}(T_1)}{k_{\text{B}}T_1} = \frac{E_{\text{GS}}}{k_{\text{B}}T_1} + \frac{F_{\text{int}}(T_0) - E_{\text{GS}}}{k_{\text{B}}T_0} - (3N - 3) \ln \frac{T_1}{T_0} - \int_{T_0}^{T_1} \frac{\langle U_{\text{anharm}} \rangle_{\text{int},T}}{k_{\text{B}}T^2} dT \quad (\text{S5.2})$$

Because the third term is the same for each phase, the free energy differences between the phases will have a linear relationship with temperature if $\langle U_{\text{anharm}} \rangle_{\text{int},T} = 0$. This is also the case for the harmonic approximation, with the difference that $F_{\text{int}}(T_0)$ can already include anharmonic corrections calculated in Sec. 5.2. A λ -TI correction calculated at 150 K will be four times more important at 600 K.

The $\langle U_{\text{anharm}} \rangle_{\text{int},T}$ can be interpreted as an added correction on top of the λ -TI correction. This value impacts the slope of the Helmholtz free energy differences as a function of temperature, which is at T_0 equal to $\frac{\Delta F_{\text{int}}(T_0) - \Delta E_{\text{GS}}}{k_{\text{B}}T_0}$. Therefore, when $\langle U_{\text{anharm}} \rangle_T$ is much larger for one phase compared to another, then the free energy difference will have a significant curvature at temperature T .

The results for the γ phase of FAPbI₃, with a simulation cell set to the average cell at 150 K is shown in Fig. S10. The ensemble average of the anharmonic energy for the intermediate PES is small. This means that the anharmonicity of the intermediate PES (if present) was already captured at 150 K via λ -TI, see Sec. 5.2.

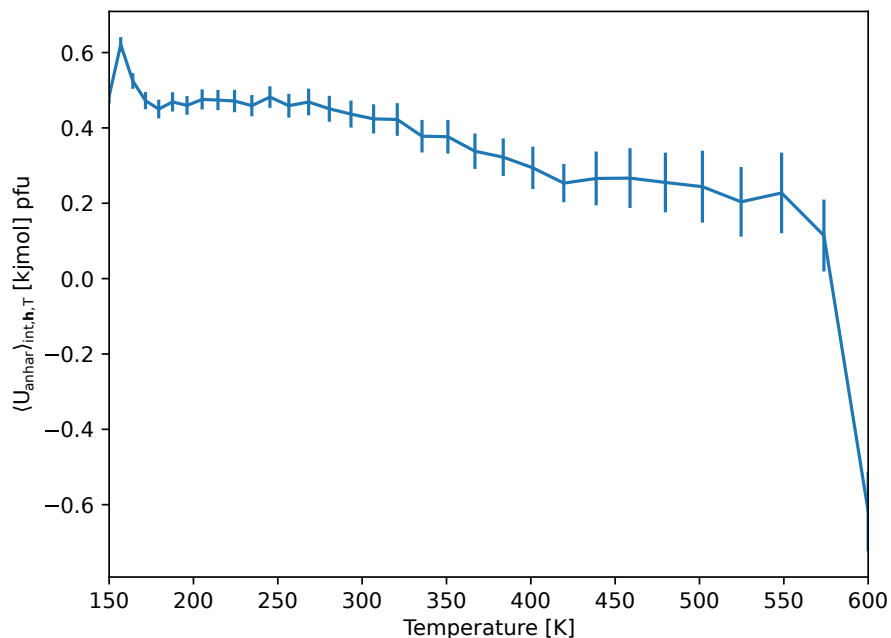


Figure S10: Ensemble average of the anharmonic energy of the intermediate PES as a function of the temperature for the γ phase of FAPbI₃, with a simulation cell set to the average cell at 150 K.

5.4 Going from the intermediate to the MLP PES

For the organic molecules the intermediate PES is the MLP with a positive bias, so the ensemble average of the energy difference is always negative. When λ approaches 1, the bias loses its effect and the other minima become accessible leading to a larger energy difference between the intermediate and MLP PES. Fig. S11 plots the ensemble average of the energy difference between the MLP and intermediate PES as a function of λ . Due to multiple local minima, the correction is rather large. Therefore, it is important to include enough λ values near $\lambda = 1$, and to perform multiple long MD simulations. The small error bars indicate that the ensemble averages are converged.

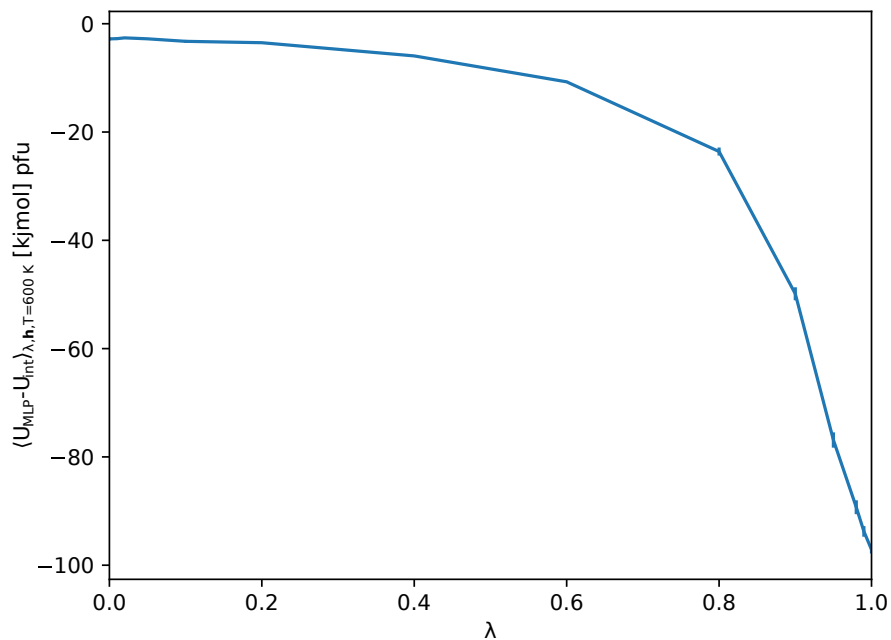


Figure S11: Ensemble average at 600 K of the energy difference between the MLP PES and intermediate PES as a function of the interpolation parameter λ for the γ phase of FAPbI₃ with a simulation cell set to the average cell at 150 K.

5.5 Temperature correction to the Helmholtz free energy for the MLP PES

The same analysis as in Sec. 5.3 is performed for the MLP PES, the results are plotted in Fig. S12. The anharmonic energy is higher than for the intermediate PES. If a local minimum is already well sampled at low temperatures then its effect on the free energy is already captured via the second term of Eq. S5.2 by the determination of $F_{\text{int}}(T_{\text{low}})$. If a local minimum becomes relevant at a specific temperature, then the free energy is lower than the free energy of a system without this local minimum. This lowering effect on the free energy can be achieved via an increase of $\langle U_{\text{anharmon}} \rangle_{\text{MLP}}$. We cannot directly link the magnitude of $\langle U_{\text{anharmon}} \rangle_{\text{MLP}, T}$ to the number of local minima that are getting sampled around this temperature, because the anharmonicity of the already sampled minima also has influence.

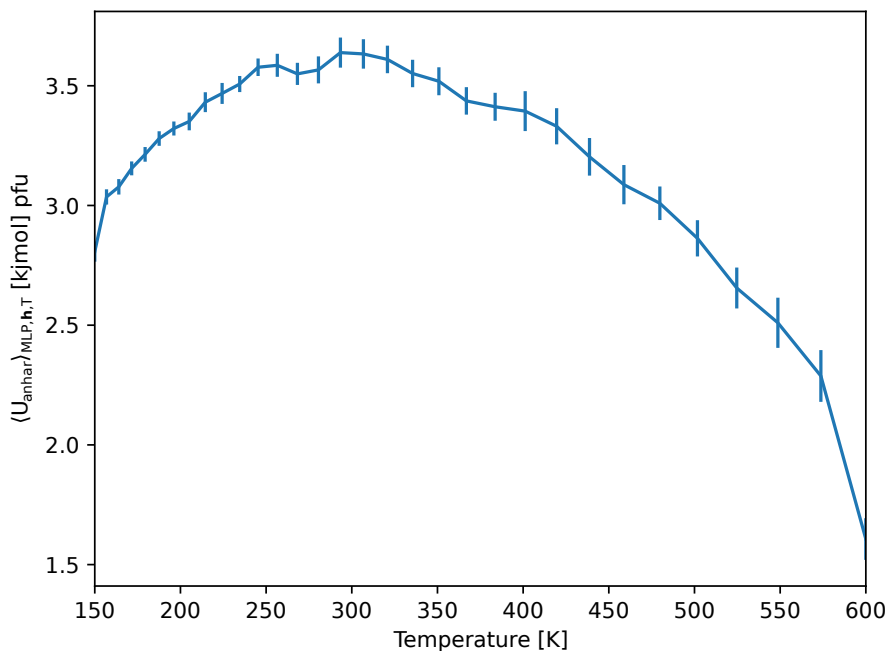


Figure S12: Ensemble average of the anharmonic energy of the MLP PES as a function of the temperature for the γ phase of FAPbI₃, with a simulation cell set to the average cell at 150 K.

5.6 Going from Helmholtz to Gibbs free energy

To go from the Helmholtz free energy at a specific simulation cell to the Gibbs free energy at a specific pressure we need to determine the probability of this simulation cell at this pressure, see also Eq. 2.6 in the manuscript. Because the probability of the six-dimensional simulation cell is difficult to determine, we use the probability of the volume instead. The probability of encountering the volume at a specific temperature and pressure is determined via NPT MD simulations at those conditions and by creating a histogram of the volumes with a bin size of 0.1 Å³ pfu. Fig. S13 shows the results for a NPT MD simulation at 150 K and 0.1 MPa for the γ phase of FAPbI₃. The probability is determined by the normalized magnitude of the bin that contains the volume of the used simulation cell. Because the histogram contains a bit of noise, we calculate the running average with a window of 9 and use the value at the volume of the simulation cell. This probability is close to the maximum probability because we used the average simulation cell of the NPT MD simulations to determine the Helmholtz free energy.

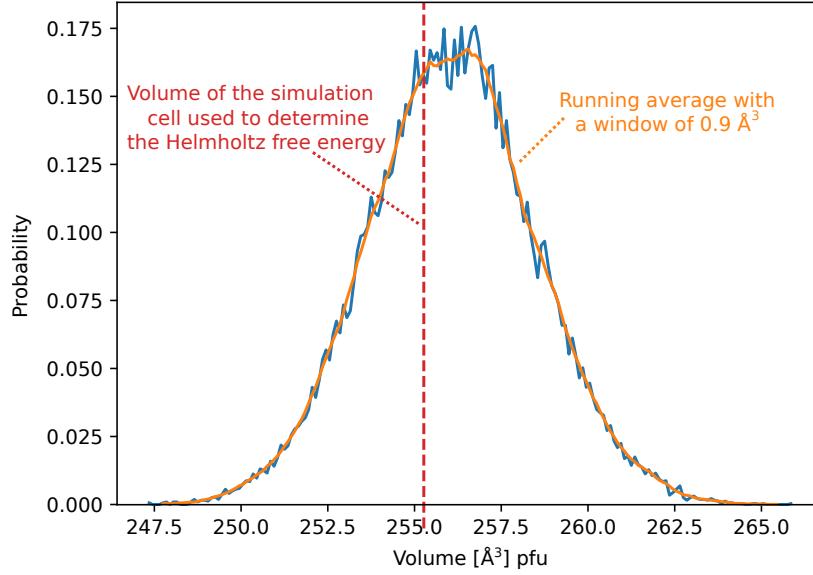


Figure S13: Probability distribution of the volume during a NPT MD simulation at 150 K and 0.1 MPa for the γ phase of FAPbI₃. The probability is estimated via a histogram with 0.1 Å³ as the bin size shown in blue. To decrease the noise on the histogram a running average with a window of 9 is shown in orange. The volume of the simulation cell used to determine the Helmholtz free energy is indicated by the vertical red dotted line.

5.7 Temperature correction to the Gibbs free energy for the MLP PES

The same analysis as in Sec. 5.5 is performed, except instead of the energy the anharmonic enthalpy is investigated. The anharmonic enthalpy is defined as follows:

$$\langle H_{\text{anharmon}} \rangle_{\text{int},T} = \langle H \rangle_{\text{int},T} - \langle H \rangle_{\text{harm},T}, \quad (\text{S5.3})$$

where $H = U + PV$, is the enthalpy of a structure, and $\langle H \rangle_{\text{harm},T} = H_{\text{GS}} + (3N - 3) \frac{k_{\text{B}}T}{2}$. Fig. S14 plots the ensemble average of the anharmonic enthalpy of the MLP PES for the γ phase of FAPbI₃ at atmospheric pressure. The ensemble average is higher for the enthalpy in NPT simulations than for the energy in the NVT simulations. An observation that is valid for all phases and all materials investigated in this work. This can be caused by the extra cell degrees of freedom not included in the definition of the harmonic enthalpy.

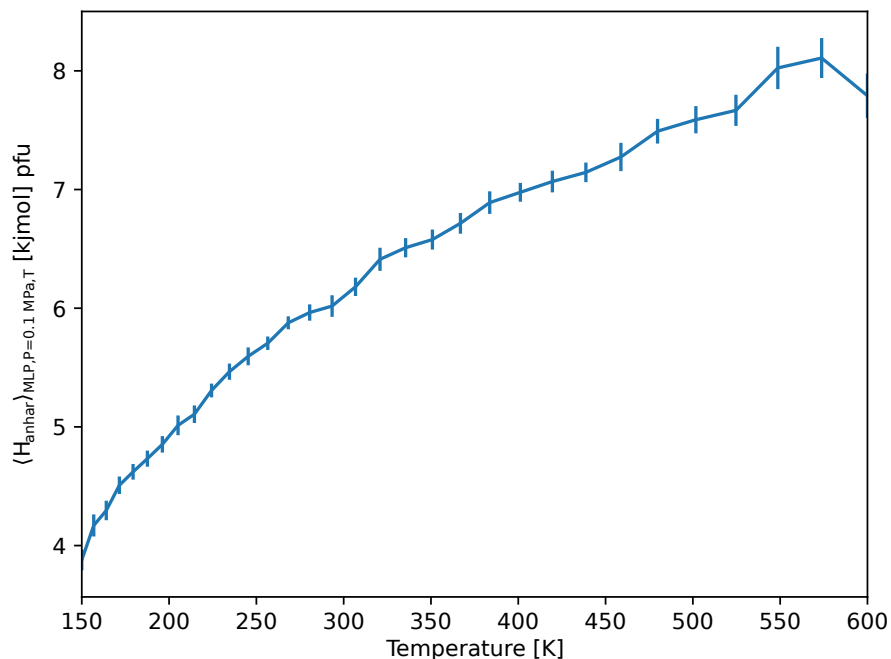


Figure S14: Ensemble average of the anharmonic enthalpy of the MLP PES as a function of the temperature for the γ phase of FAPbI₃ at atmospheric pressure.

5.8 Spectra from NVE MD simulations

As an alternative to the TI approach, the Helmholtz free energy can be determined using NVE MD simulations.³ Figure S15 presents the phonon spectrum for the γ phase of FAPbI₃, with the simulation cell set to the average structure at 150 K. Compared to the spectrum obtained via the Hessian matrix (see Fig. S8), we observe that the peaks are broadened.

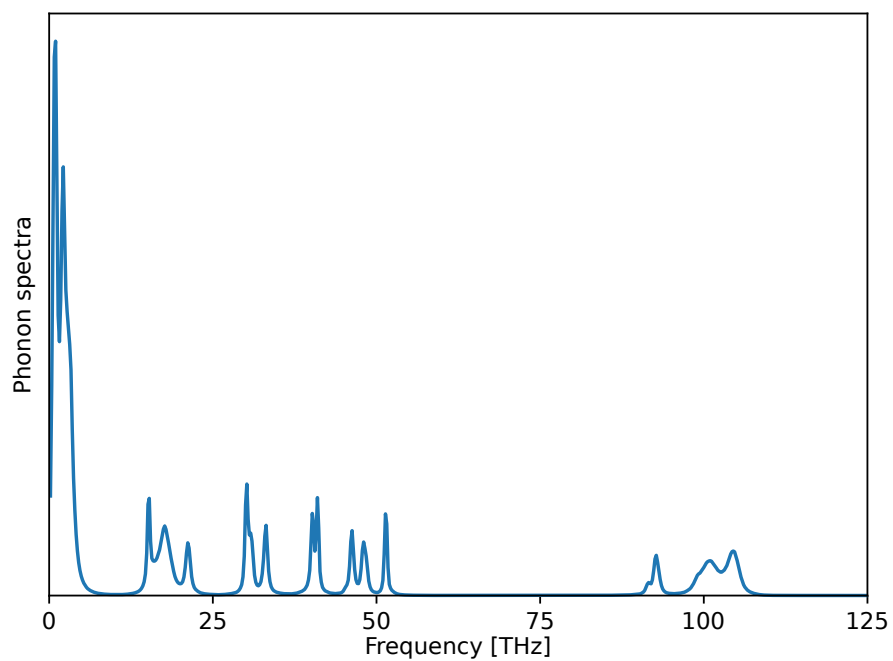


Figure S15: Phonon spectra for the γ phase of FAPbI₃, with a simulation cell set to the average cell at 150 K. This spectrum is calculated from NVE MD simulations at 150 K.

6 Parameters of the average cell used to calculate the Helmholtz free energy

Tabs. S4 (CsPbI₃), S5 (FAPbI₃), and S6 (MAPbI₃) present the parameters of the average simulation cell, containing 8 formula units, used to calculate the Helmholtz free energy. These parameters were obtained from NPT MD simulations at the specified temperature and a pressure of 0.1 MPa. Fig. S16 plots the volumes as a function of temperature. The volume is larger when the A-site cation is larger. For each material, the volumes of the phases are similar, only for the δ_{Cs} phase of CsPbI₃ is the volume significantly lower. As discussed in Sec. 4.3 of the manuscript, at low temperatures the orientational freedom of the MA molecules is more restricted than at higher temperatures. A possible explanation could be the volume of the simulation cell at 150 K, which is significantly lower than at the higher temperatures. This also explains why the FA molecules at lower temperatures are more free to rotate than the MA molecules, because the volume of the simulation cell of FAPbI₃ at 150 K is significantly larger, see Sec. 9.

Since the simulation cells containing 64 formula units are constructed as $2 \times 2 \times 2$ supercells of those with 8 formula units, their parameters are not presented here.

Table S4: Cell parameters for the NVT simulation of CsPbI₃ containing 8 formula units.

Phase	Average cell at temperature	$ \vec{a} $ [Å]	$ \vec{b} $ [Å]	$ \vec{c} $ [Å]	α [°]	β [°]	γ [°]	Volume pfu [Å ³]
γ	0	12.32	12.32	12.5	90.0	90.0	86.7	237.0
	150	12.56	12.4	12.4	87.84	89.98	90.01	241.0
	187	12.61	12.41	12.4	88.01	90.06	90.02	242.0
	234	12.45	12.62	12.43	89.95	91.28	89.99	244.0
	293	12.62	12.46	12.51	90.56	89.99	89.73	246.0
	350	12.65	12.52	12.53	90.26	90.14	90.05	248.0
	419	12.6	12.57	12.64	89.89	90.1	90.13	250.0
	501	12.61	12.65	12.68	90.11	89.98	90.02	253.0
	600	12.68	12.67	12.73	90.01	90.03	90.03	256.0
δ_{Cs}	0	17.8	10.39	9.59	90.0	90.0	90.0	221.0
	150	17.91	10.47	9.63	89.98	90.05	89.99	226.0
	187	17.94	10.5	9.64	90.02	90.02	89.99	227.0
	234	17.98	10.52	9.65	89.98	90.04	89.98	228.0
	293	18.03	10.56	9.67	90.0	90.04	89.97	230.0
	350	18.08	10.59	9.7	89.98	90.03	89.9	232.0
	419	18.15	10.63	9.72	89.98	90.04	89.96	234.0
	501	18.24	10.68	9.76	89.96	89.99	89.92	237.0
	600	18.36	10.73	9.81	89.96	90.05	89.96	241.0
δ_{FA}	0	16.01	13.91	8.43	90.0	90.0	90.0	235.0
	150	15.89	14.23	8.48	89.96	89.88	89.97	240.0
	187	15.85	14.34	8.49	89.98	90.01	89.96	241.0
	234	15.83	14.43	8.5	90.01	89.58	90.13	243.0
	293	15.81	14.57	8.51	90.06	89.65	90.86	245.0
	350	15.75	14.76	8.51	90.03	89.66	90.84	247.0
	419	15.78	14.86	8.53	89.94	89.03	91.51	250.0
	501	15.82	14.96	8.56	89.88	89.14	90.7	253.0
	600	15.91	15.07	8.6	89.68	89.75	90.51	258.0

Table S5: Cell parameters for the NVT simulation of FAPbI₃ containing 8 formula units.

Phase	Average cell at temperature	$ \vec{a} $ [Å]	$ \vec{b} $ [Å]	$ \vec{c} $ [Å]	α [°]	β [°]	γ [°]	Volume pfu [Å ³]
γ	0	12.59	12.76	12.59	90.0	92.8	90.0	253.0
	150	12.62	12.67	12.77	90.09	90.32	90.16	255.0
	187	12.73	12.72	12.77	89.43	89.7	89.62	258.0
	234	12.8	12.72	12.7	90.17	90.27	89.94	258.0
	293	12.78	12.81	12.79	90.24	90.41	89.96	262.0
	350	12.81	12.86	12.81	89.99	90.09	89.77	264.0
	419	12.85	12.89	12.85	89.83	89.66	89.73	266.0
	501	12.9	12.92	12.87	89.74	89.94	89.92	268.0
	600	12.95	12.98	12.94	89.96	89.95	89.8	272.0
δ_{Cs}	0	19.05	11.7	9.08	90.0	87.84	90.0	253.0
	150	19.49	11.55	9.21	91.14	89.2	90.0	259.0
	187	19.5	11.71	9.14	89.23	90.55	89.75	261.0
	234	19.55	11.74	9.16	88.92	89.63	91.61	263.0
	293	19.7	11.73	9.17	89.99	90.36	91.09	265.0
	350	19.77	11.67	9.24	90.68	89.81	89.55	267.0
	419	19.77	11.74	9.27	88.77	90.23	89.64	269.0
	501	19.88	11.74	9.35	89.51	90.12	89.94	273.0
	600	19.91	11.85	9.36	90.07	90.22	89.44	276.0
δ_{FA}	0	15.69	15.1	8.46	90.0	90.0	90.0	251.0
	150	15.75	15.34	8.59	89.48	90.41	92.5	259.0
	187	15.88	15.11	8.62	89.85	89.54	90.27	258.0
	234	15.82	15.17	8.73	90.1	91.72	88.67	262.0
	293	15.88	15.2	8.73	90.03	91.55	90.77	263.0
	350	15.95	15.31	8.71	89.96	90.96	90.83	266.0
	419	15.93	15.45	8.77	89.69	91.24	91.46	270.0
	501	16.01	15.46	8.83	89.82	90.76	90.13	273.0
	600	16.06	15.66	8.91	89.9	89.64	90.5	280.0

Table S6: Cell parameters for the NVT simulation of MAPbI₃ containing 8 formula units.

Phase	Average cell at temperature	$ \vec{a} $ [Å]	$ \vec{b} $ [Å]	$ \vec{c} $ [Å]	α [°]	β [°]	γ [°]	Volume pfu [Å ³]
γ	0	12.29	12.29	12.69	90.0	90.0	87.46	240.0
	150	12.27	12.43	12.74	90.05	90.04	90.1	243.0
	187	12.62	12.52	12.65	90.17	89.47	89.99	250.0
	234	12.69	12.59	12.59	89.89	90.72	90.24	251.0
	293	12.64	12.62	12.7	90.4	90.33	89.41	253.0
	350	12.67	12.69	12.67	90.47	90.21	90.05	255.0
	419	12.67	12.67	12.83	89.93	89.3	89.84	257.0
	501	12.74	12.73	12.82	90.27	90.12	89.78	260.0
	600	12.81	12.81	12.83	90.06	89.95	89.72	263.0
δ_{Cs}	0	18.54	11.02	9.52	90.0	90.0	90.0	243.0
	150	19.18	10.82	9.4	89.88	90.31	90.2	244.0
	187	19.2	10.89	9.38	90.04	90.42	90.0	245.0
	234	18.64	11.31	9.39	90.03	90.28	90.52	247.0
	293	19.33	10.87	9.44	90.26	90.13	89.35	248.0
	350	19.22	10.95	9.52	90.26	90.14	90.11	250.0
	419	19.12	11.06	9.57	90.52	89.87	91.05	253.0
	501	19.17	11.12	9.63	90.18	89.89	89.11	257.0
	600	19.22	11.17	9.73	90.1	89.71	90.54	261.0
δ_{FA}	0	15.75	14.67	8.49	86.07	90.0	90.0	245.0
	150	15.72	14.91	8.49	88.52	94.44	89.65	248.0
	187	15.73	14.89	8.51	89.18	93.25	89.62	249.0
	234	15.75	14.9	8.54	89.53	88.41	90.12	250.0
	293	15.72	14.97	8.6	90.05	88.42	89.4	253.0
	350	15.73	14.98	8.66	89.7	90.21	88.47	255.0
	419	15.81	15.04	8.67	89.83	90.49	89.5	258.0
	501	15.85	15.16	8.68	89.82	89.62	89.47	261.0
	600	15.93	15.23	8.75	89.86	90.33	89.98	265.0

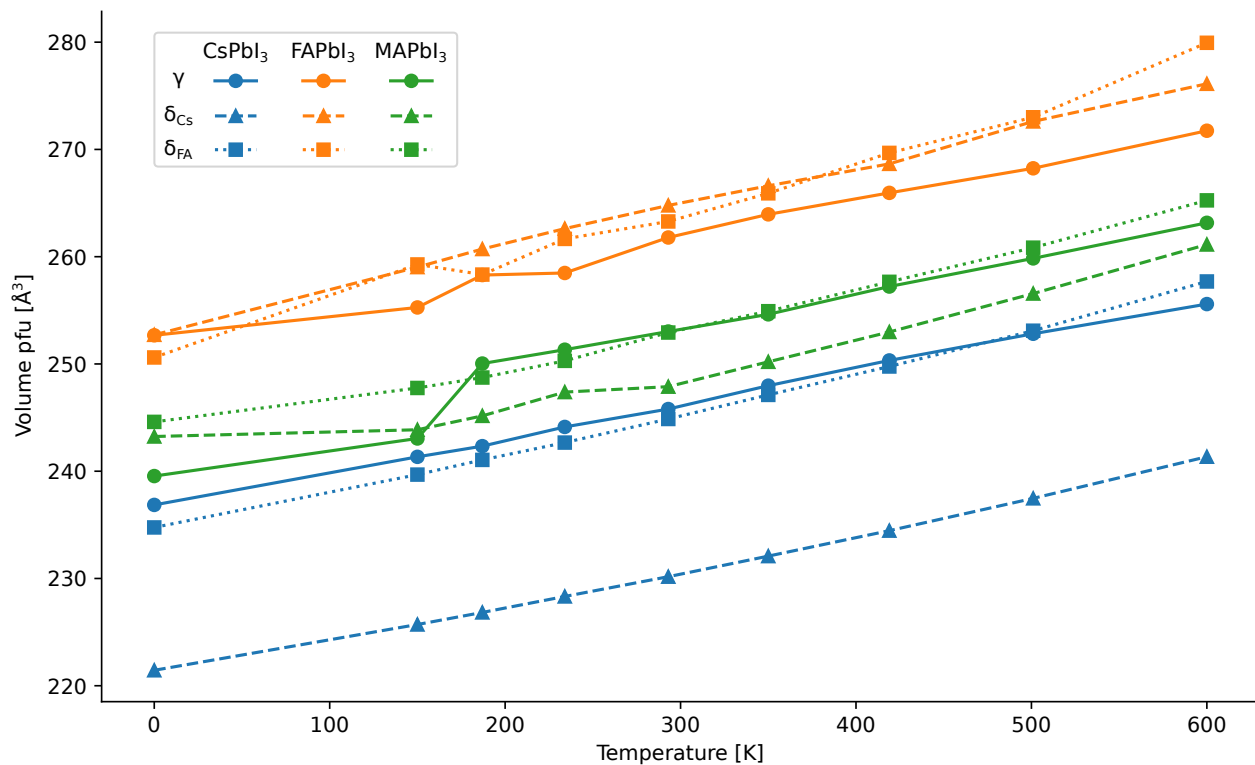


Figure S16: Volume of the average simulation cell in NPT at 0.1 MPa as a function of temperature for the three phases of CsPbI₃, FAPbI₃, and MAPbI₃.

7 Histogram of optimized energies

Figs. S17 (CsPbI_3), S18 (FAPbI_3), and S19 (MAPbI_3) present the histograms of the optimized energies keeping the simulation cell fixed at different temperatures. For each histogram, the optimizations were performed on 4000 initial structures that were generated via NVT (NPT) MD simulations at 150 K (and 0.1 MPa). To escape local minima, these MD simulations were coupled via REX with 31 simulations at higher temperatures, reaching a maximum of 600 K. For all phases and simulation cells of CsPbI_3 , the 4000 optimizations resulted in approximately the same energy, while for FAPbI_3 and MAPbI_3 the energy distribution is broader. This is the result of the organic molecules which create multiple minima due to their orientation. For most simulations and phases of MAPbI_3 the lowest energy has (almost) the highest probability to be found, while for FAPbI_3 the lowest energy has a rather low probability. Only the lowest energy for the δ_{Cs} phase of FAPbI_3 has a good probability to be found.

In Sec. 9 the possible orientations of the organic molecules are plotted for the three phases of FAPbI_3 and MAPbI_3 . At 150 K the possible orientations of the organic molecules are more restricted for MAPbI_3 than for FAPbI_3 , and of the three phases of FAPbI_3 the FA molecules have the least freedom in the δ_{Cs} phase. A smaller phase space for the organic molecules correlates with a higher probability of finding the lowest energy. Therefore, it was crucial to choose initial structures from MD simulation at 150 K that were coupled with higher-temperature MD simulation via REX to escape local minima.

There are two options to improve the probability of finding the lowest energy. Namely, performing REX MD simulations with a lower minimal temperature to eliminate higher energy local minima, and performing more optimization. However, given the maximum temperature of our REX simulations is 600 K, 150 K as a minimum temperature is at the limit to assure a proper acceptance rate for 32 replicas. Moreover, given that we perform optimizations for 3 materials, 3 phases, 8 simulation cells containing 8 formula units, and 3 simulation cells containing 3 formula units, 4000 optimizations are at the limit of our computational resources. In principle, the TI approach is valid for any harmonic PES around random local minima. Therefore, it is not necessary to use the global minima. However, the TI corrections might be more difficult to converge.

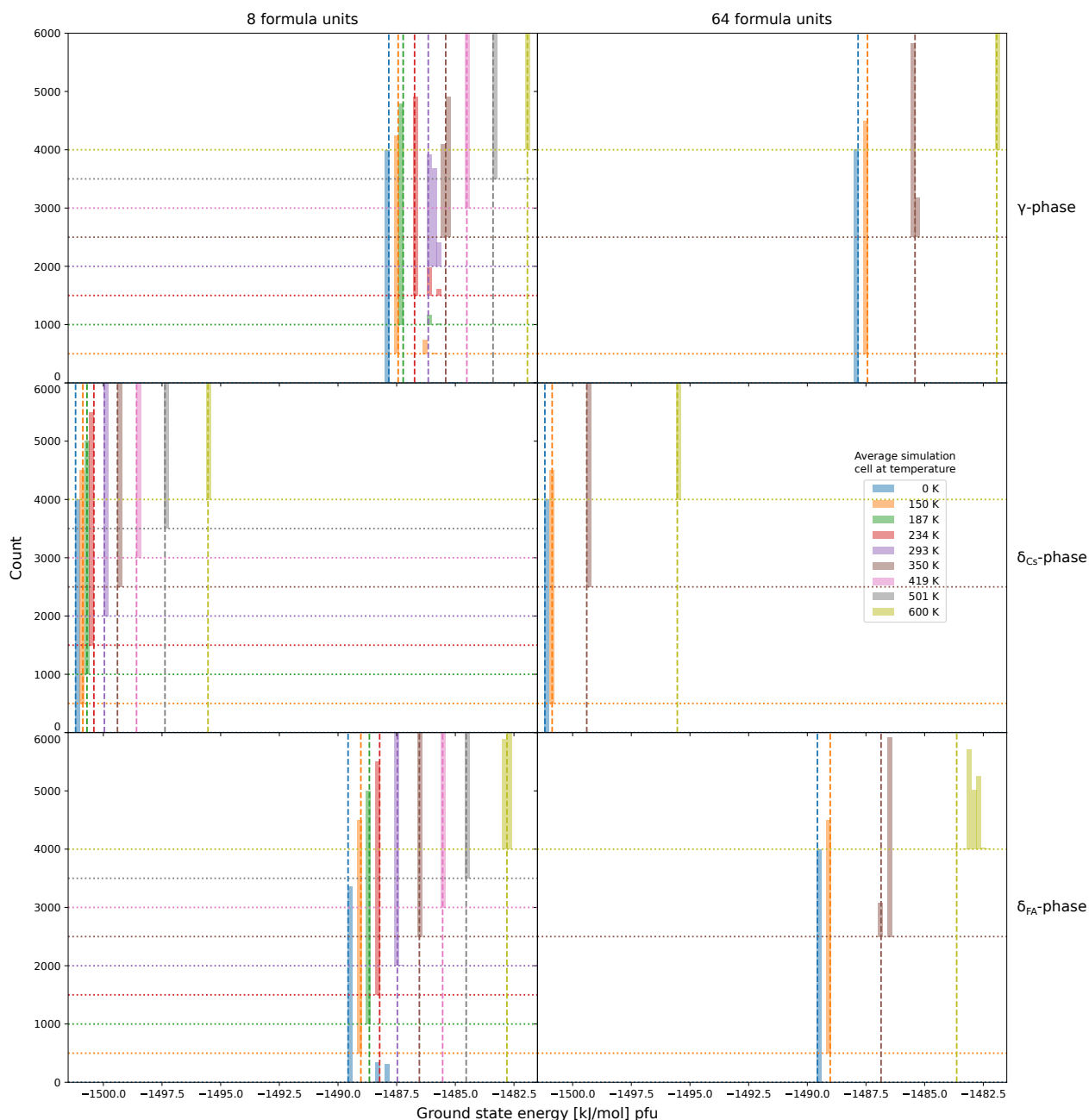


Figure S17: Histograms with a bin size of 0.2 kJ/mol pfu for the energy of 4000 optimized structures of CsPbI₃. The results for the three phases containing 8 and 64 formula units are shown. The blue histograms (*i.e.* 0 K) show the results for a full cell optimization, while the other optimizations kept the simulation cell fixed to the average cell at the specified temperature and at 0.1 MPa.

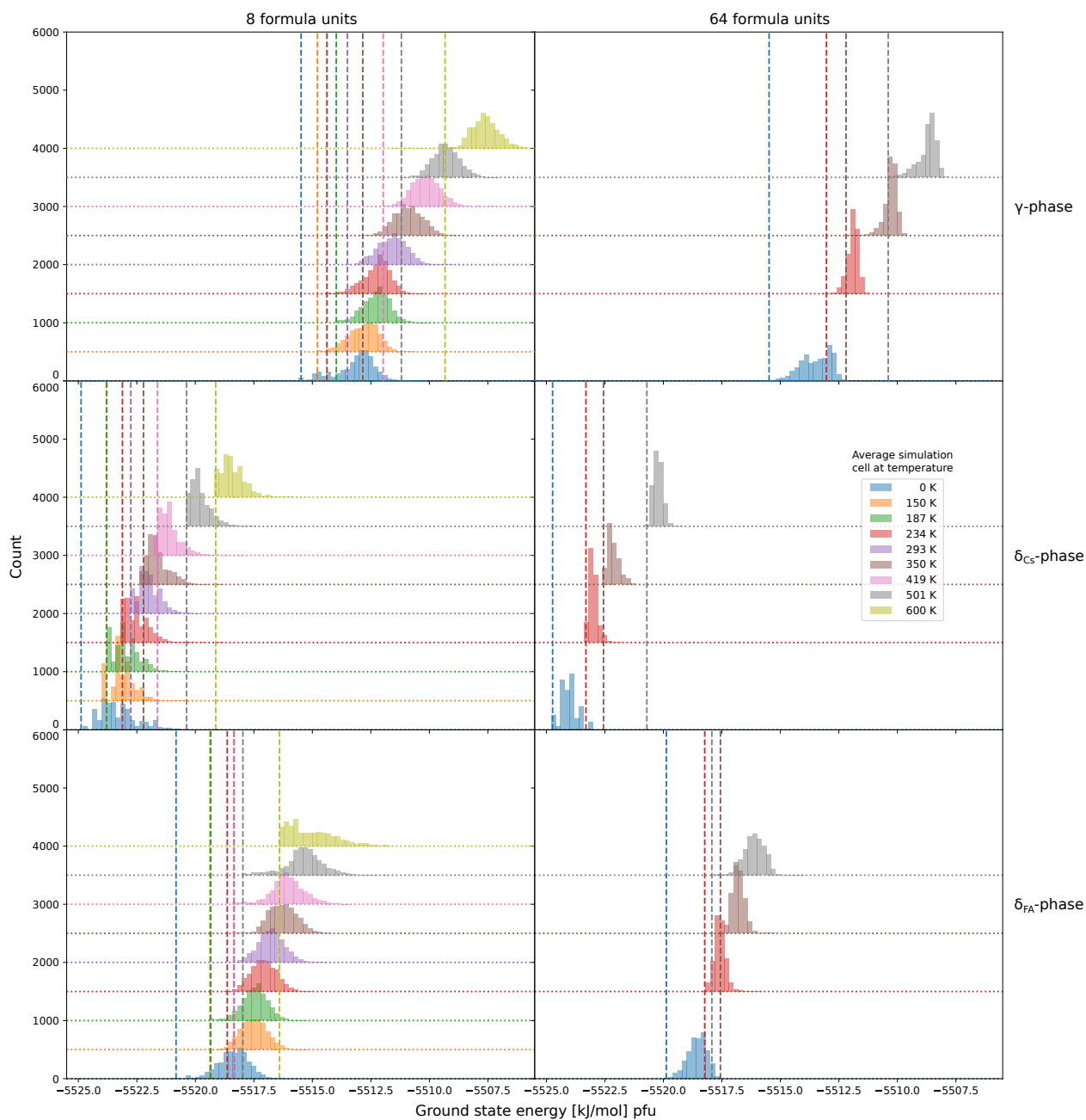


Figure S18: Histograms with a bin size of 0.2 kJ/mol pfu for the energy of 4000 optimized structures of FAPbI_3 . The results for the three phases containing 8 and 64 formula units are shown. The blue histograms (*i.e.* 0 K) show the results for a full cell optimization, while the other optimizations kept the simulation cell fixed to the average cell at the specified temperature and at 0.1 MPa.

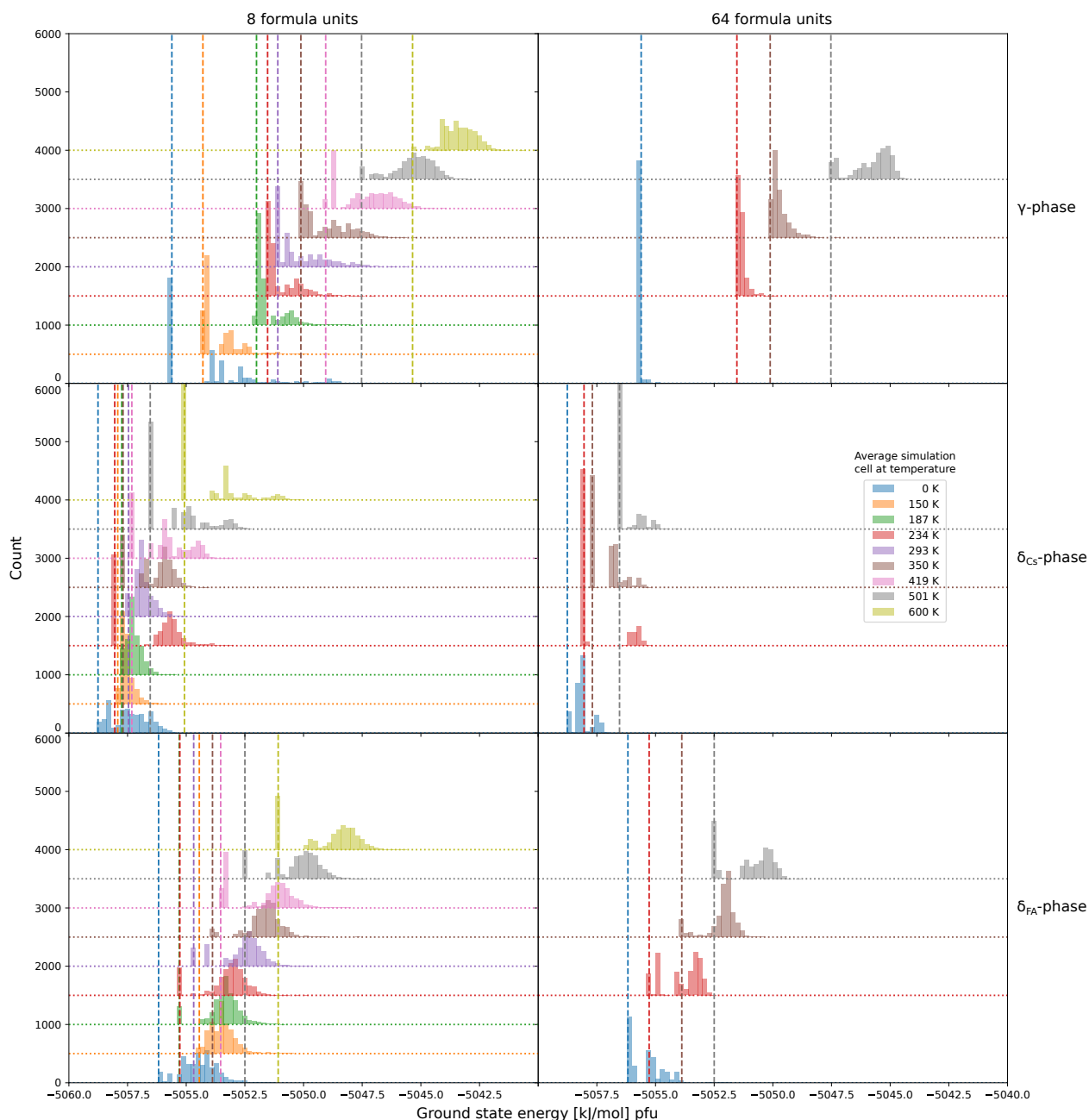


Figure S19: Histograms with a bin size of 0.2 kJ/mol pfu for the energy of 4000 optimized structures of MAPbI₃. The results for the three phases containing 8 and 64 formula units are shown. The blue histograms (*i.e.* 0 K) show the results for a full cell optimization, while the other optimizations kept the simulation cell fixed to the average cell at the specified temperature and at 0.1 MPa.

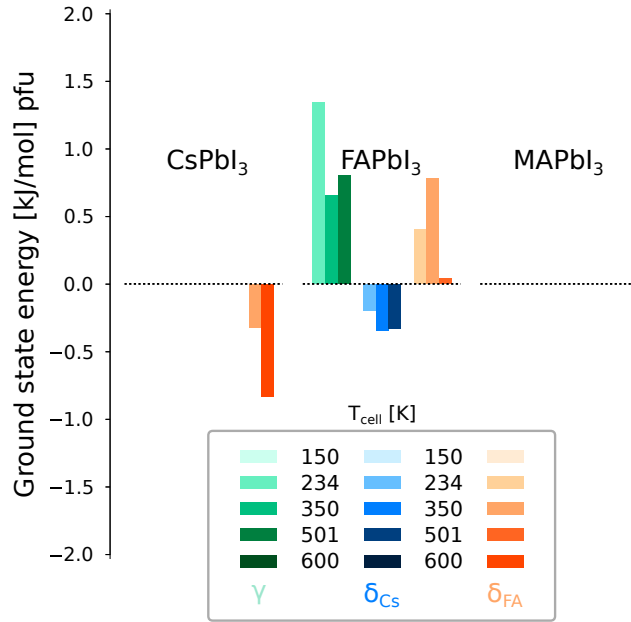


Figure S20: Ground state energy difference between optimized structures for 64 and 8 formula units.

Fig. S20 shows the differences between the lowest energy found for 64 and 8 formula units. Because the phase space is significantly larger for the 64 formula units, the probability of not finding the lowest energy is higher. Given the low probability of finding the lowest energy for the γ and δ_{FA} phases of FAPbI₃ containing 8 formula units, the optimization on 64 formula units failed to find this energy. Therefore, we opted to use the $2 \times 2 \times 2$ supercells of the lowest energy structure for 8 formula units to construct a harmonic PES for 64 formula units. Only the supercells for the δ_{FA} phase of CsPbI₃ and the δ_{Cs} phase of FAPbI₃ could optimize to a lower energy. For those systems, we did not use the lowest energy structure. However, this does not necessarily introduce errors because the TI approach can correct this.

8 Supercell effect on the free energy contributions

Fig. S21 shows the free energy difference between the δ phases and the γ phase as a function of temperature in different PESs for simulation cells containing 64 formula units. The uncertainty due to the simulation cell is almost negligible for the Helmholtz and Gibbs free energies, only CsPbI₃ has a small dependence. We only performed the supercell simulation for three different simulation cells due to the high computational cost, which could hide larger discrepancies for different simulation cells. However, it appears that the cell degrees of freedom are not that relevant for a simulation cell containing 64 formula units. This is not surprising because there are only six cell degrees of freedom compared to 960 (CsPbI₃) or 2304 (FAPbI₃ and MAPbI₃) atomic degrees of freedom.

Compared to the results for eight formula units (see Fig. 6 in the manuscript), the Helmholtz and Gibbs free energy is higher for the γ phase compared to the δ phases, which increases the transition temperatures. Fig. S22 shows the effect of the supercell on the six contributions to the Helmholtz free energy for each phase, and Fig. S23 shows the effect of the supercell on the energy difference with respect to the γ phase. The ground state energy is not influenced because we used the $2 \times 2 \times 2$ supercells of the lowest energy structure for 8 formula units, see Sec. 7. The supercell leads to lower harmonic free energies for each phase, which can be explained by comparing the frequency spectra, see Fig. S24. The supercell has modes with lower frequencies that have a lower harmonic free energy, see Eq. 2.5 in the manuscript. This stabilizing effect is larger for the δ phases compared to the γ phase. However, the anharmonic contribution partly counteracts this stability difference between the γ and δ phases. Because the supercell positively affects the anharmonic corrections of the γ phase and not the δ phases. The supercell has on average a destabilizing effect on the configurational free energy, because the number of minima do not scale exponentially with system size. This destabilizing effect is the largest for the γ phase because the tilt of one octahedra influences the tilts of the other octahedra. Irregular tilting patterns lead to higher energies and thereby higher free energies.

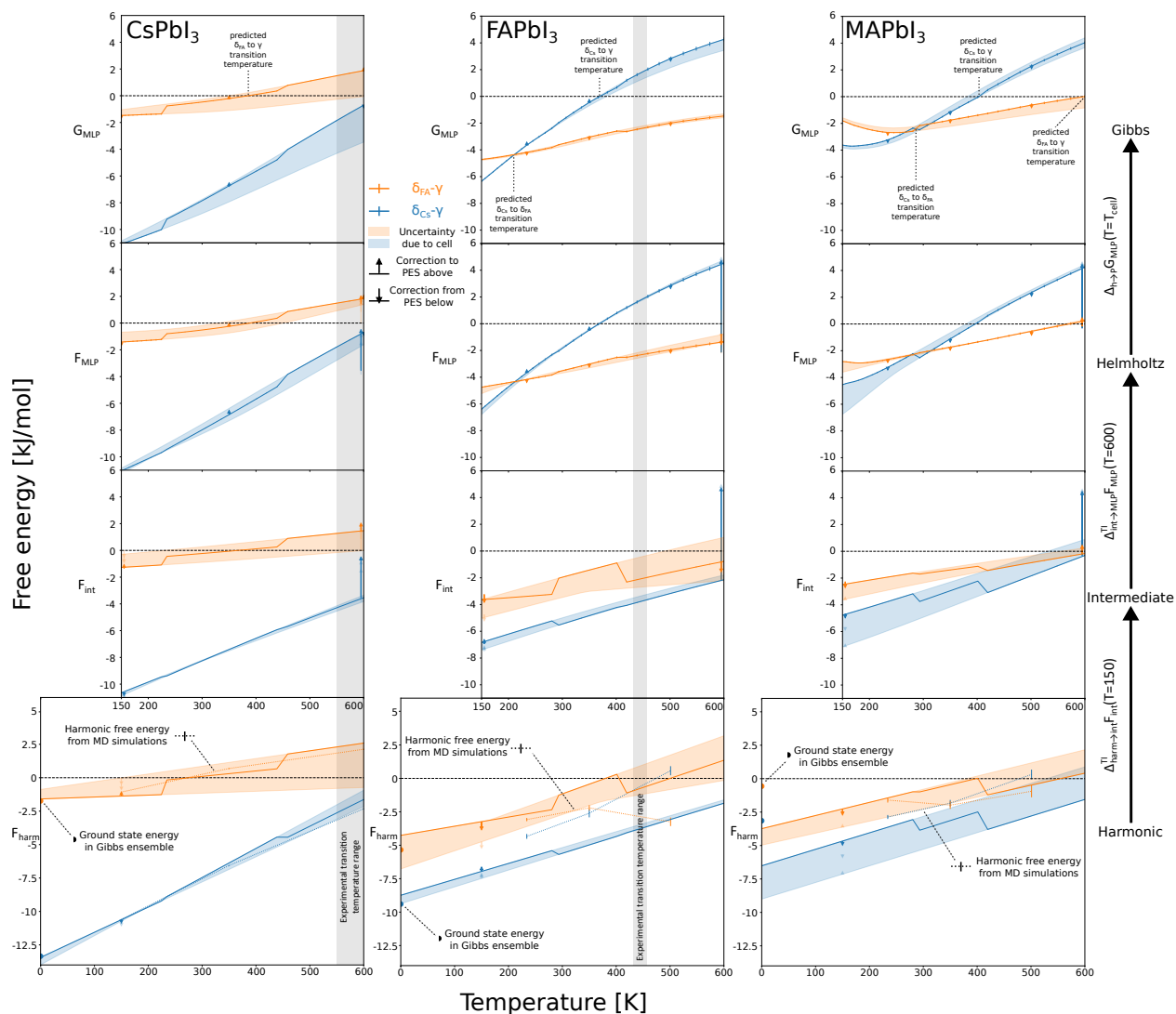


Figure S21: Free energy difference of the δ_{CS} (blue) and δ_{FA} (orange) phases relative to the γ phase as a function of temperature, computed using different PES: harmonic (via NVE MD simulations, dashed lines, and via Hessian calculations, solid lines with shaded areas), intermediate, and MLP. The Helmholtz and Gibbs free energies for the MLP PES are obtained from MD simulations in the NVT and NPT ensembles, respectively. The results correspond to simulation cells containing 64 formula units of $CsPbI_3$, $FAPbI_3$, and $MAPbI_3$. For the NVT simulations, eight independent simulation cells were used, with the shaded area representing the range between minimum and maximum values. The solid lines depict the free energy computed for the average NPT MD simulation cell at the temperature that is closest to the given x-axis value on a logarithmic scale. The arrows originating from the solid lines represent corrections to the free energy plotted above, while the arrows pointing toward the solid lines represent corrections arising from the free energy plotted below.

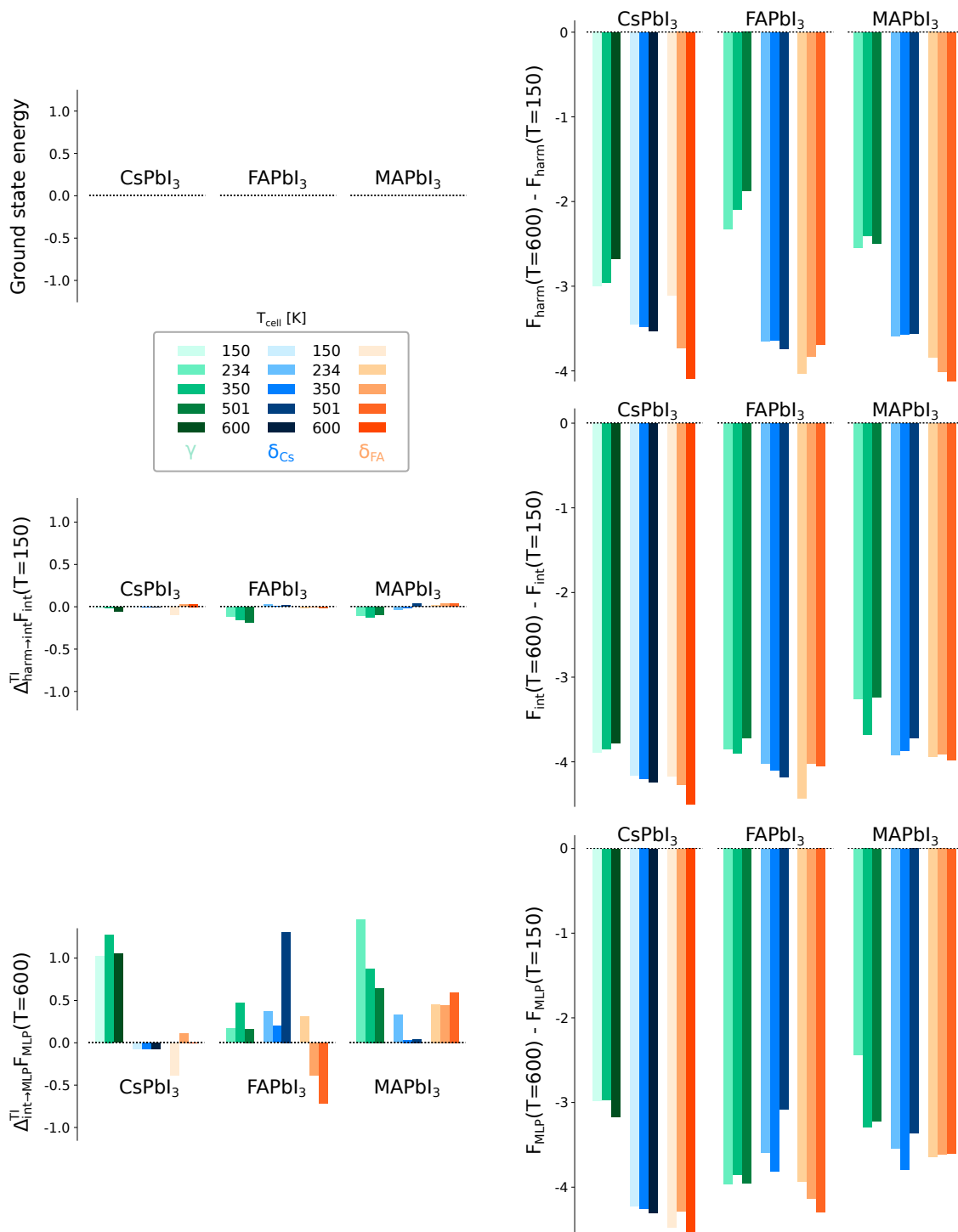


Figure S22: Free energy contributions to the total Helmholtz free energies calculated with the average simulation cells at three different temperatures, see Eq. 2.8 in the manuscript. The energy differences between the contributions for 64 and 8 formula units are reported, positive values indicate that the phase is more stable for 8 formula units. The results of the three phases of CsPbI₃, FAPbI₃, and MAPbI₃ are shown. The left side shows the ground state energy and the λ -TI corrections to the intermediate and MLP PES. The right side indicates the temperature effect on the free energy for the harmonic, intermediate, and MLP PES.

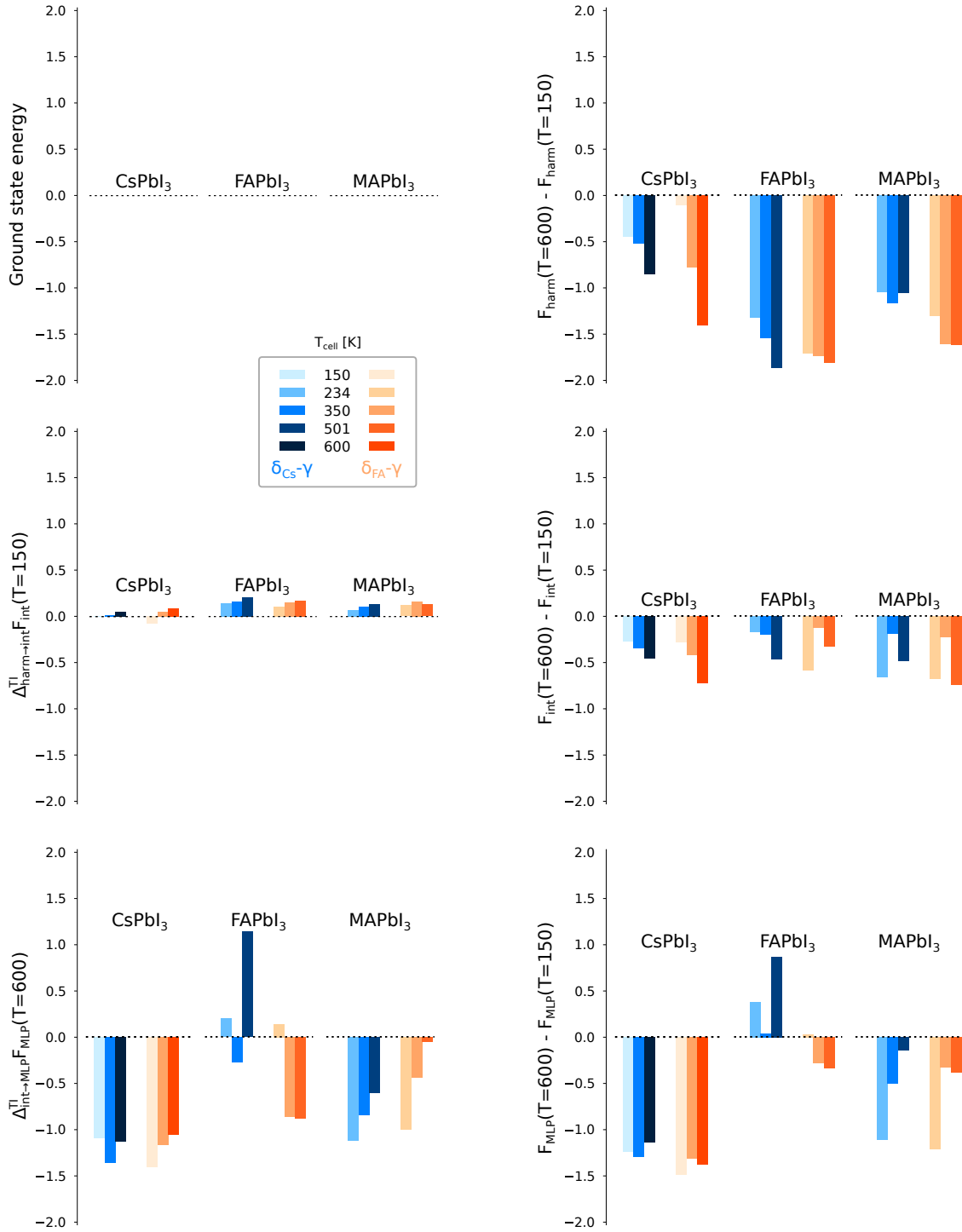


Figure S23: Free energy contributions to the total Helmholtz free energies calculated with the average simulation cells at three different temperatures, see Eq. 2.8 in the manuscript. The effect of the supercell on the energy differences of the δ phases with respect to the γ phase is reported. Positive values indicate that the γ phase is more stable for simulation cells with 64 formula units instead of 8. The left side shows the ground state energy and the λ -TI corrections to the intermediate and MLP PES. The right side indicates the temperature effect on the free energy for the harmonic, intermediate, and MLP PES.

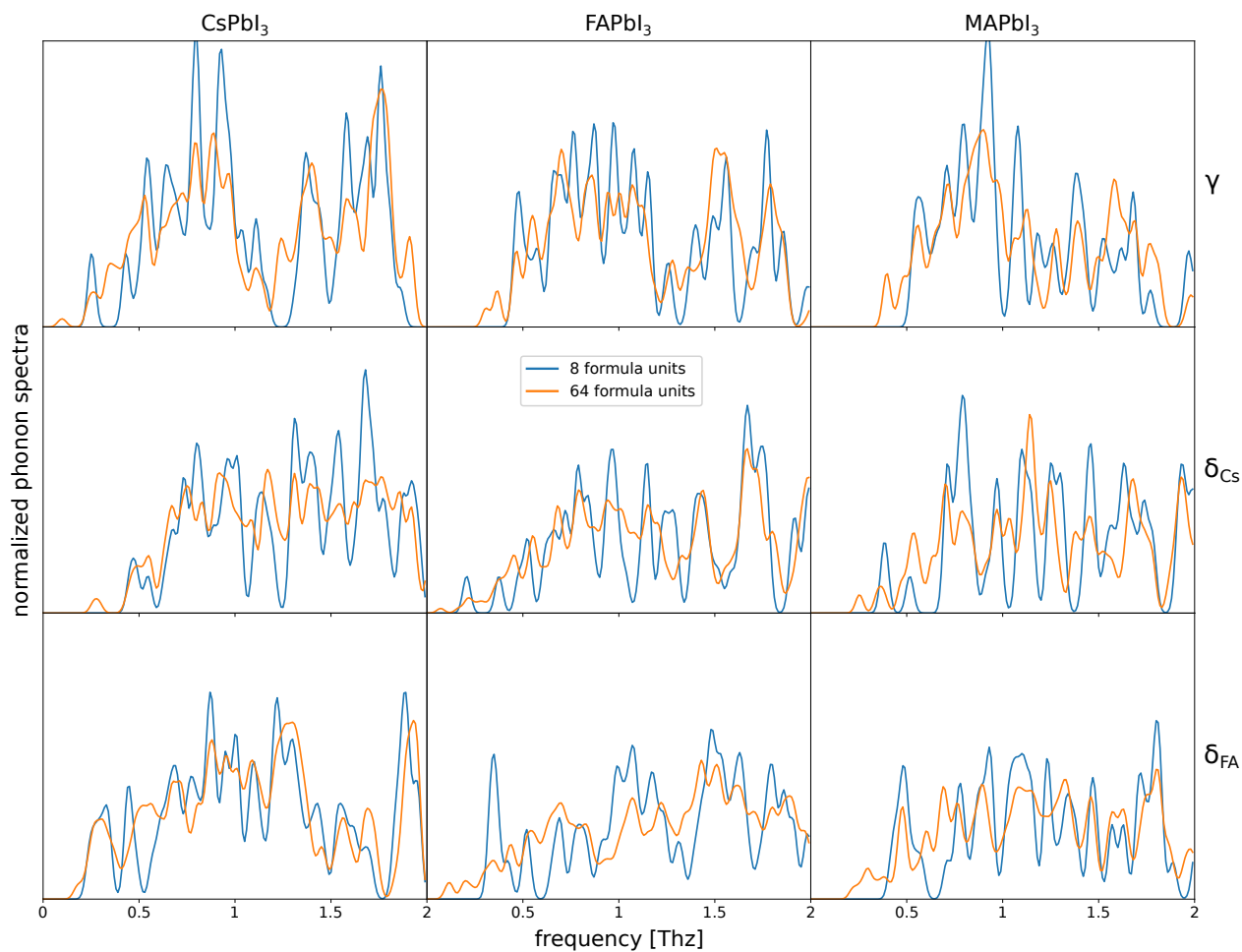


Figure S24: The normalized phonon spectra for the three phases of CsPbI_3 , FAPbI_3 , and MAPbI_3 for simulations containing 8 and 64 formula units. Calculated via the Hessian matrix of the lowest energy structure that was optimized keeping the simulation cell fixed to the average cell at 350 K and 0.1 MPa. Gaussian smearing of 0.02 THz is added to the eigenvalues of the mass-weighted Hessian.

9 Orientation of the organic molecules

Figs. S25 and S26 show the possible orientations of the organic molecules in FAPbI₃ and MAPbI₃, respectively. The coloring of the dots is based on the orientation of the reference organic molecule, where the RGB values are set by the x , y , and z values of the CN unit vector. For FAPbI₃ we can see that the colors mix for the three phases even at the lowest temperature. Similarly for the MAPbI₃ phases, the colors mix except for the γ phase at 150 K. This means that the orientation of one MA molecule influences the orientation of the other MA molecules reducing the number of local minima that can be sampled at 150 K. At higher temperatures (and for bigger simulation cells, see also Fig. 8 in the manuscript), the organic molecules have more freedom to orient irrespective of neighboring molecules. This may explain why the configurational free energy contribution becomes increasingly stabilizing for the γ phase of MAPbI₃ at higher temperatures.

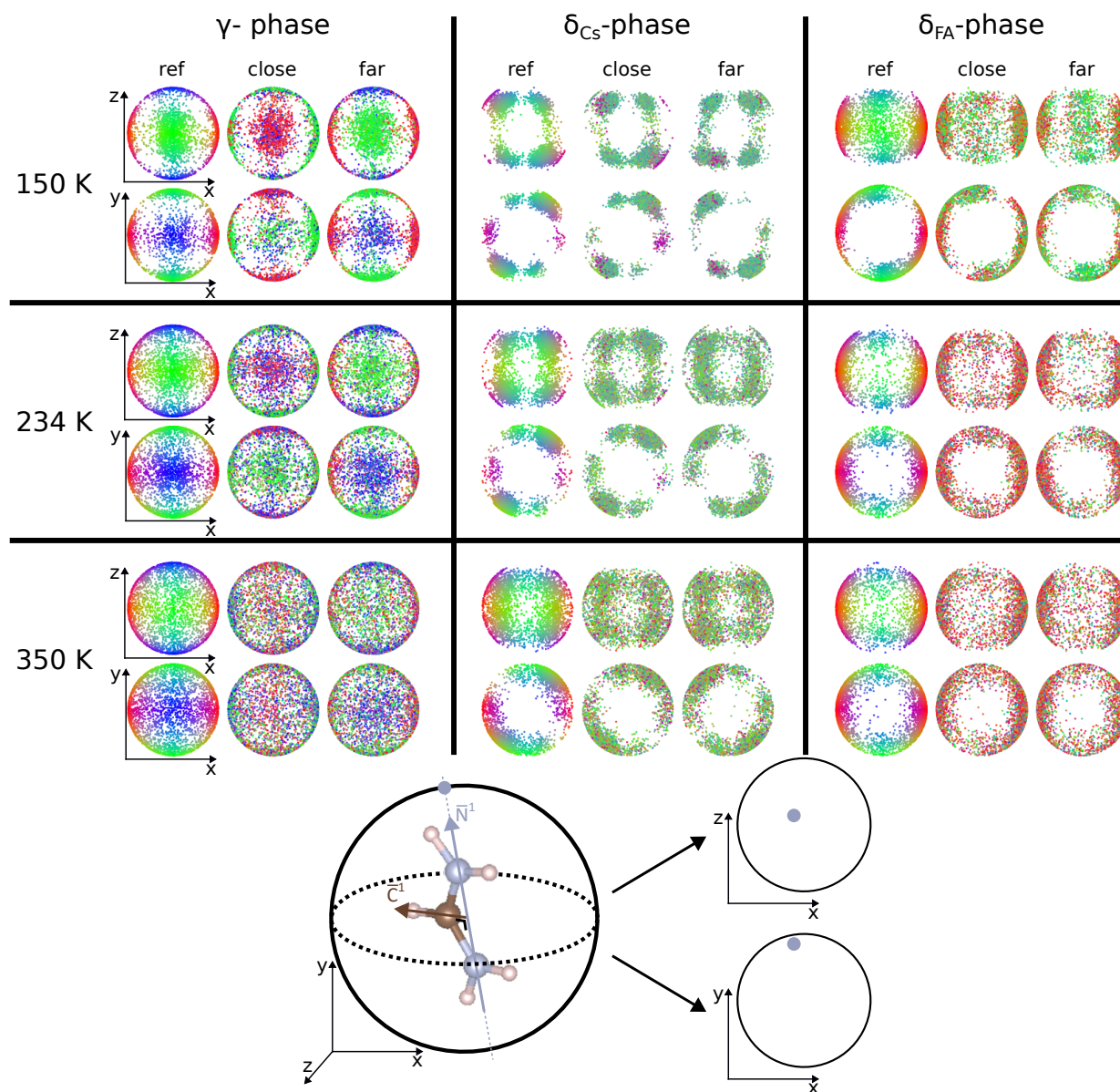


Figure S25: Orientation distributions of three FA molecules in FAPbI₃ during NVT simulations on the MLP PES at the specified temperature using the average simulation cell at that temperature. The orientation of each molecule is represented by the unit vector \vec{N} , defined from the two nitrogen atoms. The endpoints of these vectors are projected onto the xz and xy planes, as illustrated at the bottom of the figure. For each simulation, three FA molecules are selected: one is randomly chosen as the reference, and the other two are the nearest and furthest molecules from the reference. The RGB color of each dot is determined by the x , y , and z components of the \vec{N} vector of the reference MA molecule in the simulation cell.

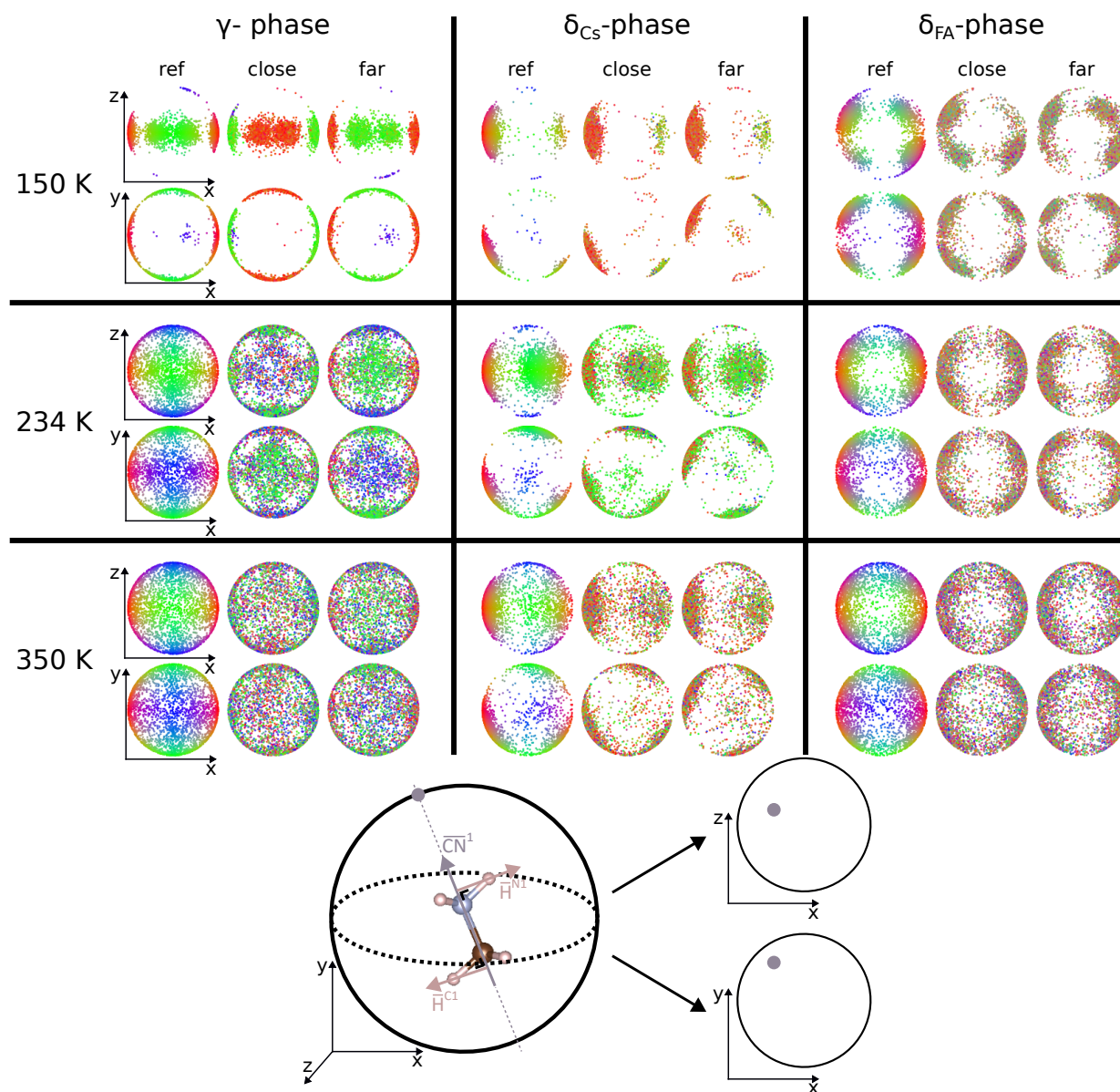


Figure S26: Orientation distributions of three MA molecules in MAPbI₃ during NVT simulations on the MLP PES at the specified temperature using the average simulation cell at that temperature. The orientation of each molecule is represented by the unit vector \vec{CN} , defined from the two nitrogen atoms. The endpoints of these vectors are projected onto the xz and xy planes, as illustrated at the bottom of the figure. For each simulation, three MA molecules are selected: one is randomly chosen as the reference, and the other two are the nearest and furthest molecules from the reference. The RGB color of each dot is determined by the x , y , and z components of the \vec{CN} vector of the reference MA molecule in the simulation cell.

References

- (1) Peters, L. D. M.; Dietschreit, J. C. B.; Kussmann, J.; Ochsenfeld, C. Calculating free energies from the vibrational density of states function: Validation and critical assessment. *J. Chem. Phys.* **2019**, *150*, 194111.
- (2) Kapil, V.; Engel, E.; Rossi, M.; Ceriotti, M. Assessment of Approximate Methods for Anharmonic Free Energies. *Journal of Chemical Theory and Computation* **2019**, *15*, 5845–5857.
- (3) Braeckvelt, T.; Goeminne, R.; Vandenhaute, S.; Borgmans, S.; Verstraelen, T.; Steele, J. A.; Roeffaers, M. B. J.; Hofkens, J.; Rogge, S. M. J.; Van Speybroeck, V. Accurately Determining the Phase Transition Temperature of CsPbI₃ via Random-Phase Approximation Calculations and Phase-Transferable Machine Learning Potentials. *Chemistry of Materials* **2022**, *34*, 8561–8576.
- (4) Beveridge, D. L.; DiCapua, F. M. Free Energy Via Molecular Simulation: Applications to Chemical and Biomolecular Systems. *Annual Review of Biophysics* **1989**, *18*, 431–492.
- (5) Cheng, B.; Ceriotti, M. Computing the absolute Gibbs free energy in atomistic simulations: Applications to defects in solids. *Phys. Rev. B* **2018**, *97*, 054102.